

Three-dimensional modeling of minor chemical constituents in the mesosphere/lower thermosphere region

Dissertation

am Leibniz-Institute für Atmosphärenphysik in Kühlungsborn zur Erlangung
der Doktorwürde der Mathematisch-Naturwissenschaftlichen Fakultät der
Universität Rostock

Mykhaylo Grygalashvyly

Juli 2008

Contents

1	Introduction	4
1.1	Motivation.....	4
1.2	Thesis Outline.....	5
2	Model Description	7
2.1	Dynamic Model.....	8
2.2	Chemistry-Transport Model (CTM).....	9
2.2.1	Chemical Code.....	10
2.2.2	Radiation Code.....	10
2.2.3	Diffusion Code.....	11
2.2.3.1	Eddy Diffusion.....	11
2.2.3.2	Molecular Diffusion.....	12
2.2.4	Advection.....	14
2.3	Improvements.....	15
2.3.1	Walcek Scheme.....	15
2.3.2	Water Vapor Photolyses Rate.....	17
3	Modeling of Global Water Vapor	19
3.1	Results and Comparison with Observations.....	19
3.2	Dependence on Solar Activity.....	22
3.3	Autocatalytic Water Vapor Production.....	27
3.4	Summary and Conclusions.....	35
4	Trend Calculations	37
4.1	General Problem.....	37
4.2	Chemical aspects.....	39
4.3	Water Vapor.....	41
4.4	Ozone.....	44
4.5	Hydroxyl.....	47
4.6	Carbon Monoxide.....	48
4.7	NO _x	48
4.8	Chemical Heat.....	49
4.9	Summary and Conclusions.....	51
5	Ozone	53
5.1	Middle Mesospheric Maximum (MMM) of Ozone Near the Polar Night Terminator.....	53
5.2	Results.....	54
5.3	Discussion.....	56
5.4	Conclusions.....	58
6	Non-Linear Effects in the MLT Region	60
6.1	General Discussion.....	60
6.2	Mesopause Region.....	62

6.3	Middle Mesospheric Ozone Oscillations at the Polar Day Terminator.....	66
6.4	Summary and Conclusion.....	68
7	Influence of Sudden Stratospheric Warmings (SSWs) on the chemistry in the extended Mesopause Region	69
7.1	The Sudden Stratospheric Warming (SSW).....	69
7.2	Effects During SSW in the Extended Mesopause Region.....	70
7.3	Summary and Conclusions.....	79
8	Other Results	81
8.1	Chemical Heating Rates	
8.1.1	The Problem.....	81
8.1.2	Results.....	82
8.2	Computation of OH* and OH	
8.2.1	Introduction.....	83
8.2.2	Calculation of the Concentrations of OH* in the Different Exited States.....	85
8.2.3	Results.....	86
8.3	Summary and Conclusions	88
9	Summary and Outlook	89
9.1	The Most Important Results.....	89
9.2	Open Questions and Future Improvements of the CTM.....	90
A	History	92
B	Derivation of the Equation for Calculation of Eddy Diffusion	94
C	Derivation of the Equation for Calculation of Molecular Diffusion	96
D	Description of Walcek Scheme.	99
E	The Cycles for Water Vapor	102
F	The Chemical Reactions	103
	References	105

Chapter 1

Introduction

1.1 Motivation

The minor chemical constituents play a significant role in the middle atmosphere. These constituents determine the radiation budget and influence the dynamics through heat, which calorificates in chemical reactions. Very few constituents can be measured by various ground based or rocket- and satellite-borne techniques available. For certain time periods or geographical regions other constituents are unmeasurable. The mesosphere - sometimes also called the "ignorosphere" - is still a region characterized by different unexplained phenomena. There is a permanent lack of data required for different investigations to employ model data. Different discrepancies between observations and model calculations have been reported in the recent past. Examples of these discrepancies are: the so-called ozone deficit problem [e.g. Clancy et al., 1987; Eluszkiewicz, 1993; Siskind et al., 1995; Summers et al., 1997], the HO_x dilemma [Summers et al., 1997; Offermann, 2000; Conway et al., 2000], and the upper mesospheric water vapor layer explained in terms of the recombination of O and H₂ on meteoric dust [Summers and Siskind, 1999]. The intercomparison of observations revealed considerable differences between individual measurements [Nedoluha and Hartogh, 2006]. However, the comparison between different model results also showed distinct differences [Sonnemann et al., 2005]. Moreover, not all phenomena in the atmosphere can be studied by measurements. Two reasons for this are a lack of ability and precision (for example, the water vapor measurements above 85 km). It is not easy to measure all chemical constituents together in the same place and time, however this is sometimes necessary in order to understand a phenomenon. Consequently, this situation also requires the development of sophisticated models. Both the monitoring of the atmosphere and its modeling are necessary to investigate its physical and chemical state.

On the other hand, three dimensional dynamical models need global distributions of chemical constituents for calculations of radiation and heat budgets. The solution to the problem is made possible by the development of models which calculate the distribution of chemical constituents and which also feed the dynamic part of the model. Moreover, three-dimensional models of dynamics and chemistry can be applied to study the influence of anthropogenic activity on Earth's atmosphere, response of the atmosphere to different impacts and predictions of future states. Furthermore, three-dimensional models of the dynamics and chemistry, verified with data from measurements and examined for the Earth's atmosphere, can be generalized for the atmospheres of other planets. The modeling is very important for the Earth and other planets where the ability to gain measurements is limited.

1.2 Thesis Outline

The focus of this thesis is to study some of the features of the behavior and distribution of important minor chemical constituents such as ozone, water vapor, hydroxyl etc. in the middle atmosphere using a sophisticated chemistry-transport model (CTM). A short historical overview can be found in appendix A.

A time-dependent three-dimensional numerical chemistry-transport model was developed and used to study the distribution of chemical minor constituents in the mesosphere - lower thermosphere (MLT) region. All physical processes believed to be important are simulated in the model, including chemical interaction, photochemical dissociation, eddy and molecular diffusion, and advection. The model has been described in Chapter 2.

The model was used to investigate multiple phenomena. Examples of these phenomena are the photochemical Doppler effect, solar influence on mesospheric water vapor by Lyman-alpha radiation, autocatalytic water vapor production as a source of relatively large mixing ratios within the middle to upper mesosphere in high latitudes during summer, tertiary ozone maximum formation, and trends of mesospheric water vapor due to increase of methane and other minor constituents.

Different measurements have shown that large water vapor mixing ratios occur in the upper mesosphere at high-latitude summers under conditions of strong solar radiation. In this area, photolysis should effectively reduce the water vapor mixing ratio. The analysis of this finding by means of a three-dimensional model supplies evidence that water vapor is autocatalytically formed below a crossover height of about 65 km, transported upward and destroyed by photolysis above this altitude. The discussion of autocatalytic water vapor production is the subject of Chapter 3.

The intensification of agriculture and industry leads to injection into the atmosphere of such gases as methane, carbon dioxide, dinitrogen oxide. The anthropogenic changes of the troposphere are well studied but the impact on the mesosphere-lower thermosphere was not clarified. The influence of the rising concentrations of methane, dinitrogen oxide and carbon dioxide since the pre-industrial era upon the chemistry of the mesosphere was studied by the model and discussed in Chapter 4.

The spatio-temporal behavior of the ozone mixing ratio in the upper mesosphere/mesopause region under nearly polar night conditions is one of the phenomena not completely understood or reproduced by models thus far. The most marked features of the modeling results are a pronounced ozone maximum around 72 km occurring close to the polar night terminator during night and a strong drop of the mixing ratio above approximately 80 km. These features were also found by means of ground-based microwave measurements in high latitude at the Arctic Lidar Observatory for Middle Atmosphere Research (ALOMAR, 69.29° N, 16.03° E) and even at the moderate latitude of Lindau (51.66° N, 10.13° E) during nights in the winter season. This result was explained in terms of accumulation of ozone under twilight conditions with a reduced photolysis of water vapor and a small and permanently acting dissociation of molecular oxygen into atomic oxygen (which will be quickly converted into ozone). The comprehensive discussion of the question is the theme of Chapter 5.

The photochemical system of the mesosphere represents a nonlinear chemical oscillator enforced by diurnal periodic solar radiation. This oscillator can display such effects as period doubling cascades and other subharmonics or chaos. The nonlinear effects in MLT region are discussed in Chapter 6.

An ability to reproduce small-scale effects is significant for atmospheric modeling. One of such effects is Sudden Stratospheric Warming (SSW). It consists of a sudden increase of temperature in the stratosphere for high and middle latitudes in winter during a time range of 1 or 2 weeks with deceleration of zonal mean zonal flow, distortion and breakdown polar vortex. The impact of a stratospheric warming event upon minor constituents in the MLT region has been investigated by means of the model and discussed in Chapter 7.

Additionally, a submodel for calculation of chemical heating rates, and a submodel considering the relaxation of excited hydroxyl constituents were developed. These submodels can be applied for future studies and are considered in Chapter 8.

The last Chapter summarizes the results and shows the perspective for future development and improvements of the model.

Chapter 2

Model Description

The 3-dimensional Global Circulation Model (3D-GCM) presented here consists of two main parts: dynamical and chemical part. Figure 2.1 schematically shows the main blocks of the model. The Chemistry-Transport Model (CTM) consists of block for chemical calculations, block for calculations of eddy and molecular diffusive transport, and block for calculations of advective transport. The CTM part discussed below in Chapter 2.2 more comprehensively. The output of CTM is a 3-dimensional distribution of minor chemical constituents, which is transmitted into the dynamical part. The dynamical part calculates 3-dimensional fields of temperature and zonal, meridional and vertical winds. This 3d-distribution of dynamical data feed back into CTM. Two dynamical parts are possible for the calculations: COMMA-IAP (Cologne Model of the Middle Atmosphere of the Institute of Atmospheric Physics) and LIMA (Leibniz-Institute model of the Middle Atmosphere). The

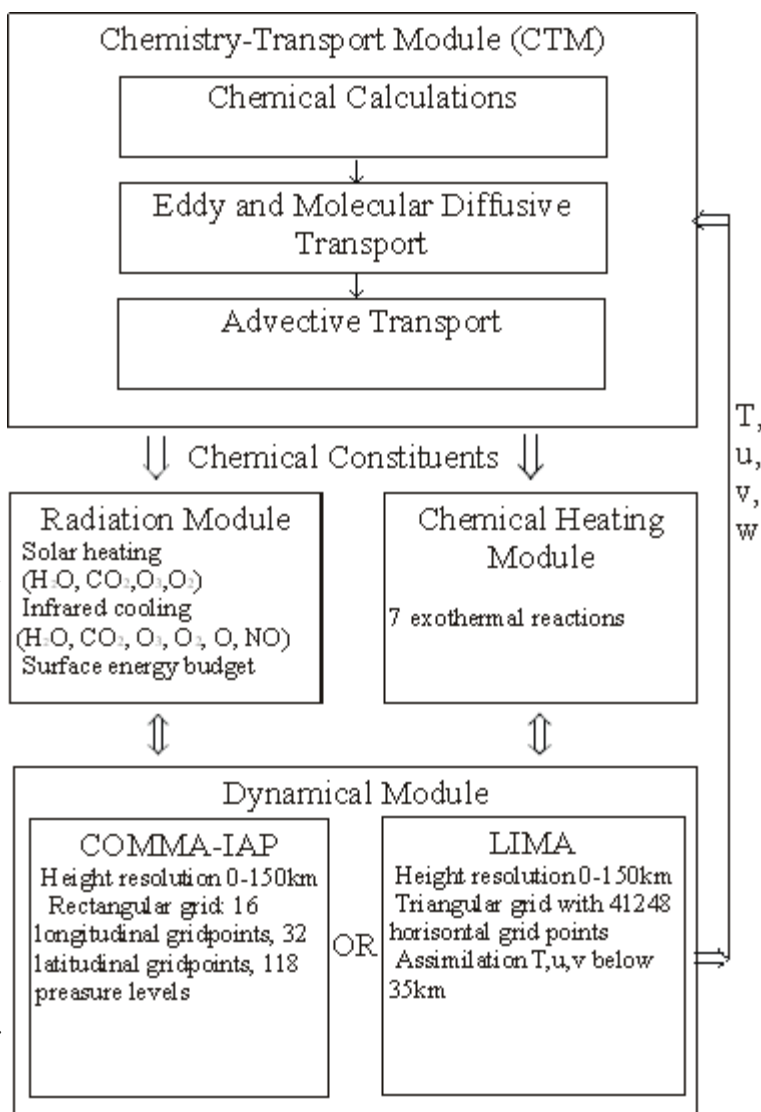


Figure 2.1. The scheme of 3D-GCM.

dynamical model COMMA-IAP is a climatologically mean model and LIMA is a model for realistic calculations for a given year and it is applied to different open scientific questions. The calculations which will be discussed in Chapters 3-7, 8.1 are done based on COMMA-IAP and in Chapters 7, 8.2 based on LIMA dynamics. The dynamical parts of the GCMs and the difference between them are described in Chapter 2.1.

2.1 Dynamic Model

The dynamical part of the models COMMA-IAP and LIMA are based on a model developed by Klinker [1981] and Rose [1983]. COMMA-IAP represents an improved version of the model COMMA-IAP described by Kremp et al. [1999], Berger and von Zahn [1999] and Körner [2002]. COMMA-IAP is based on spherical coordinates with a horizontal resolution of 5° in latitude and 22.5° in longitude. This corresponds to 36 steps in meridian direction versus 16 steps in zonal direction. The vertical grid of the model has an extension from the ground up to the lower thermosphere (0-150 km). Nonlinear (primitive) atmospheric equations are integrated in time steps of 225 s. The radiation code considers the EUV and X-ray spectrum of the solar radiation which reflects the main focus on the mesosphere and lower thermosphere. It also takes into account non-local thermodynamic equilibrium (non-LTE) parameterizations for absorption of solar radiation by O_2 , O_3 , H_2O and CO_2 , and infrared absorption and emission by O_3 , H_2O , CO_2 , NO and O . The model takes into account radiation calculations, which provide the radiative cooling and heating rates to drive the diabatic circulation of the model atmosphere. Parameterizations of the solar absorption in the UV and partly in the visible range consider the contribution of ozone and molecular oxygen as absorbers in the middle atmosphere and lower thermosphere. The values of the solar fluxes and absorption cross-sections are taken from the paper of Strobel [1978]. The actual energy available from direct solar heating is scaled by the stored potential chemical energy and the energy loss due to airglow emission according to Mlynczak and Solomon [1993]. Absorption of solar radiation by tropospheric water vapor and carbon dioxide in the near infrared range is calculated according to Lacis and Hansen [1974] and Liou [1980]. The cooling rates by terrestrial radiative flux divergence are computed by the use of water vapor, ozone, carbon dioxide, atomic oxygen, and nitric oxide from the CTM. The cooling rates due to carbon dioxide are computed using parameterizations of Kutepov and Fomichev [1993] and Fomichev et al. [1998], including effects from non-local thermodynamic equilibrium conditions. Gravity wave drag parameterization is employed as mechanical dissipation according to Holton and Zhu [1984]. In COMMA, at each time step the actual gravity wave momentum deposition is calculated near critical and breaking levels due to a family of gravity waves with horizontal phase velocities of 5, 25 and 50 m/s. The gravity wave diffusion coefficient is then used as the actual eddy diffusion parameter for calculating the vertical eddy transport of heat, the cooling due to the divergence of the vertical heat flux, and the heating from dissipation of turbulent gravity wave energy. The set of gravity wave parameters is chosen in such a way that typical breaking altitudes occur in the mesopause region. Owing to gravity wave momentum deposition on the mean flow, the model simulates realistic thermal behavior such as the cold summer mesopause having temperatures as low as 120 K or the two distinctive level structures of the mesopause [Berger and von Zahn, 1999]. The resulting net heating rates and momentum deposition drive the diabatic circulation in the model resulting in realistic wind systems [Kremp et al., 1999]. A detailed description of the dynamic part of the model is also given in Körner [2002].

LIMA is a hydrostatic global Eulerian grid point model integrating the set of nonlinear primitive atmospheric equations. The model extends from the ground to the lower thermosphere (0-150 km). A smoothed topography is included as a lower boundary condition of the geopotential. The vertical resolution is $\Delta z = 1.15$ km. The dynamical part of the model is based on a completely new model architecture compared with the older version (COMMA-IAP). All model versions were designed for investigations of the physical processes in the MLT region. The older versions, as mentioned above, are based on spherical coordinates. The disadvantages of these coordinates are the pole singularities and the non-equidistant grid point distances increasing toward the equator. This drawback has been overcome by the introduction of triangle (simplex) coordinates. The older versions are unable to model phenomena such as planetary waves or sudden stratospheric warmings (SSW). They only calculate climatological means of aeronomic parameters. The new model assimilates ECMWF (European Center for Medium-Range Weather Forecasts) data containing the information about planetary waves for both horizontal wind and temperatures below 35 km. The dynamic model then calculates the propagation of these waves into the MLT region and thus computes the current dynamical state in this domain. The same method is applied for sudden stratospheric warming events. A more detailed description of LIMA is given in Berger and Lübken [2006] and Berger [2007].

2.2 Chemistry-Transport Model (CTM)

A chemistry model was developed by Sonneman et al. [1984] and Fichtelmann and Sonnemann [1989] as a one-dimensional model with the lower boundary at 30 km and the upper boundary at 200 km. A chemical family concept was used grouping together the constituents with fast exchange reactions in order to solve the stiff ordinary differential equation (ODE) system for chemical constituents. Based on experience with one-dimensional models, a global three-dimensional model was developed as introduced in Appendix A. This model was designed to model the MLT region, focusing on the mesopause region. This region is the least studied domain of the entire middle atmosphere and requires careful modeling.

The chemistry-transport model consists of a chemical, a radiation and a transport code. The chemical code is based on the concept of chemical families [Shimazaki, 1985]. It considers three families subjected to transport: the odd oxygen (O , O_3 , $O(^1D)$), the odd hydrogen (H , OH , HO_2) and the odd nitrogen ($N(^4S)$, $N(^2D)$, NO , NO_2 , NO_3) families. The hydrogen compounds H_2 , H_2O , CH_4 and H_2O_2 , the so-called even hydrogens, are also subjected to transport. A simple code considers the impact of chlorine and bromine species that do not influence the chemistry of the mesosphere [Crutzen et al., 1995]. We include all relevant constituents and reactions in the CTM influencing the domain under consideration. The rate constants are taken from Atkinson et al. [1992], DeMore et al. [1990, 1997], Sander et al. [2003], and a few three-body reactions from Hampson [1980]. The radiation code is taken from Sonnemann and Fichtelmann [1989], Sonnemann et al. [1998] and Röth [1992]. It combines a code developed for the thermosphere-mesosphere with a code developed for the stratosphere. The transport code considers both advective and diffusive (turbulent and molecular) transport. One of the problems of numerical modeling is the uncertainty in advection transport due to finite difference approximation. Henceforth we call this uncertainty “numerical diffusion”. There are schemes that reduce the diffusivity of the transport scheme [e.g. Smolarkiewicz, 1983; Prather, 1986; Bott 1989; Bott, 1992]. However, these schemes did not suppress it sufficiently, particularly under conditions of steep concentration gradients. A large diffusivity influences the distribution of minor constituents such as water vapor within the mesopause region. Because of this, the water

vapor mixing ratio in the area of noctilucent clouds (NLC) under specific constraints (83 km at high latitudes in summer) calculated by employing the Smolarkiewicz scheme amounted to about 4 ppmv [Körner and Sonnemann, 2001]. A newly developed advective transport scheme that is almost free (nearly zero) of numerical diffusion is applied in the model [Walcek and Aleksic, 1998; Walcek, 2000]. The eddy diffusion coefficient reflects chaotic processes of the airflow (for example the breaking of gravity waves) that cannot be resolved in the frame of the dynamic model. The eddy diffusion coefficient is an external parameter for the model. It depends on height, latitude, season, and local time. There are different estimations and measurements and indirect hints on the magnitude of the diffusion coefficient [Hocking, 1990; Lübken, 1997]. For calculations we use our standard eddy diffusion profile based on results by Lübken [1997]. The Thomas algorithm for vertical diffusion parameterization is applied in the model [Morton and Mayers, 1994].

2.2.1 Chemical Code

The elemental parts of the chemistry are listed below.

- The chemical species used in the model: H, OH, HO₂, H₂O₂, H₂, H₂O, CH₄, O, O(¹D), O₃, N, NO, NO₂, NO₃, N₂O, Cl, ClO, Br, BrO, CO, CO₂.
- Constituents subject to advective transport are: H_x, NO, O, O₃, H₂O, CH₄, N₂O, H₂, CO, CO₂, Cl_x, Br_x.
- Constituents subject to diffusive transport are: O, O₃, H_x, H₂O, CH₄, N₂O, H₂, N, NO, NO₂, NO₃, CO, CO₂, Cl_x, Br_x.
- The reaction scheme includes 56 individual chemical reactions.
- 14 photodissociation rates reflect the diurnal variation of the daylight dependent reactions.
- The chemical families are:

H _x	H + OH + HO ₂ + H ₂ O ₂
O _x	O + O(¹ D) + O ₃
NO _x	N + NO + NO ₂ + NO ₃
Cl _x	Cl + ClO
Br _x	Br + BrO

2.2.2 Radiation Code

The main part of the diurnal variation in chemistry results from the change of the zenith angle of the sun at the grid point and depends on sort of molecules. The radiation code used is the same as in the paper by Sonnemann et al. [1998a]. The code was primarily developed by Fichtelmann and Sonnemann [1989] for use in mesospheric and thermospheric modeling and considers the EUV and X-ray spectrum of the solar radiation. The lower mesospheric rates were revised by Kremp et al. [1999] by implementing a code developed by Röth [1992] for stratospheric modeling. The annual variation due to the eccentricity of the earth's orbit is

approximated by a sine function with amplitude of 3.5% of the calculated rates. Absolute variation is 7% between summer hemisphere and winter hemisphere.

The radiation code is running offline, meaning that it uses fixed absorber concentrations for the calculation of the photodissociation rates. The photodissociation rates in a model run are taken from the precalculated library and the actual rates depend on height and zenith angle of the sun at the grid points. Due to small variations in the mesospheric photolysis rates of the minor constituents, this is a possible first approximation. The procedure described above saves computational time; however, for full interactive coupling with the dynamic module it should be revised to use actual absorber concentrations. Additionally, the dissociation rate of water vapor has been revised [Grygalashvily and Sonnemann, 2005] according to the correction of the Lyman-alpha radiation by Woods et al. [2000]. The reactions of photodissociation used in the model are listed in Appendix D.

2.2.3 Diffusion Code

In the model, diffusive transport is divided into turbulent and molecular parts. The small scale turbulent mixing cannot be resolved by the grid structure of the model. It is parameterized by the concept of eddy diffusion. The atmospheric motion can be considered as a large number of eddies of different scales in horizontal and vertical directions. In the CTM the eddy and molecular diffusion are calculated with only a one-dimensional eddy and molecular diffusion coefficient for the vertical coordinate. This restriction is justified as the atmosphere is advection determined in horizontal directions and it agrees with the state-of-the-art model treatment. It is important to note that the eddy diffusion profile is an external quantity in the chemical model; meaning that, to a certain extent, it can tune the model output. In the real atmosphere, the eddy diffusion coefficient at a constant height depends on season, latitude and local time. However, for the present model, an idealized standard eddy diffusion profile based on measurements by Lübken [1997] was used for all seasons.

Vertical mixing in the stratosphere is slow but is still faster than the mixing by molecular diffusion. In the mesosphere, vertical turbulent mixing becomes increasingly faster with height and is still larger than the molecular diffusion growing exponentially with altitude. In the thermosphere, above the height region where gravity waves break - the so-called turbopause (the altitude of Earth's atmosphere where the eddy diffusion coefficient equals the molecular diffusion coefficient) - the separation of constituents by molecular diffusion is stronger than mixing by turbulent diffusion. This region is termed the heterosphere. The molecular diffusion becomes important at about 90 km and is dominant above 100 km. For light atoms and molecules (especially H_2 , H and O), the mixing ratios begin to increase, meaning their relative contribution increase. The molecular diffusion coefficient roughly depends inversely on the molecular weight, and thus each species possesses its own turbopause. In the model the molecular diffusion coefficients were computed according to the formula given in the U. S. Standard Atmosphere [1976] or in Banks and Kockarts [1973], depending on the air density, the temperature resulting from the dynamic part of the model and a specific constant mainly determined by the molecular weight.

2.2.3.1 Eddy Diffusion

According to Colegrove et al. [1965] the vertical flux of the molecules of the i 'th gas species is given by

$$n_i \cdot u_i + D_i \cdot \left(\frac{dn_i}{dz} + \frac{n_i \cdot (1 + \alpha_i)}{T} \cdot \frac{dT}{dz} + \frac{g \cdot n_i \cdot M_i}{R \cdot T} \right) + K \cdot \left(\frac{dn_i}{dz} + \frac{n_i}{T} \cdot \frac{dT}{dz} + \frac{g \cdot n_i \cdot M_i}{R \cdot T} \right) = 0 \quad (2.1)$$

where n_i is the number density of the i th gas species, R is the universal gas constant, D_i is the height-dependent molecular diffusion coefficient of the i 'th species diffusing through N_2 , α_i is the thermal diffusion coefficient of the i 'th species, M_i is the molecular weight of the gas through which the i 'th species is diffusing (for the major species N_2 , M has the value 28.0134 kg/kmol), and K is the height-dependent eddy diffusion coefficient.

At each grid point of the model, the number density of air changes with temperature according to the ideal gas law. The calculations of diffusive fluxes are done in terms of the mixing ratios of the constituents in order to get better accuracy. The number density of the air is important in the chemical code for the termolecular (three-body) reactions. A change in temperature results in a change of the production and loss rates for several constituents.

The derivation for the calculation in mixing ratios and dz from log-pressure coordinates is shown below for eddy diffusion and for molecular diffusion, which is a bit more complex. Both are combined and solved in the model by the implicit Euler differentiation and the use of the Thomas algorithm [Morton and Mayers, 1994].

The calculation of temperature and wind speed by COMMA-IAP or LIMA is done under the assumption that the atmosphere is in diffusive equilibrium. For diffusive equilibrium, the flux induced by eddy diffusion for the number density of the air is given by

$$\Phi_k = -K \left(\frac{\partial n}{\partial z} + n \left(\frac{1}{H} + \frac{\partial \ln T}{\partial z} \right) \right) = 0 \quad (2.2)$$

With a nonzero eddy diffusion coefficient, the underbraced term in 2.2 has to be zero. This is the equivalent formulation to the use of log-pressure coordinates as used in COMMA-IAP and LIMA.

With equation (2.2) the equation below is used to calculate the effect of the eddy diffusion

$$\frac{\partial f_i}{\partial t} = K \frac{\partial^2 f_i}{\partial z^2} + \frac{\partial f_i}{\partial z} \left(\frac{\partial K}{\partial z} - K \left(\frac{1}{H} + \frac{\partial \ln T}{\partial z} \right) \right) \quad (2.3)$$

The derivation of the equation (2.3) can be found in appendix B.

2.2.3.2 Molecular Diffusion

According to U. S. Standard Atmosphere [1976] the flux due to molecular diffusion for the i 'th gas species can be written

$$\Phi_{D_i} = -D_i \left(\frac{\partial n_i}{\partial z} + n_i \left(\frac{1}{H_i} + (1 + \alpha_i) \frac{\partial \ln T}{\partial z} \right) \right) \quad (2.4)$$

where D_i stands for the height-dependent molecular diffusion coefficient of the i 'th species diffusing through the gas for the major species N_2 (according to Table 3 in U. S. Standard Atmosphere [1976]), n_i is the number density of i 'th gas species, H_i represents the individual scale height for the i 'th component and a_i is the thermal diffusion coefficient of the i 'th species. The individual scale height H_i for each component can be expressed in terms of the mean scale height

$$H = \frac{RT}{Mg} = \frac{kT}{mg}, \quad H_i = \frac{kT}{m_i g} = H \frac{m}{m_i}, \quad (2.5)$$

where M is the mass of one mole of air molecules, m represents the average mass of a single molecule, R is the universal gas constant ($R = kN_A$) and k is Boltzmann's constant. N_A stands for Avogadro's constant, m_i is the mass of the single molecule of i 'th species. The height variation for m and g are small in the lower and middle atmosphere. Therefore, H changes mainly with the change of temperature, and constant scale height means constant temperature in the first approximation. Both models under consideration (COMMA-IAP and LIMA) use log-pressure coordinates with a constant scale height of $H = 7$ km.

The molecular diffusion coefficients are proportional to temperature, and inversely proportional to the number density of air.

$$D_i = \alpha_i \frac{T^\beta}{n} = \frac{\hat{D}_i}{n}. \quad (2.6)$$

The species dependent coefficients α_i and β_i are taken from U. S. Standard Atmosphere [1976].

The equipartition law of the kinetic theory of heat $\frac{m}{2} u^2 = \frac{3}{2} kT$ gives us the ability to derive

the appropriate values of molecular diffusion coefficients for all molecules from the table of U. S. Standard Atmosphere [1976], because the root mean square of the velocity is proportional to the molecular diffusion coefficient. The coefficient $a(H_2)$ is calculated from the value $a(H)$; while all other components are calculated from the values of $a(O)$ and $a(O_2)$, depending on which molecular weight is closer to the molecular weight of the considered component.

$$a(H_2) = a(H) \sqrt{\frac{m(H)}{m(H_2)}}, \quad a_i = a(O) \sqrt{\frac{m(O)}{m_i}} \quad \text{or} \quad a_i = a(O_2) \sqrt{\frac{m(O_2)}{m_i}}. \quad (2.7)$$

The equation below is used to calculate jointly the effect of the eddy and molecular diffusion. Its derivation can be found in Appendix C.

$$\begin{aligned} \frac{\partial f_i}{\partial z} &= \frac{\partial^2 f_i}{\partial z^2} (K + D_i) \\ &+ \frac{\partial f_i}{\partial z} \left(\frac{\partial K}{\partial z} - K \left(\frac{1}{H} + \frac{\partial \ln T}{\partial z} \right) + D_i \left(\beta_i \frac{\partial \ln T}{\partial z} + F_i(T) \right) \right) + f_i D_i \left(\beta_i \frac{\partial \ln T}{\partial z} F_i(T) + \alpha_i \frac{\partial}{\partial z} \left(\frac{\partial \ln T}{\partial z} \right) \right). \end{aligned} \quad (2.8)$$

The structure of equation (2.8) allows very fast calculation of the diffusion terms and high precalculation for the terms of the innermost loop, resulting in a fast computer code with a high degree of vectorization.

2.2.4 Advection

In numerical modeling of atmospheric phenomena it is often necessary to solve the advection equation for non-negative definite scalar functions. For this purpose a number of advection schemes were developed [Prather, 1986; Smolarkiewicz, 1973; Bott, 1989; Bott, 1992; Walcek and Alekxis, 1999; Walcek, 2000]. The continuity equation describing the transport of the nondiffusive quantity $\psi(x, y, z, t)$ in a flow field is given by

$$\frac{\partial \psi}{\partial t} = -\nabla \cdot (\vec{V} \psi), \quad (2.9)$$

where $\vec{V} = (u, v, w)$ is the velocity vector, and x, y, z, t are the space and time coordinates. For atmospheric transport x and y are expressed by spherical coordinates, and u and v are the velocity components in the corresponding direction of the spherical coordinate system. The change of the quantity per time interval in a grid box must be equal to the flux through the boundaries if there are no sources and sinks. Equation (2.9) can be transformed into

$$\frac{\partial \psi}{\partial t} + \vec{V} \cdot \nabla \psi + \psi \nabla \cdot \vec{V} = 0. \quad (2.10)$$

For an incompressible fluid the divergence of the wind speed is equal to zero which simplifies equation (2.10). For a compressible fluid like the atmosphere, a similar simplification $\nabla(\rho \vec{V}) = 0$ can be achieved by the use of log-pressure coordinates as used in COMMA-IAP and LIMA. The vertical velocity w is calculated in COMMA-IAP according to the hydrostatic law

$$\frac{1}{r \cos \phi} \frac{\partial}{\partial t} (v \cos \phi) + \frac{1}{r \cos \phi} \frac{\partial u}{\partial \lambda} + \frac{1}{\rho_0} \frac{\partial}{\partial z} (\rho_0 w) = 0, \quad (2.11)$$

with $\rho_0(z) = \rho_s \exp(-z/H)$, where ρ_s is the density at $z = 0$. For a detailed description also see Holton [1992] and Berger [1994]. Equation (2.10) with $\nabla(\rho \vec{V}) = 0$ is reduced to

$$\frac{\partial \psi}{\partial t} + \vec{V} \cdot \nabla \psi = 0. \quad (2.12)$$

If an air parcel at a level of constant pressure is heated by radiation, the air expands and a divergent flow follows as long as the expansion process takes place. The formulation of equation

(2.11), however, is equivalent to $\nabla \cdot \rho \vec{V} = 0$, and so equation (2.12) is for the advective transport equivalent to equation (2.9) and can be used for the calculation of advective transport by the use of mixing ratios.

For the one-dimensional case equation (2.12) is reduced to

$$\frac{\partial \psi}{\partial t} + u \frac{\partial \psi}{\partial x} = 0. \quad (2.13)$$

It can be shown that for all initial values a general solution of the form

$$\psi(x, t) = \zeta(x - ut) \quad (2.14)$$

exists and is equivalent to a wave that propagates in the positive x -direction [Haltiner, 1980]. The lines $x - ut = \text{const}$ are called the characteristics of the advection equation.

However, for a real atmosphere no analytic solution of this equation exists. Numerical advective schemes have to be used to calculate transport effects. These schemes have to fulfill some requirements. First of all, they must fill the requirement of monotonicity, which means that the advection scheme should not produce new extreme in the distribution of the constituents. Secondly, the scheme should be mass conserving, which means there should be no sources or sinks created by the mathematical algorithm. Another requirement is stability, i.e. the solution should converge against finite values over a long integration period. Also, the scheme should be positive definite, i.e. there should be no negative concentrations or mixing ratios in the solution. And last, but no less significant, the scheme should be marked by small numerical diffusion, i.e. concentration gradients should be conserved in the process of advection and should not be overly smoothed with time.

2.3 Improvements

2.3.1 Walcek Scheme

As mentioned in Chapter 1, the old version of the COMMA-IAP was decidedly too diffusive. Particularly, the strong vertical tidal winds being one order of magnitude larger than the mean wind created enormous problems in the extended mesopause region so that gradients of the mixing ratio decrease artificially. This concerned, among other variables, the atomic oxygen and water vapor mixing ratios - constituents marked by strong gradients. This was, of course, an unsatisfactory situation. As all models enumerated in Chapter 1 use the same or a similar diffusive transport scheme, it is not surprising that the published results showed clearly smoothed structures in the mixing ratios if they have too large wind [Smolarkiewicz, 1983; Prather, 1986; Bott, 1989, 1992]. Thus it was the main demand that any improved model should reduce the numerical diffusion of the advective transport scheme.

The numerical diffusion is a consequence of the discrete gridpoint structure. In order to integrate the system the differential quotients are approximated by difference quotients. By expanding the difference quotient of the advective transport term into a Taylor series, the second Taylor coefficient has the mathematical form of a diffusion term. This term determines the so-called numerical diffusion coefficient which reads as $z|w|/2$ with z being the height

resolution of the model and w being vertical velocity. A simple estimation shows that the numerical diffusion can exceed the turbulent diffusion coefficient, especially for the tidal wind component. For example, if the height resolution is $z \approx 2$ km and $|w| \approx 10$ cm/s, then 10^6 cm²/s that is the order of strong eddy diffusion. The estimation makes clear that a transport scheme characterized by small numerical diffusion is necessary to get reliable results. The Walcek scheme is marked by almost zero numerical diffusion. The scheme was introduced by Walcek and Aleksic [1998] and Walcek [2000]. Walcek scheme description can be found in Appendix D.

Figure 2.2 illustrates general algorithm for 1-dimensional case. The mixing ratios and velocities used as input data for subroutine which calculates transport by advection. The dimensionally depended “densities” precalculated. At the first step, the subroutine identifies local extremum and specifies mixing ratio limits at new time for a given direction. The next step, the subroutine updates mixing ratios and upstream fluxes only for the cells where $u \geq 0$. At the last step, the subroutine updates mixing ratios and fluxes only for the cells where $u < 0$. The calculation cycle is repeated for all dimensions.

There are two problems of employing the scheme in the model. The first is the problem of singularity and the second concerns the boundary conditions at both poles. In order to solve the problem of the boundary conditions we use the additional index i_p . The index runs opposite

over the pole values to index i , which numerates grid points along longitude. In other words, we use for the transport over the pole grid points that are symmetric to each other relative to the pole.

In the Walcek scheme for vertical transport we need additional velocities and fluxes at one cell below the lower boundary and one cell above the upper boundary. We quadratically extrapolate the values of the fluxes and velocities.

A possible mistake in implementing this scheme is incorrectly specifying the changing fluid densities during multi-dimensional calculations. The problem is that the monotone limiters (see Appendix D) used by this advection algorithm will “check” a totally worthless updated mixing ratio resulting from using erroneous fluid densities. Problematically, we never know if we have passed incorrect fluid densities to the code as it gives reasonable looking answers (no infinities, negatives etc.). So, an extremely valuable test of whether we have correctly loaded densities, winds, and mixing ratios into this algorithm is to run the code using constant mixing ratios everywhere, but with monotone limiter statements turned off. In other words, we let the scheme calculate a nonmonotonic behavior. As formulated, this algorithm is algebraically

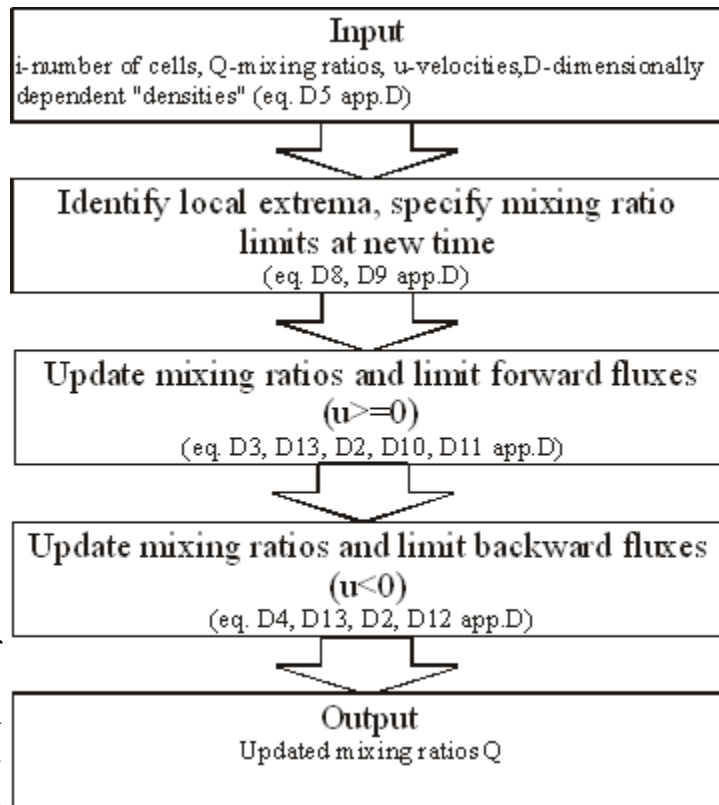


Figure 2.2. The general scheme of algorithm for 1-dimensional case.

guaranteed to never generate an updated mixing ratio different from the constant if constant mixing ratios are initially specified for a given domain. Such test was done with positive results, meaning monotone limiters were turned off and calculation with such statements have remained constant mixing ratios.

2.3.2 Water Vapor Photolyses Rate

A key component of chemistry quality modeling is the correct estimation of photodissociation reaction rates (or photolysis rates). Photolysis rates depend on the intensity of solar radiation in the atmosphere and the molecular properties of the molecule undergoing photodissociation. Water vapor photolysis is the main source of hydrogen radicals in the MLT domain influencing the odd oxygen distribution especially within the mesosphere. The water vapor dissociation rate above approximately 70 km altitude is mainly determined by Lyman-alpha radiation. Below this height, the radiation contribution of the Schumann-Runge bands becomes increasingly important. The solar Lyman-alpha radiation varies strongly with solar activity by an approximate maximum factor of two between solar activity minimum and maximum [Simon, 1981; Woods et al., 2000], whereas the radiation of the Schumann-Runge bands varies at their maximum only by a few percent [London et al., 1984; Lean, 1984]. The later variation is on the order of the variation caused by the eccentricity of the earth's orbit (7%). Lastly, based on UARS measurements, an average value of the solar cycle variation of Lyman-alpha was estimated by a factor of 1.5 [Woods et al., 2000]. This value is smaller than the older estimation by Vidal-Madjar [1977], who published a factor of two between solar minimum and maximum (from 2 to $4 \cdot 10^{11}$ phot. $\text{cm}^{-2} \text{ s}^{-1}$). The change of the value of the mean Lyman-alpha irradiance from 3 to about $4.65 \cdot 10^{11}$ phot. $\text{cm}^{-2} \text{ s}^{-1}$ (3.7 to $5.6 \cdot 10^{11}$ phot. $\text{cm}^{-2} \text{ s}^{-1}$ averaged over 2 years from solar min to solar max) is more important because it influences the H_2O dissociation rate, increasing it by more than 50% relative to the older value. In our calculation, we use a maximum variation of a factor of two in order to show a maximum response [Vidal-Madjar 1975; Simon, 1981].

The solar rotation period of 27 days encompasses typical features in the photolysis rate of water vapor. The variation of the Lyman-alpha radiation within a 27-day period may be at a maximum in the order of 30% [Vidal-Madjar and Phissamay, 1980; Woods et al., 2000]. However, the latest estimated average value is 9% [Woods et al., 2000]. As the absorption cross-section of the main absorber O_2 for the Lyman-alpha radiation is essentially higher than the corresponding one for the Schumann-Runge bands, a marked variation of the water vapor dissociation rate only occurs above approximately 70 km.

Below this domain, the oxidation of H_2O by $\text{O}(^1\text{D})$ becomes increasingly important compared with photolysis, but it does not strongly vary within the solar cycle. Considering that water vapor mixing ratios decrease with increasing height above the maximum at 50 - 70 km, and regarding its aeronomic importance, one finds that the strongest impact of solar activity upon atmospheric chemistry occurs within the extended mesopause region (approx. 70-100 km). Above this domain the water vapor mixing ratios are too small and the chemistry is too slow compared to the transport processes; below this region the variation of the dissociation rate within the solar cycle is strongly reduced. Thus, variation of the Lyman-alpha radiation has strongest influence upon the region 70-100 km, that is also the region of PMSE and NLC. Therefore, it can have an influence on the occurrence rate of these phenomena.

The influence of the 11-year solar activity cycle variation on the chemistry of the mesosphere/lower thermosphere, and particularly on the water vapor distribution, was

investigated (see Chapter 3). In order to simulate a 11-year solar cycle, Lyman-alpha radiation was parameterized by the expression

$$J_{H_2O}^{new}(z, \chi, t) = J_{H_2O}^{old}(z, \chi, t) + Ly(t) \cdot \sigma_{H_2O} \cdot \exp\left[-10^{-20} \cdot n_{O_2}(z) \cdot \overline{H(z, \chi)} \cdot \sec \chi\right], \quad (2.15)$$

where J^{new} dissociation rates for water vapor with applying of variation of Lyman-alpha radiation, depend on time t , zenith angle χ and height z . J^{old} - dissociation rates for water vapor with minimum of Lyman-alpha radiation. $Ly(t)$ stands for the number of photons, and $\sigma_{H_2O} = 1.4 \cdot 10^{-17} \text{ cm}^{-2}$ corresponds to the dissociation cross-section for H_2O by Lyman-alpha. The exponential expression represents the Beer-Lambert law, including the Lyman-alpha absorption by O_2 as the only efficient absorber, and the column density of O_2 at a solar zenith angle depending on a mean density scale height of O_2 . By means of the Expression (2.15), we investigated the impact of changing Lyman-alpha radiation on the chemistry of the MLT region. In order to carry out trend calculations we had to reproduce the Lyman-alpha radiation for a period since, at least, the beginning of NLC observations in 1883. This problem will be discussed in context with the trend calculations in Chapter 4.

Chapter 3

Modeling of Global Water Vapor

3.1 Results and Comparison with Observations

Water vapor is an important constituent for the upper atmosphere. It is the source for hydrogen radicals OH and H which destroy ozone and, thus, indirectly influence on the absorption of ultra-violet radiation. Water vapor plays a role in the cooling of the mesosphere region by emission of long-wave radiation. In the mesopause region there are some phenomena, for example NLC, PMSE or airglow emission in the Meinel bands, which are correlated to the concentration of water vapor. To understand these phenomena, a detailed knowledge of the climatology of water vapor is desirable. Responding to importance of water vapor many measurements were done and published in papers during last years.

The most important observations for the purpose of comparison with the modeled water vapor distribution of this work are the microwave measurements by Seele and Hartogh [1999] as it was done at high latitudes - the region which is interesting from point of view of NLCs (Noctilucent Clouds) and PMSEs (Polar Mesospheric Summer Echoes) study, and HALOE (HALogen Ocultation Experiment) which is a satellite measurement and shows seasonal and latitudinal distribution of water vapor. Thus, in this work comparisons with observations mentioned above will be presented.

The microwave observations were carried out at ALOMAR (Arctic Lidar Observatory for Middle Atmospheric Research, Andoya, Norway, 69° N, 16° E), where also temperature observations by lidar and by falling spheres from rockets were made. Seele and Hartogh used an average of 24 h of the measured signal at 22.235 GHz which confines the measurements to an altitude of about 80 km. An average over one week allows a retrieval of water vapor data up to 85 km. Above that height the measurement noise error and the influence of the a priori-profile (a first guess of the vertical distribution of water vapor which is needed for the inverting of the data) increase strongly. The microwave measurements at ALOMAR are carried on continuously since 1997. For detailed description of microwave spectroscopy and the integration of the signal see Hartogh and Jarchow [1995], Seele and Hartogh [1999], Seele [2000].

Figure 3.1 shows microwave water vapor measurements at ALOMAR [Seele and Hartogh, 1999]. They found a pronounced annual cycle at northern high latitude with a maximum in water vapor mixing ratio between May and September/October and a higher annual variability than at midlatitudes. There is no semiannual cycle at the northern high latitudes. The water vapor measurements (Figure 3.1) are in good agreement with the modeling results calculated by COMMA-IAP (Figure 3.2). Both display the known seasonal variation at high latitudes. Highest values occur from May to September, lowest values from January to April. The summer

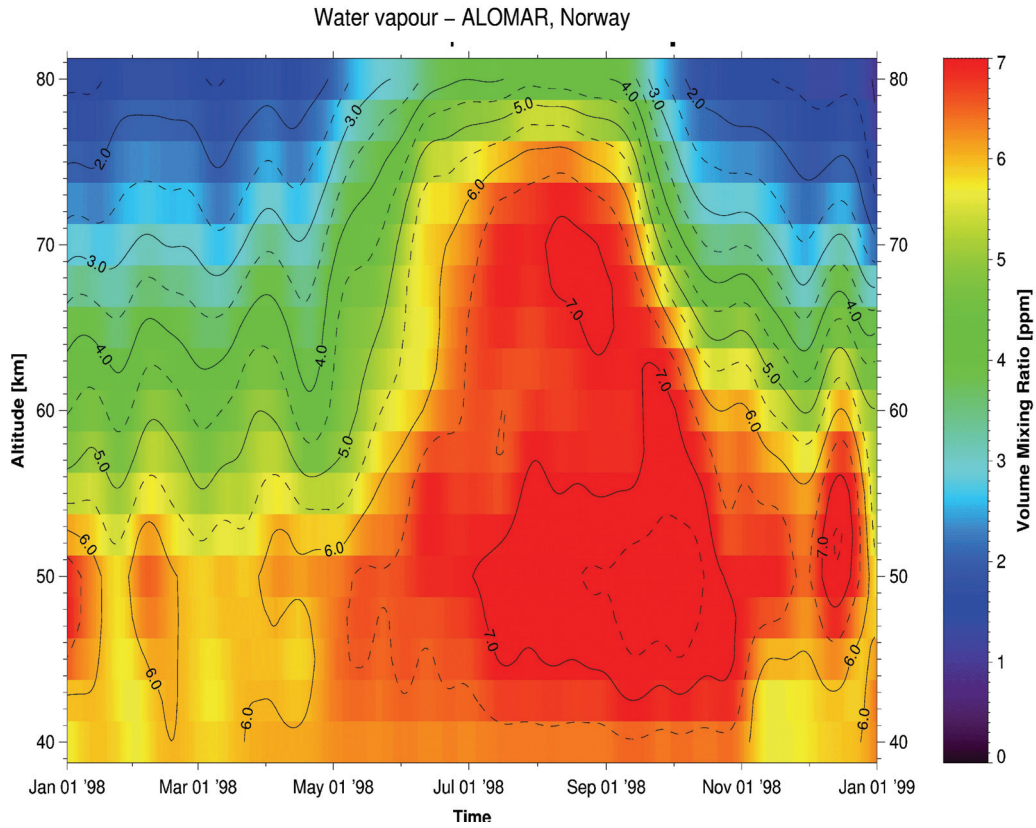


Figure 3.1. Microwave measurements of water vapor mixing ratio [ppmv] at ALOMAR (69°N, 16° E)

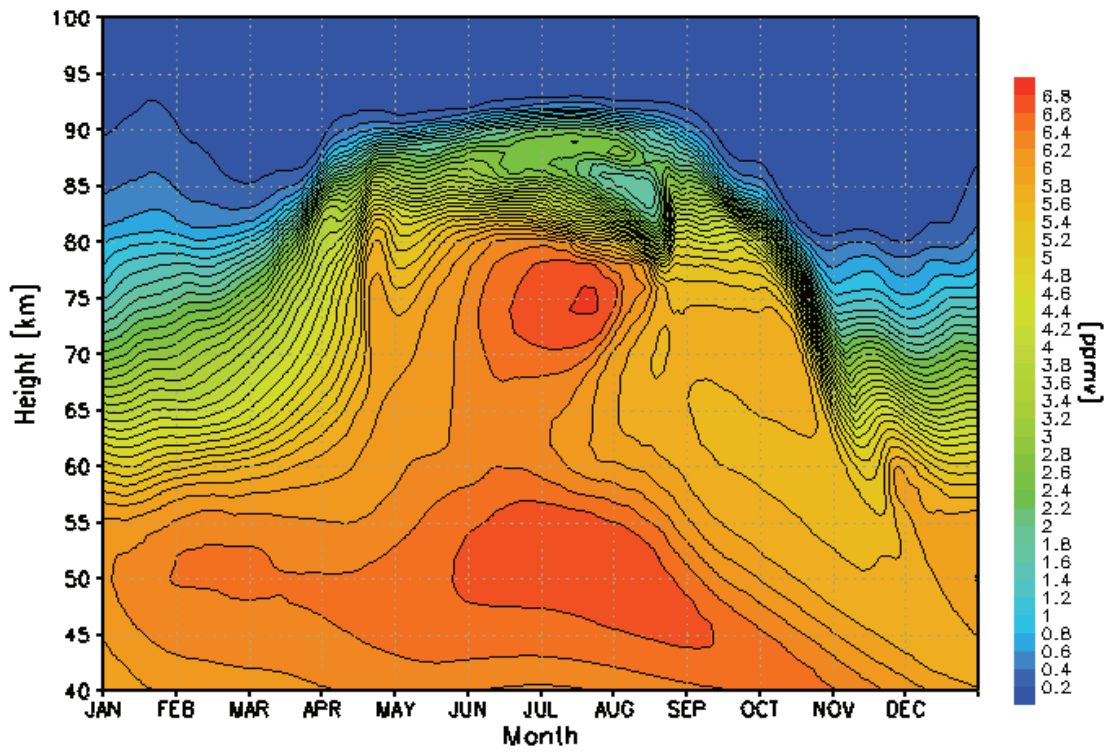


Figure 3.2. Water vapor mixing ratio [ppmv] at 67.5° N for mean solar activity.

maximum in the upper mesosphere occurs in the end of June - beginning of August. Both, measurements and modeling show double maximum structure for this period. This feature is discussed below in section 3.3 of this chapter. An absolute maximum in the mixing ratio of 6.5-7 ppmv occurs in the upper stratosphere-lower mesosphere during September and October. All described features for the high latitudes water vapor cycle agree well with the microwave observations of Seele and Hartogh in Figure 3.1.

As it was mentioned, the latitudinal distribution of model output can be compared with HALOE experiment. Figure 3.3 exhibits the result of calculations for water vapor mixing ratio of the mesosphere in a latitudinal section near north spring equinox (30 March) under conditions of low solar activity. The influence of Lyman-alpha radiation and 11-year solar activity will be discussed below in section 3.2 of this chapter. To the south of the equator a low latitudes water vapor peak occurs at a relatively high altitude just around 70 km. Two other peaks right and left of that are located in the high southern and northern latitudes slightly below (south) and around (north) the stratopause. The southern peak lies at somewhat higher latitudes than the northern one. Figure 3.4 shows the model output for the south summer solstice (10 January). The most marked pattern consists of the enhanced water vapor mixing ratio in mean to high summer latitudes of the southern hemisphere. In the vicinity of 60°S a strong maximum with values slightly below 7 ppmv occurs above the stratopause. However, an area of large mixing ratios 6.3-6.9 ppmv in even higher latitudes reaches up to 80 km and even touches the NLC region. The cause consist in a strongly accelerated upward wind in summer and in autocatalytic water vapor production which will be discussed below in section 3.3 of this chapter. The water vapor local maximum in midlatitudes near the stratopause of the winter hemisphere (Figure 3.4) and the general increase of the contour lines from north to south with an amplified rise close to the polar

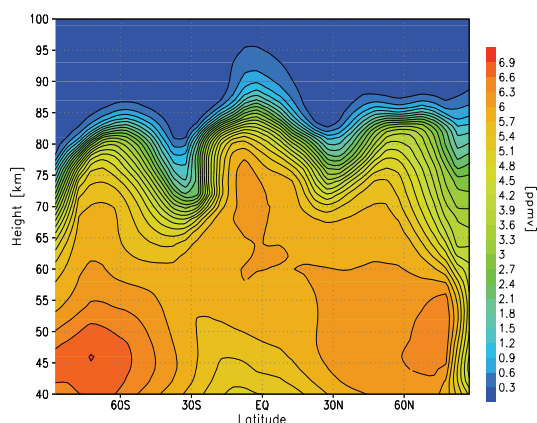


Figure 3.3. Latitudinal section of the water vapor mixing ratio for north spring equinox calculated by means of COMMA-IAP.

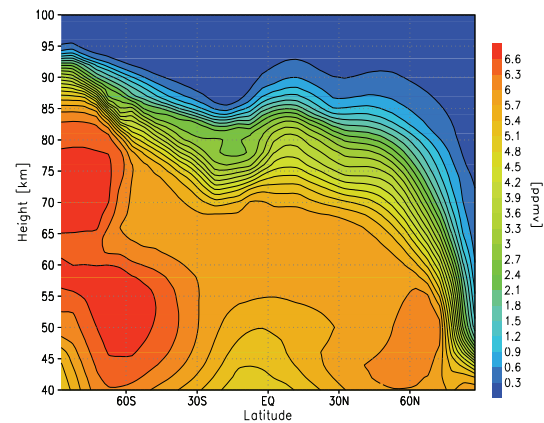


Figure 3.4. Latitudinal section of water vapor mixing ratio for south summer solstice calculated by means of COMMA-IAP.

day terminator is typical for the water vapor distribution in this season.

Very similar features were observed by HALOE, for example, in 1996 during the year of low solar activity, as Figures 3.5 and 3.6 demonstrate. The very strong maximum of water vapor mixing ratio with values larger than 7.4 ppmv exists near the equatorial region around 70 km during north spring equinox (Figure 3.5). The summer hemisphere at mean and high latitude is characterized by a double maximum structure with values of water vapor mixing ratio larger than 6.6 ppmv and a clear minimum around 60-65 km (Figure 3.6). The comparison between the model calculations and HALOE observations generally agrees well (see Figures 3.3 -3.6), but also revealed some differences. Although the principal patterns are very similar, the calculations

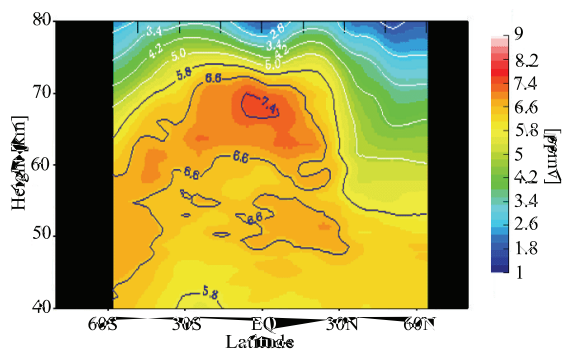


Figure 3.5. Water vapor mixing ratio [ppmv] for low solar activity (1996) for north spring equinox observed by HALOE from March 16th till April 15th with beginning on the left.

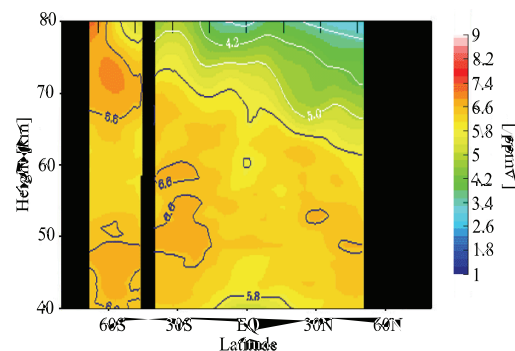


Figure 3.6. Water vapor mixing ratio [ppmv] for low solar activity (1995/1996) for south summer solstice observed by HALOE from December 12th, 1996 till January 18th, 1997 with beginning on the left.

show somewhat smaller water vapor mixing ratio (up to 0.7 ppmv) in the upper domain than the HALOE measurements. The model reflects a climatological mean for a certain solar activity whereas the HALOE observations correspond to an individual year. The data presented in HALOE observations are a latitudinal-seasonal combination over about a month whereas the results of model calculations correspond to a fixed date. There is no sense to change the model output according with HALOE measurements as it just embarrass subsequent analysis and the comparison is not a main point of this work. The lower boundaries for the total hydrogen mixing ratio are about 7.5 ppmv in H_2 equivalents. An increase of this value would also raise the total hydrogen mixing ratio below 70 km. However, there is a discrepancy between the WVMR observed by HALOE and that measured by other techniques. Using microwave measurements at low latitudes Nedoluha et al. [1996] found WVMR that were systematically smaller in the upper mesosphere compared to the HALOE data but larger below that domain. In addition, Seele and Hartogh [1999] confirmed this finding with observations at high latitudes using the same technique. This finding also was confirmed by Nedoluha and Hartogh [2000] comparing all available measurements of mesospheric water vapor. They found that the HALOE measurements provided too large mixing ratios in the upper mesosphere. As mentioned above, the model reproduce similar to the measurements seasonal and latitudinal distribution of water vapor. Further, some special questions will be discussed.

3.2 Dependence on Solar Activity

The response to the solar cycle variation over entire solar cycle of 11 years was investigated for different constituents at different altitudes and latitudes. Each model run yields a great deal of information. In this subchapter only some exemplary results are shown. All following figures are drawn by using one value per 5 days. The general response in the model on the variation of solar activity is as expected from the theory. There is a close anticorrelation between solar activity and water vapor concentration, at least down to 80 km. Below 70 km the behavior of water vapor is more indifferent or even slightly inverse and sometimes shows a certain phase delay between solar activity and atmospheric response. The optical depth of unity of the Lyman-alpha radiation ranges close to 75 km and increases rapidly below this altitude. The

domain of autocatalytic water vapor formation lies below 65 km so that only a small positive correlation can result from the variable Lyman-alpha radiation, meaning an increase of water vapor with rising radiation. The rise of the air pressure at high latitudes in summer raises the domain of autocatalytic water vapor formation by a few kilometers.

Figure 3.7 depicts the relative difference of the zonally averaged H_2O mixing ratio between low and high solar activity for the south summer solstice (12 January). The magnitude presented is calculated by the expression $100\%([H_2O]_{low} - [H_2O]_{high})/[H_2O]_{low}$, where $[H_2O]_{low}$ and $[H_2O]_{high}$ mean water vapor in year of low and high solar activity respectively. Nowhere does water vapor have a marked diurnal variation resulting from chemistry. However, there is a remarkable variation due to tidal motion in the domain of the strong H_2O gradient in the vicinity of the mesopause so that one should consider defined temporal conditions in order to compare it, e.g. with the NLC occurrence rate. The chemical active species of the odd families are marked by a considerable diurnal variation. Hence, diurnally averaged values are not meaningful. Overall, the calculations (Figure 3.7) show positive values increasing with height as expected. The magnitude of the variation is very different depending on latitude. It is clearly seen from Figure 3.7 that the strongest variations at high latitudes occur in winter. The relative deviation for water vapor is less informative because it can be large but the absolute change is not significant, for example, if the values of the water vapor mixing ratio are very low. On the other hand, for large values of water vapor even small relative changes can produce high absolute ones. Thus, Figure 3.8 depicts the absolute deviation of the water vapor mixing ratio for the same spatio-temporal conditions as displayed in Figure 3.7. As Figure 3.8 shows the largest absolute deviation of water vapor mixing ratio due to the solar cycle occurs at high and middle summer

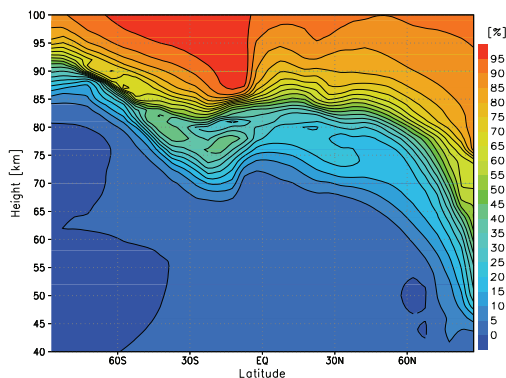


Figure 3.7. Relative deviation of water vapor [%] between years of low and high solar activity for south summer solstice.

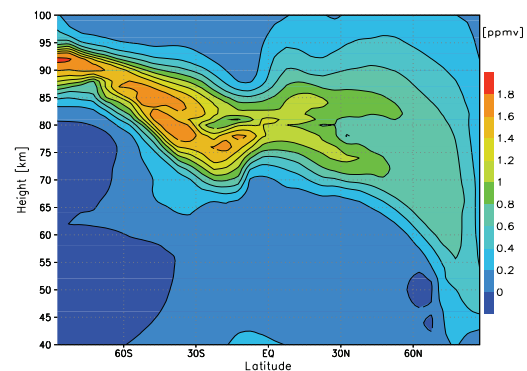


Figure 3.8. Absolute deviation of water vapor mixing ratio [ppmv] between years of low and high solar activity for south summer solstice.

latitudes between 85-95 km that is the region of NLCs and PMSEs formation. One can infer from Figure 3.7 that the deviation decreases from the winter to the summer hemisphere according to the increase of pressure at constant height. The absolute wintertime values vary more weakly (Figure 3.8) than those in summer but the relative variation is much higher.

Figures 3.9 and 3.10 exhibit the same quantity as shown in Figures 3.7 and 3.8, respectively, employing a seasonal section at constant latitude $67.5^\circ N$ - the latitude of the occurrence of NLCs and PMSEs. Figure 3.9 shows the annual variation for the relative deviation of water vapor. The red areas above 85 km in spring and autumn indicate a relative difference of 95%, however, the absolute variations are rather small. These areas correspond to domains

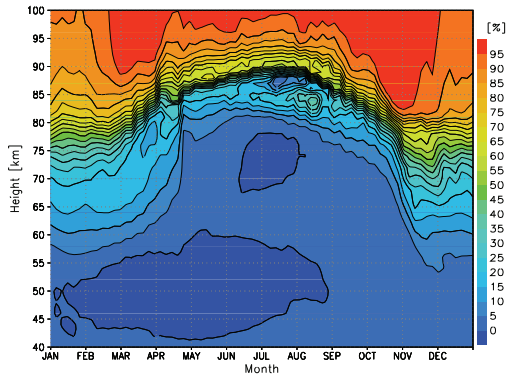


Figure 3.9. Annual variation of relative deviation of water vapor [%] at 67.5° N.

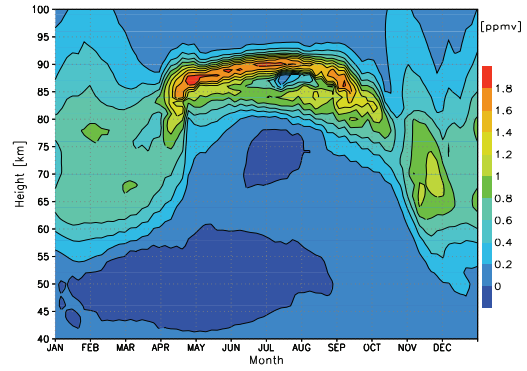


Figure 3.10. Annual variation of absolute deviation of water vapor [ppmv] at 67.5° N.

of dry air moving downwards from the lower thermosphere, which was subjected to the full long term dissociating radiation.

Figure 3.10 illustrates that the 11-year solar cycle has strongest impact on water vapor in the region between 85-95 km during April-August - the region of NLC and PMSE formation. As water vapor is one of the parameters which has an influences on the NLC and PMSE formation and their occurrence rates, this phenomenon can be modulated by 11-year solar activity. The influence of the solar cycle is reduced with decreasing altitude as Figures 3.7 - 3.9 demonstrate.

Figure 3.11 displays the water vapor mixing ratio at 90 km and a latitude of 52.5° N and Figure 3.12 of 67.5° N. The solar activity maximum occurs at year 5.5. One can recognize a clear variation of the water vapor mixing ratio in this height with the smallest values occurring during solar maximum. The annual variation in Figure 3.11 is characterized by a marked semiannual component at this height with maxima in late winter (the smaller one) and late summer (the higher). During years of high solar activity, the annual variation in the absolute amount of the mixing ratio is smallest. A semiannual variation can also be found around the equator. At low latitudes, the annual variation is more complicated, particularly during high solar activity. At high latitudes, as shown in Figure 3.12, the annual variation dominates with a strong peak in summer and only a very small peak in late winter. Both the maxima and minima show nearly a parallel variation over the solar cycle.

In low to mid latitudes the variations with the solar cycle are as expected from theory,

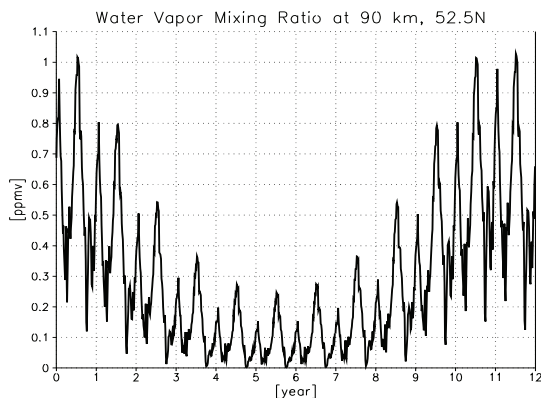


Figure 3.11. Water vapor mixing ratio at 90 km, 52.5° N.

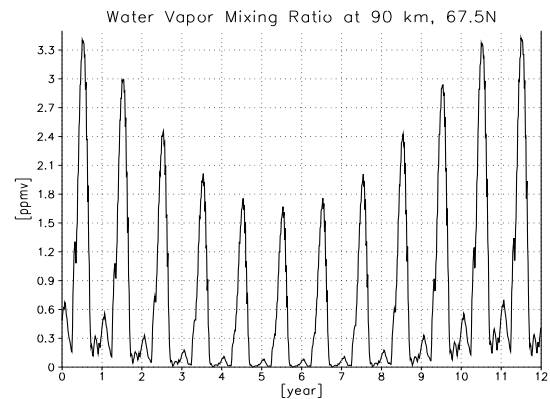


Figure 3.12. Water vapor mixing ratio at 90 km, 67.5° N.

whereas at high latitudes the behavior is somewhat different. Figure 3.13 depicts a 22-year interval of the H₂O mixing ratio at 67.5° N. There is only a relatively weak solar cycle variation (about 20% for the peak values during the NLC season).

At low latitudes, the connection to the solar activity is closer and strongest around the equator, as Figure 3.14 illustrates. This finding is not so surprising as the radiation penetrates deeper into the atmosphere there. Additionally, the air pressure at high latitudes is greater in summer than at other latitudes during this time, meaning an effective absorption of Lyman-alpha radiation begins already at greater heights.

Chandra et al. [1997] analysed HALOE data of water vapor for the 11-years solar cycle. They found a variation of about 30-40 % at 80 km and only 1-2 % at 60-65 km. At 45° N at 80

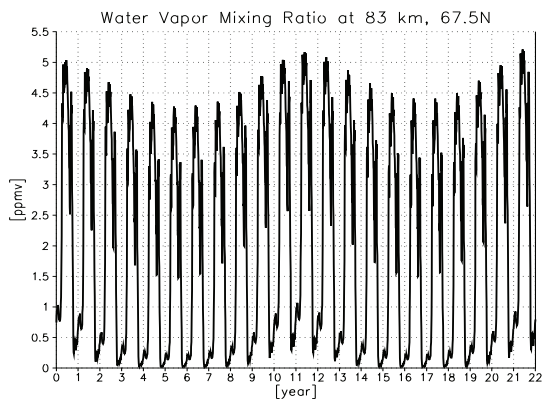


Figure 3.13. Water vapor mixing ratio at 83 km, 67.5° N.

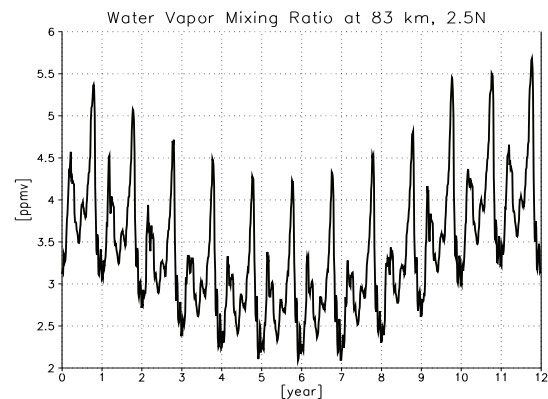


Figure 3.14. Water vapor mixing ratio at 83 km, 2.5° N.

km they inferred an annual averaged mixing ratio growth from 2.41 to 3.22 ppmv for the years from 1992 to 1995. Figure 3.15 shows this quantity for two solar cycles for the same height and a neighboring latitude (47.5° N). The model results show growth from approximately 2.4 to 3.3 ppmv in excellent agreement with the HALOE data. The data presented in Figures 3.7 and 3.9 also yields only very small variations below 65 km in the order of the HALOE measurements.

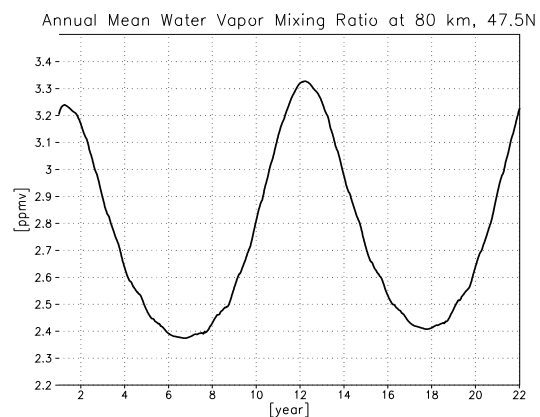


Figure 3.15. Solar cycle variation of the annual mean of water vapor mixing ratio [ppmv] at 47.5° N at 80 km.

The Lyman-alpha radiation in the upper mesosphere - mesopause region has direct impact mainly on water vapor but due to the hydrogen radical production it also influences indirectly other chemically active minor species. In order to prove the existence of such an influence few examples are presented here. Figures 3.16 - 3.18 depict the solar cycle variation of ozone, atomic hydrogen and hydroxyl, respectively at 83 km at 2.5° N. For ozone one can recognize clear semiannual variation with maxima in winter and a lower one in summer. The amplitudes are modulated by the solar cycle with maximum values during solar minimum. Atomic hydrogen and hydroxyl vary in the opposite way (Figures 3.17 and 3.18) and correlate with Lyman-alpha radiation. During solar minimum the annual variation

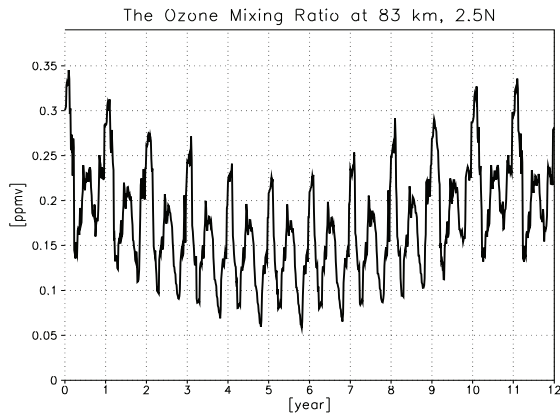


Figure 3.16. Ozone mixing ratio at 83 km, 2.5° N.

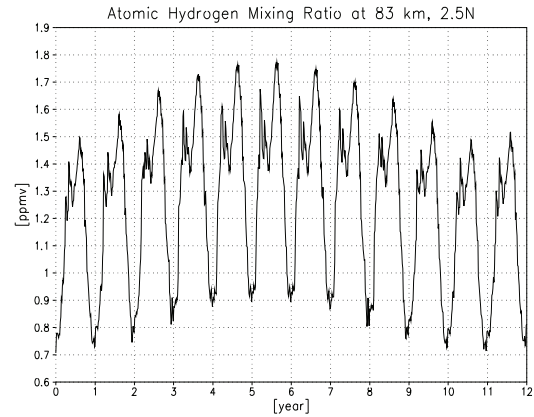


Figure 3.17. Atomic hydrogen mixing ratio at 83 km, 2.5° N.

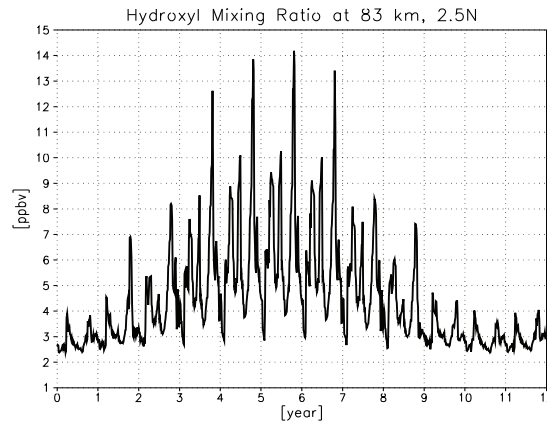


Figure 3.18. Hydroxyl mixing ratio at 83 km, 2.5° N.

is strongly reduced. There are semiannual variations opposing that of ozone, but their amplitudes are essentially noisy. The variation during the solar cycle results from the variation of the dissociation rates of water vapor, whereas, the semiannual variation is mainly determined by the dynamics. Comparing Figure 3.16 with 3.14 one can infer a somewhat unexpected results that water vapor and ozone anticorrelate during the annual cycle, but they correlate during the 11-year cycle. To explain this behavior let carry out two mental experiments. First, imagining an air parcel is subjected to photolysis which depends on time, and thereby its state varies in time. Assume also, that the fluxes of water vapor through the boundaries are small (smaller than changes due to photolysis) and constant. In this case the logical chain is: amount of water vapor decreases due to photolysis - the number density of hydrogen radicals grows - the number density of ozone decreases due to chemical reactions with hydrogen radicals, thus, changes of water vapor and ozone will be correlated. The second experiment is the same, but now there is a flux of water vapor through the boundaries of the box varying in time, but the photolysis is constant, in other words, the water vapor in the box is determined by the flux. In the second case the logical deduction has the order: water vapor is changed by flux - production of odd hydrogens will be changed in same direction as water vapor - changes of ozone will have the opposite direction with water vapor, thus, changes of ozone and water vapor will be anticorrelated. First mental experiment is equivalent to the 11-year variation in the model, because a certain day in

the model has the same dynamics for all years and the variation of water vapor is determined by variation of Lyman-alpha radiation. The second one is equivalent to the annual cycle as during the annual cycle the variation of water vapor is mainly determined by advection and changes of the photolysis from day to day is less significant. Now, one can come to a more general rule of relative behavior of ozone and water vapor in the upper mesosphere-mesopause-lower termosphere. If during a certain period the variation of the photolysis rate of water vapor is not significant and the variation of water vapor is mainly modulated by advection the changes of water vapor and ozone will be anticorrelated. If during a certain period the fluxes of water vapor are constant and changes of water vapor are determined by changes of the photolysis ozone and water vapor will be correlated.

Looking on the problem from the other side, one can use an analytical formula for ozone at 80 km [Allen et al., 1984]:

$$[O_3]_{80} \approx \frac{(J_1 + J_2)^2 k_{20} k_2 [O_2]^2}{J_5 [H_2O] k_{15} k_{10} \left(J_3 + J_4 + \frac{k_{11} (J_1 + J_2)}{k_{10} [M]} \right)}, \quad (3.1)$$

where the kinetic rate constants k_i refer to reactions in Appendix F, J_1, J_2 - dissociation rates of molecular oxygen, J_3, J_4 - dissociation rates of ozone and J_5 - dissociation rate of water vapor. Carefully looking on the denominator one can see that ozone is inversely proportional to H_2O and to the dissociation rate of water vapor J_5 . If water vapor varies under the conditions of constant or small variation of photolysis rate, then the variation of ozone will be determined by water vapor. Consequently ozone and water vapor are anticorrelated, that is the case of annual variation. If the variation of water vapor is small but its dissociation rate varies more significantly, then the variation of ozone will be determined by variation of the photolysis rate of water vapor J_5 , and ozone will be anticorrelated with the photolysis rate, meaning it correlates with water vapor, that is the case of the 11-year cycle at the mesopause near the equator. Thus, water vapor and ozone are able to show both correlation and anticorrelation behavior during 11-year and 27-day cycles, which are determined by Lyman-alpha radiation.

The influence of the solar activity on the mesospheric dynamics is still an open question and not easy to answer since, due to comparable characteristic response times, the dynamics and chemistry are closely connected in the mesosphere. The solar cycle variation of the vertical wind would influence the water vapor distribution also imprinting its variation into the NLC occurrence rate.

3.3 Autocatalytic Water Vapor Production

One of poorly understood phenomena is the occurrence of very large water vapor concentrations within the upper mesosphere - a domain where H_2O is effectively destroyed by photolysis. As early as 1977, an indication of a relatively high-lying maximum of the WVMR close to 60 km was reported [Radford et al., 1977]. In 1982 a water vapor layer was also detected at 65 km [Gibbins et al., 1982]. However, both groups used the microwave technique and derived wrong absolute values [Radford et al., 1977; Gibbins et al., 1982]. Using microwave measurements, a tendency for increasing WVMRs in the 60 to 65 km domain up to 6 ppmv was found for certain seasonal conditions [Bevilacqua et al., 1985]. In 1996, Neduluha et al. published a profile of WVMR retrieved from microwave measurements at Table Mountain (34.4° N) during a period in July that clearly showed a double peak structure for altitude. The upper

maximum lay around 65 km and the conventional one around 46 km. The values of the WVMRs ranged between 6.5 and 7 ppmv, with the upper one being a little stronger. A high maximum was also sporadically observed at the ALOMAR observatory (Figure 3.1), Norway (69° N; 16° E), in the midsummer [Seele and Hartogh, 1999]. Other groups found only peaks around the stratopause [Peter et al., 1988]. An unusually high peak of the WVMR was investigated in a sequence of articles [Summers et al., 1996, Harries et al., 1996a, 1996b; Summers et al., 1997a, 1997b; Siskind and Summers, 1998; Summers and Siskind, 1997, 1999; Summers et al., 2001]. Some articles mentioned above reported about measurements of unexplained high H₂O layer near an altitude of 65 to 70 km. The effect is not a permanent phenomenon, but it occurs during certain seasons at different latitudes. The occurrence of the very high WVMR layer in the HALOE data outside of the noctilucent cloud area with mixing ratios up to 7 ppmv and close to 70 km was speculatively interpreted by a heterogeneous reaction of H₂ with O on the surface of meteoric dust [Summers and Siskind, 1999]. In this context, a disagreement of the measurements for standard chemistry was often stated [Clancy et al., 1994; Summers et al., 1997a; Sandor and Clancy, 1998; Conway et al., 2000; Summers et al., 2001]. Different measurements have shown that large water vapor mixing ratios occur in the upper mesosphere in high latitude summer under conditions of strongest solar insolation where photolysis should effectively reduce its value and strong upward vertical wind exists. Obviously, the observations are in contradiction with the simple notion of a monotonic decrease of the WVMR with height above its maximum near the stratopause due to increasing photolysis of water vapor. The analysis of this finding by means of a high-resolution 1D-model supplies evidence that water vapor is autocatalytically formed below a height of about 65 km and destroyed by photolysis above this altitude. We call this level cross-over altitude (CA). As it was shown in section 3.1, calculations by means of our 3D-model COMMA-IAP yield seasonal-latitudinal patterns and variations well comparable with those of the HALOE or microwave observations at ALOMAR. The model output mirrors typical patterns of high water vapor mixing ratios at high latitudes during the summer as measured by HALOE or by microwave technique at ALOMAR. Thus, based on experiments with our 3D-model COMMA-IAP, three catalytic cycles of water vapor formation from the molecular hydrogen reservoir were proposed [Sonnemann et al., 2005] (see Appendix E). Two necessary conditions should be satisfied for the autocatalytic water vapor formation - a vertical wind accelerated with height and prolonged time of solar insolation, both exist during summer at high latitudes. Hydrogen radicals act as catalysts, resulting mainly from water vapor by photolysis and oxidation by O(¹D). A great number of the hydrogen radicals return to water vapor by so-called zero cycles, particularly under the condition of small atomic hydrogen concentration decreasing strongly with decreasing height. In the upper domain under the condition of large atomic hydrogen concentrations, the formation of molecular hydrogen will be favored. Favorable conditions for large water vapor mixing ratios at high altitudes are given by an accelerated upward vertical wind. Below the cross-over altitude the vertical wind is weak so that H₂ and CH₄ have sufficient time to be oxidized into H₂O - a very slow process. Above this level, however, the vertical wind has to be strong in order to lift the H₂O enriched air to greater heights before the dissociation has an effective impact on the H₂O-distribution. Such accelerated upward vertical winds are typical for the mesosphere under certain seasonal-latitudinal conditions: high and mean latitudes during summer.

The oxidation of methane by the hydroxyl radical OH and the excited atomic oxygen atom O(¹D) in the stratosphere leads to an increase of the water vapor mixing ratio (WVMR) with maximum global mean values in the upper stratosphere/lower mesosphere (the conventional WVMR maximum being around 50 km). According to this process, the mean global methane

mixing ratio decreases from about 1.7 ppmv in the lower atmosphere [Khalil et al., 1993] to about 100 ppbv at 60 km and 10 ppbv at 70 km [Körner and Sonnemann, 2001]. On global average a downward and upward transport of H₂O takes place from the peak of the WVMR so that the effective carrier of hydrogen atoms contributing to the escape flux into space is methane [Sonnemann and Körner, 2003]. Due to turbulent mixing within the homosphere (up to about 100 km), the total hydrogen mixing ratio is nearly a conserved quantity up to about 70 km [Sonnemann and Körner, 2003]. The total hydrogen mixing ratio ranges from 7.5 to 8 ppmv in H₂ equivalents. Above the cross-over altitude water vapor is subject to increasing photolysis so that it is converted into molecular and finally into atomic hydrogen.

In the upper mesosphere, H₂O is dissociated into H and OH (the branch into H₂ and O plays no role at that height). Hence, at first glance H₂O should decrease because of solar illumination. This process results in the formation of two hydrogen radicals from one water vapor molecule. The same assertion is valid for the oxidation of H₂O by O(¹D) according to H₂O+O(¹D) → 2OH. The reaction of H₂ with O(¹D) also leads to the production of two hydrogen radicals, and the decomposition of methane likewise results in the formation of H radicals depending on special conditions (see also the graph of methane decomposition in Sonnemann et al. [1998]). The radical formation represents the first step in the catalytic water vapor production. As the O(¹D) formation also results from the photolysis of ozone, the hydrogen radical production is strongest under the condition of strongest solar photodissociation. Great portions of the radicals return to water vapor, particularly under the condition of sufficiently large air density, which entails a small atomic hydrogen concentration. There are a large number of different zero-cycles returning two hydrogen radicals back to water vapor (see Appendix E). The net effect in all cases is that the solar shortwave radiation is dissipated into heat. These are the dominant processes in the middle mesosphere. The effective chemical lifetime of water vapor becomes very large and reach 10⁷ -10⁹ s above 65 km at high and mean latitudes during the summer [Körner and Sonnemann, 2001] as Figures 3.19 and 3.20 show.

Hydrogen radicals act as catalysts. As the catalysts that form H₂O stem for a large part from H₂O itself, the process are called autocatalytical. The hydrogen radicals return to H₂O or form H₂ after being some times involved in one of the catalytic cycles. The formation of H₂ requires, according to the reaction H+HO₂ → H₂+O₂, atomic hydrogen as a reactant. This is the only (conventional) reaction producing H₂ from the hydrogen radicals. However, there is a permanent source for H₂ from the decomposition of methane, which compensates partly for the

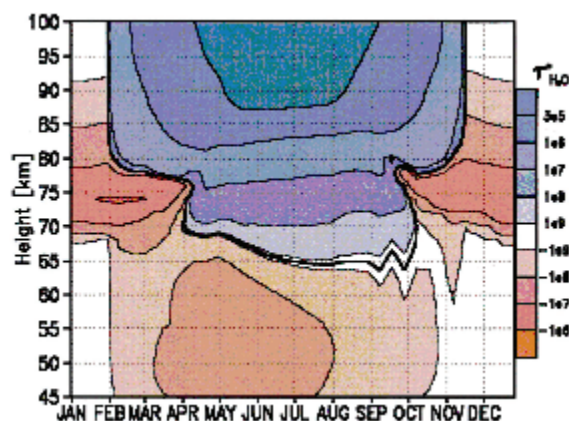


Figure 3.19. Seasonal section of the effective characteristic chemical time [s] for water vapor at 72.5° N. Körner and Sonnemann [2001].

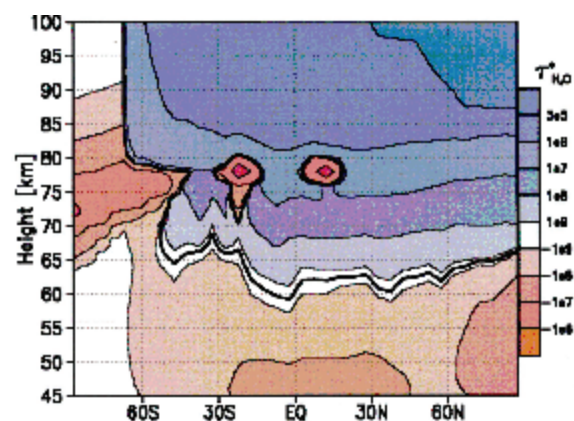


Figure 3.20. Latitudinal section of the effective characteristic chemical time [s] for water vapor for northern summer solstice. Körner and Sonnemann [2001].

loss of H₂. Due to the loss reactions H+O₂+M → HO₂+M and H+O₃+M → OH+O₂, atomic hydrogen decreases strongly with decreasing height. The first reaction depends quadratically on the air density. Ozone also increases greater than the air density with decreasing altitude. Hence, H₂ formation becomes less effective at lower altitudes. Each hydrogen radical resulting from H₂O runs on average n times through one of the catalytic cycles before it is transformed, together with a second radical, into an H₂ molecule. In that case that number n is just a half, meaning two hydrogen radicals resulting from H₂O have, on average, exactly one H₂ molecule oxidized to H₂O before they react to form H₂, then the composition does not change. The height where this is valid is the cross-over altitude. The existence of a CA requires that the atmosphere is not yet in photochemical equilibrium. This corresponds to the real state of the atmosphere.

In contrast to the heights above 65-70 km, the hydrogen radical formation due to oxidation by O(¹D) becomes increasingly important in the middle and lower mesosphere. O(¹D) results from the photodissociation of ozone in the Hartley bands. There is a broad maximum of its concentration near the stratopause. The radical formation takes place by the process O(¹D)+H₂O → 2OH. A hydroxyl radical then reacts according to the reaction schemes given above. The fast reaction OH+O → H+O₂, forming atomic hydrogen, is very important as this reaction determines almost exclusively the production term of H in that domain. In contrast to the H-loss terms, this term still increases with decreasing height in the mesosphere/stratopause region; however, it does not compensate the increasing loss of H and so the H-concentration strongly decreases with decreasing height.

Since the H₂-concentration is crucial in determining the feasibility of the catalytic water vapor formation, the only effective H₂ formation process mentioned is the reaction of H with HO₂. Equilibrium of H₂ is approximately given if the diurnally averaged production is equal to its diurnally averaged loss. Including the main loss processes for H₂ by reaction with OH and O(¹D), the H₂-concentration should approximately approach

$$[H_2] = \frac{l_1[H][HO_2]}{(l_2[O(^1D)] + l_3[OH])} \quad (3.2)$$

if transport is neglected. Here the squared brackets stand for the density of the constituent within the brackets. The quantities l_i are the kinetic reaction rates $l_1 = 5.6 \cdot 10^{-12}$, $l_2 = 1.1 \cdot 10^{-10}$, $l_3 = 5.5 \cdot 10^{-12} \exp(-2000/T) \text{ cm}^3 \text{ s}^{-1}$ [Atkinson et al., 1992; Sander et al., 2003]. The concentrations represent their mean daytime values. The idealized steady state of Equation (3.2) is only valid approximately in the lower to middle mesosphere after a long time of calculation after the transient period. Especially in the upper mesosphere/mesopause region, the concentrations of the individual constituents vary strongly during the time of day and their variations are not in phase with one another. It is evident from this expression, due to the quadratic dependence of the main atomic hydrogen loss process on air density, and the reaction with ozone, that the equilibrium concentration of molecular hydrogen decreases drastically with decreasing height. H₂ is transformed into water vapor as long as its concentration is greater than its equilibrium concentration.

Autocatalytic water vapor production discussed below based on examples of model calculations for the southern hemisphere. One of such examples was shown in section 3.1 (see Figure 3.4). One can see on it, as it was discussed, a clear double maximum structure with high values 6.6-6.9 ppmv at high summer latitudes (60° S - 90° S) at altitudes 65-78 km . Figure 3.21 shows the calculated annual variation of the water vapor mixing ratio at 67.5°. Largest water

vapor mixing ratios at 65 -75 km occur after the south summer solstice (22 December). A clear double maximum appears in this period. The principal annual patterns with a time shift of half a year are comparable to the annual variation as measured by Seele and Hartogh [1999] at 69° N (Figure 3.1) and calculated by COMMA-IAP for 67.5° N (Figure 3.2). One can see on Figure 3.21 strong water vapor decrease in May. This figure makes clear the fact that the water vapor distribution can vary significantly within a time range of 4 weeks. Figures 3.22 - 3.23 display the molecular hydrogen mixing ratio in latitudinal section for 10 January (the date after south summer solstice) and its annual variation at 67.5° S, respectively. These figures correspond to Figure 3.4 and Figure 3.21 and show an inverse behavior of molecular hydrogen and water vapor mixing ratio as total amount of even hydrogens ($2\text{CH}_4 + \text{H}_2\text{O} + \text{H}_2$) is a conservative quantity

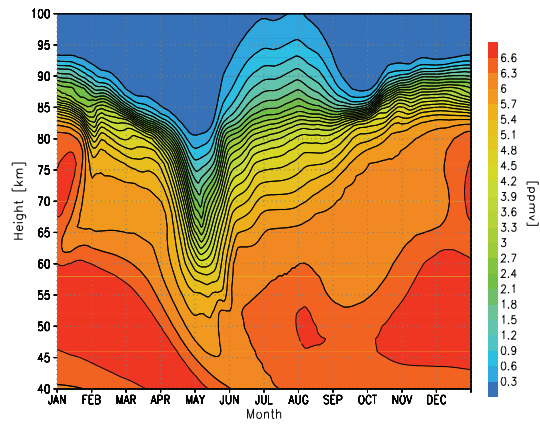


Figure 3.21. Annual variation of water vapor mixing ratio at 67.5° S.

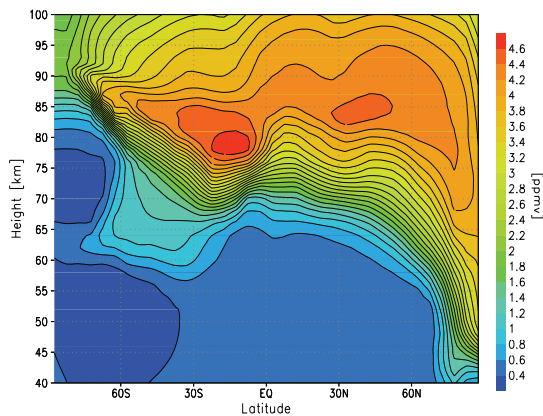


Figure 3.22. Latitudinal section of molecular hydrogen mixing ratio for 10 January (southern summer).

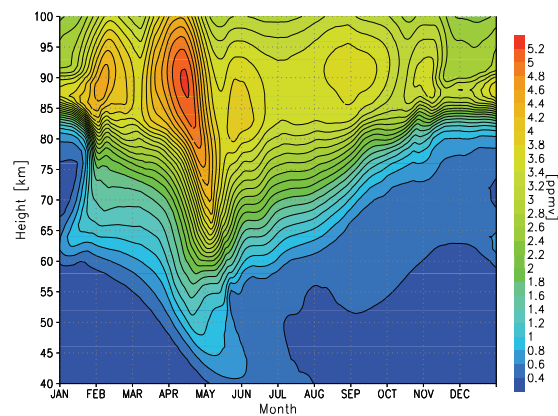


Figure 3.23. Annual variation of molecular hydrogen mixing ratio at 67.5° S.

below 70 km as it was discussed by Körner and Sonnemann [2001]. Domains of large water vapor mixing ratio are related to small values of the molecular hydrogen mixing ratio. The patterns are connected with vertical wind patterns because downward directed winds transport air enriched with molecular hydrogen into lower altitudes and vice versa. Figure 3.24 depicts the seasonal section of the zonally averaged vertical wind at 67.5° S according to the output of dynamic part of model COMMA-IAP. As mentioned above, an upward directed vertical wind accelerated with altitude above the stratopause - one of the requirements for formation of high water vapor mixing ratio in the summer mesosphere and for the double maximum structure of it. One can recognize the acceleration

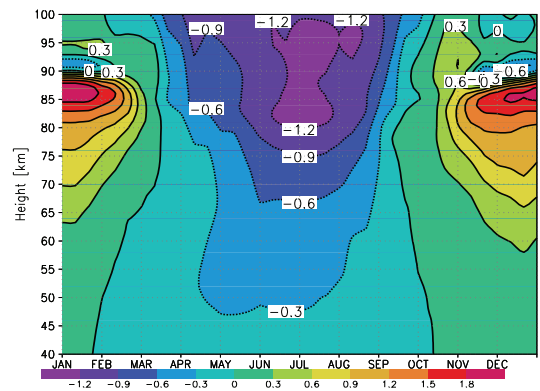


Figure 3.24. Seasonal section of the zonally averaged vertical wind [cm/s] at 67.5° S.

of the vertical wind with increasing height above 65 km during southern summer months (November - February).

The 3D-calculations clearly showed that the H₂-distribution is essentially controlled by the vertical wind system. Downward directed wind conveys dry but H₂-abundant air from the mesopause region down to the mean and lower mesosphere. In contrast, relatively humid air marked by small H₂ mixing ratios will be transported by upward moving air into the upper mesosphere/mesopause region. On this path below 65 km, H₂ is subjected to catalytic oxidation to H₂O. However, this is normally a very slow process and will be discussed later. Around the stratopause region, the vertical winds possess, on average, the smallest amounts anywhere in the atmosphere. The air is relatively isolated there for a long time; the vertical exchange of air is considerably reduced. Hence, the oxidation of H₂O and CH₄ to H₂O can optimally take place. The characteristic lifetime of H₂ averaged over a day according to Equation 3.2 amounts to:

$$\tau(H_2) = \left(\overline{l_2 [O(^1D)]} + l_3 [OH] \right)^{-1}, \quad (3.3)$$

where l_2 , l_3 refer to reaction rates at Equation 3.2, and upper line means averaging during a day.

Using typical values for the concentrations of O(¹D) and OH at the stratopause, the reaction rates for, e.g. T = 270 K, and considering equinox conditions with half a day night, the characteristic time amounts to roughly $2 \cdot 10^7$ s or 231 days. This value is essentially smaller at high latitudes when approaching summer solstice due to the prolongation of the daytime, the increase of temperature and the rise of the concentration of O(¹D) and OH. Both constituents have approximately the same influence on molecular hydrogen at that domain. Especially in the stratosphere as mentioned above, the H₂ loss will (partly) be compensated by the decomposition of CH₄, also resulting in H₂ for a certain branch of decomposition. The WVMR increases with altitude and has a pronounced maximum, on global average, slightly above the stratopause [Sonnemann and Kömer, 2003]. This value is the so-called conventional maximum.

Although H₂ is oxidized to H₂O up to the cross-over altitude (65 km), a question arises. Why does the water vapor mixing ratio not continue increase up to this height on global average? The answer is related to the increasingly stronger mixing with height above the stratopause region due to the comparably long lifetime of H₂. This can be inferred from Figure 3.24 displaying the accelerated vertical wind at high latitude (67.5° S) and Figure 3.23 demonstrating the mixing of H₂ within the mesosphere. The lifetime of H₂ increases in the mesosphere with increasing height due to the decline of the concentrations both of O(¹D) (up to 80 km) and OH, and due to the decrease of the temperature (l_3 depends very strongly on T). Normally, the mixing takes place faster than the catalytic oxidation of H₂. Only under preferred conditions do the catalytic processes result in an obvious increase of the water vapor mixing ratio with height, sometimes the interplay between dynamics and chemistry produces a double peak. The second maximum occurs between 65 and 75 km. The preferred conditions exist most often at high latitudes in summer. The equator maximum during spring equinox (Figures 3.3 and 3.5) is not discussed here in detail. However, Siskind and Summers [1998] derived from HALOE observations that the 70 km enhancement of water vapor around the equator appears to be shifted in latitude such that it follows the sun, but with a 30-60 day lag.

At high latitudes in winter (May - August on Figure 3.23), the mesosphere is enriched with H₂ that was downward transported from the mesopause region. After the vertical wind reversal (September on Figure 3.24), this air is transported upwards again and subjected to the amplified catalytic oxidation. Hence, the water vapor mixing ratio increases (after November on

Figure 3.21), and the levels of constant mixing ratios are shifted upward. As shown before, this process has a seasonal timescale. After solstice, peaking in midsummer, the WVMR reaches its largest values with a time delay of about a month (end of December - end of January on Figure 3.21). During this phase, the secondary peak occurs at an altitude between 70 and 75 km. In the calculations, this maximum was obtained by using homogeneous chemistry and did not need to introduce a heterogeneous reaction as done by Summers and Siskind [1999].

The cross-over altitude (65 km) was calculated by means of the 1D-model under highly idealized conditions. As Equation 3.2 makes clear, the H_2 equilibrium depends on the ratio of the production term to the loss term, and is determined essentially by the composition of the hydrogen radicals. Figure 3.25 shows the distribution of the H_2 equilibrium-mixing ratio in an altitude-latitude section for December 1st, calculated according to Equation 3.2 by means of the 3D-model displaying diurnally averaged values. The area for mixing ratios greater than 6 ppmv is left blank. Figure 3.25 clearly exhibits the decrease of the H_2 equilibrium-mixing ratio with increasing latitude in summer. At the south pole, the 0.8 ppmv level touches 70 km but it is about 2.5 km lower at 60° S. The same assertion is valid for the winter hemisphere, but this is unimportant as the behavior during this time is governed by transports due to the strong rise of the characteristic lifetime of H_2 . This means that the H_2 chemistry becomes minor and, in fact, it can be neglected. Thus, the downward transport of this constituent determines the mixing ratio.

As shown by figure 3.24 the vertical wind accelerates with height up to the mesopause region. The same is true for the meridional wind conveying permanently, on global average, air out of the polar region. The wind is strongest at the upper mesosphere. Figure 3.26 displays the

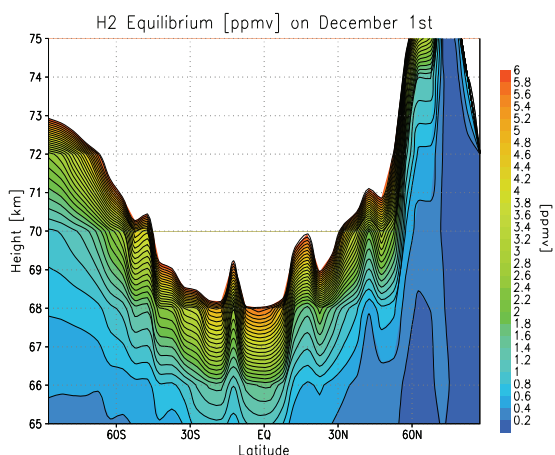


Figure 3.25. Molecular hydrogen equilibrium mixing ratio [ppmv] for 1 December (before summer solstice in southern hemisphere).

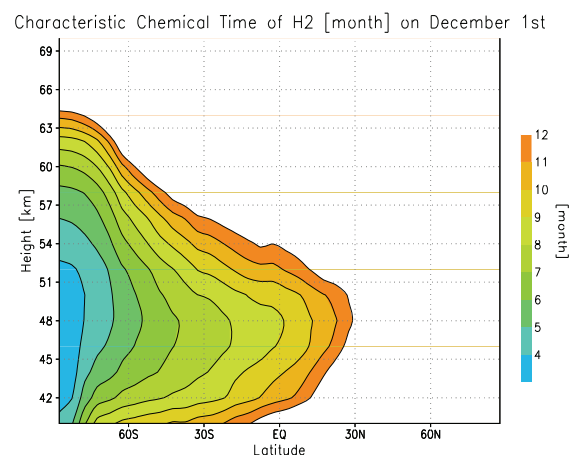


Figure 3.26. The characteristic chemical lifetime of H_2 for 1 December (before summer solstice in southern hemisphere).

same conditions as shown in Figure 3.25 but for the characteristic lifetime of H_2 . The characteristic times larger than 1 year are not displayed. The figure makes it clear that only under conditions of highest solar insolation peaking around the stratopause (blue color) does the characteristic time possess a seasonal scale. Otherwise, H_2 has a characteristic chemical lifetime larger than the characteristic transport time and thus its distribution is mainly determined by advection.

According to the general formula given by Körner and Sonnemann [2001], Figure 3.27 shows, for the same state of affairs as depicted in Figure 3.26, the effective characteristic time considering not only the loss, but also the production of H_2 . The effective characteristic time for

molecular hydrogen has been calculated by the expression:

$$\tau_{\text{eff}}(H_2) = \left(l_2 [O(^1D)] + l_3 [OH] - l_1 [H] [HO_2] / [H_2] \right)^{-1}, \quad (3.4)$$

where l_1, l_2, l_3 refer to reaction rates at Equation 3.2, and the upper line means averaging over a day.

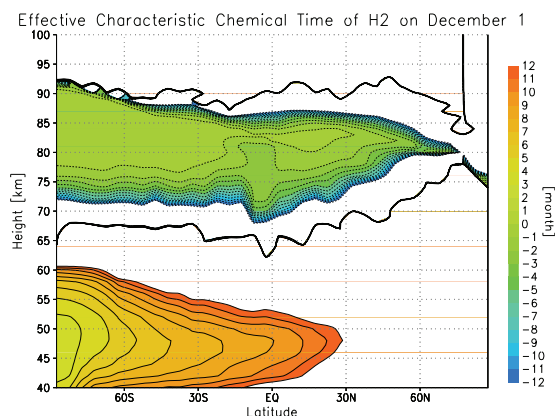


Figure 3.27. Effective characteristic chemical lifetime of molecular hydrogen for 1 December (before southern summer solstice).

of changing the sign of the characteristic time at high summer latitudes. The result of this is that an almost constant WVMR is transported upward until the H_2 formation, and accordingly the H_2O loss, becomes stronger above about 75 km (>3 months). The absolute amount of the effective characteristic time of H_2 formation drops below 1 month between 80 and 90 km. However, the H_2O loss is even stronger than this value, indicating that it is partly converted into atomic hydrogen and becomes a major hydrogen-carrying constituent there [Körner and Sonnemann, 2001]. Figure 3.27 makes clear that globally H_2 is mainly controlled by dynamic processes. The exception is the region at high latitudes of the summer hemisphere confined below 60 km. Globally, in a broad band with exception of the high latitude winter between 75 and 85-90 km, H_2 will be formed more effectively, but also there is the characteristic transport time smaller than that of the chemical formation.

The effective characteristic time can change its sign (becoming negative) if the production is stronger than the loss. This occurs approximately at 65 km at the summer pole but increases then up to 67 km. Above that height no water vapor will be formed. There is a second range at high altitudes corresponding to the secondary ozone maximum. There, the loss is stronger than the production. However, it is marked by very long effective characteristic times and the loss does not result in a net water vapor formation but only in H production. Due to very long characteristic times, the H_2 formation from water vapor is also very slow above the boundary

of changing the sign of the characteristic time at high summer latitudes. The result of this is that an almost constant WVMR is transported upward until the H_2 formation, and accordingly the H_2O loss, becomes stronger above about 75 km (>3 months). The absolute amount of the effective characteristic time of H_2 formation drops below 1 month between 80 and 90 km. However, the H_2O loss is even stronger than this value, indicating that it is partly converted into atomic hydrogen and becomes a major hydrogen-carrying constituent there [Körner and Sonnemann, 2001]. Figure 3.27 makes clear that globally H_2 is mainly controlled by dynamic processes. The exception is the region at high latitudes of the summer hemisphere confined below 60 km. Globally, in a broad band with exception of the high latitude winter between 75 and 85-90 km, H_2 will be formed more effectively, but also there is the characteristic transport time smaller than that of the chemical formation.

Until summer solstice, the WVMR decreases slightly with height above 60-65 km. After that time a small minimum occurs between 60 and 65 km, which cannot be explained by chemistry alone. The zonally averaged meridional wind blows out of the polar area, but this is not true for the local wind that is strongly subjected to the tides. During certain phases of the day, the wind blows onto the pole, transporting dryer air from lower latitudes into higher latitudes. Thus, tidal motion, in addition to diffusion, is connected with weak air mixing marked by the tendency to dissipate (latitudinal) gradients of the mixing ratios. Around 60 to 65 km, the diurnal tide prevails whereas above 70 km the semi-diurnal tide begins to dominate. Figures 3.28 and 3.29 depict the meridional wind in a clockwise south polar projection at 60 and 70 km altitude, respectively, for December 1st. The diurnal tide preferred long-range transports as the wind blows for a longer time in the same direction. The mean meridional wind strengthened with height, and the increasing dominance of the semi-diurnal tide weakens the mixing tendency whereas with decreasing altitude the mixing tendency increases. Due to the slight latitudinal gradient of the WVMR and the essentially smaller wind components near its global middle

Meridional Wind at 60 km, Lat.[42.5S;87.5S], Dec.1

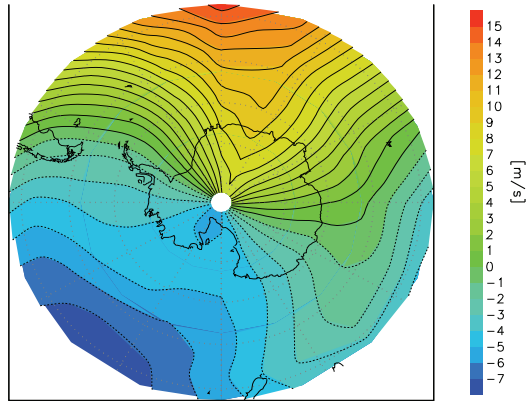


Figure 3.28. Meridional wind [m/s] in south polar projection at 60 km for 1 December (before southern summer solstice).

Meridional Wind at 70 km, Lat.[42.5S;87.5S], Dec.1

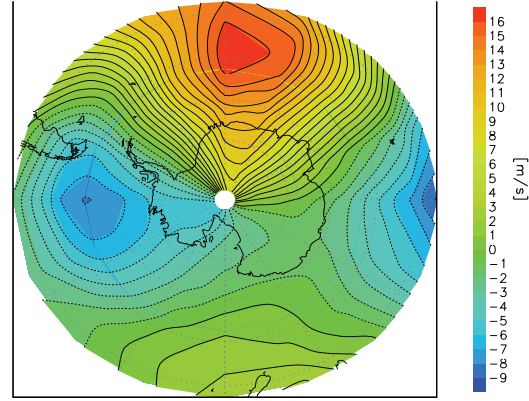


Figure 3.29. Meridional wind [m/s] in south polar projection at 60 km for 1 December (before southern summer solstice).

atmospheric maximum around the stratopause, the WVMR is not essentially affected there. The strongest influence exists in the 60 to 65 km range at high latitudes where dryer air from relatively lower latitudes will be mixed with humid air, thereby forming a slight minimum of the WVMR after solstice (see Figures 3.4 and 3.21). That is why the upper maximum of the WVMR does not indicate a local production of water vapor at that height, but instead indicates that due to dynamic processes a minimum is formed below it. Only by consideration of the tidal motion, calculated in the frame of a non-diffusive 3D-model, the reproduction of a double peak of the WVMR is possible.

3.4 Summary and Conclusions

The behavior of water vapor in the middle atmosphere was modeled based on the 3D-model COMMA-IAP. Comparisons of the results of modeling with the results of measurements, particularly with HALOE and microwave measurements at ALOMAR, show good agreement. Both measurements and modeling show annual variations of water vapor with higher values in the mesosphere-mesopause-lower thermosphere (MLT) region during summer. The double-maximum structure of water vapor with maxima of 6.5-7 ppmv at 45-55 and 70-75 km was observed by measurements and reproduced by the model in the summer mesosphere at high latitudes. Explanation of this feature was done in frame of gas-phase chemistry by autocatalytic water vapor formation under conditions of prolonged time of solar insolation and vertical wind accelerated with height. In order to understand the formation of this double maximum one has to take into consideration the complicated interplay between chemistry and dynamics. One can see that only under conditions of prolonged daytime hours of solar insolation in summer (especially within the polar day area) the hydrogen-bearing constituents will be converted into H_2O below about 65 km. Above that height, H_2 is formed from H_2O , but the effective characteristic time scale of H_2O is long compared with the transport time up to 75-80 km so that the vertical transport lifts humid air upward without large loss of it. The zonally averaged meridional wind blows out of the pole area in summer, but this is not generally true for the meridional wind depending on local time. Owing to the tidal waves there are ranges transporting relatively dry air from outside into the polar region that lower the mean water vapor mixing ratio. This effect is strongest at 60 to 65 km dominated by the diurnal tide. Above this height, the

semi-diurnal tide begins to dominate and the averaged outward blowing wind becomes stronger. Below 60 km, the horizontal water vapor gradient is essentially smaller and the winds are much less than above so that an air mixing does not play such a great role there. Outside of the high latitudes, water vapor mixing ratio maximum has been observed at this height close to the equator and particularly around equinox. These events are not discussed in detail here but the explanation is generally the same - an interplay of chemistry and transport under the condition of strongest solar insolation. In order to get the largest water vapor concentrations at altitudes of 70-80 km, the vertical wind should be small below the cross-over altitude but large above this crossover level. This requires accelerated winds with increasing height such as also result from calculations by means of the global 3D-model COMMA-IAP. Owing to the uncertainties of some rate constants, the model outputs could change in some details, however, the good agreement between the results of COMMA-IAP calculations, HALOE measurements and microwave observations at ALOMAR significantly supports the credibility of the results. In order to understand the behavior of the mesospheric water vapor it would be useful to clarify the discrepancy between the HALOE and other observations, particularly in the upper mesosphere.

Additionally, the influence of the 11-year solar cycle on water vapor and other minor constituents as ozone, atomic hydrogen and hydroxyl was investigated on the basis of COMMA-IAP in the MLT region. The Lyman-alpha radiation has strongest impact mainly on water vapor above 70 km. Water vapor always shows an anticorrelation with Lyman-alpha radiation, whereas ozone can correlate or anticorrelate in frame of 11-year solar cycle depending on amplitude of water vapor. Special attention was given to the chemical composition of the NLC region at high latitudes during summer. The largest absolute deviation of water vapor due to 11-year solar cycle was found at high latitudes between 85-95 km during April-August. Thus, as water vapor is one of the parameters for the NLC and PMSE formation, these phenomena can be modulated by the 11-year solar cycle. There was not found an indication of a phase delay of approximately two-three years between solar activity and water vapor response in that height as the NLC occurrence rate shows [Gadsden, 1998; Thomas and Olivero, 2001]. Assuming it is true, this phase lag seems to be rather a temperature effect than a direct influence of H₂O. A candidate of the cause of the phase delay could be given by the geomagnetic activity reaching its maximum two years after the solar maximum, but it is also conceivable that it is a feedback of some species to the dynamics. The temperature is the most sensitive parameter with respect to the NLC formation. It is influenced by the change of the composition with varying solar activity (ozone, atomic oxygen, CO₂, chemical heating rates). Thus, the analysis of calculations based on an interactively coupled model with feedback of the calculated chemical constituents to the dynamical part of the model would be very significant.

Chapter 4

Trend Calculations

4.1 General Problem

Trend is the tendency of the change of a parameter within a sufficient long time range eliminating all accidental (natural) and quasi-cyclic variations. The dominant cyclic variations are not only the annual variation and the quasi 11-year solar activity cycle (Schwabe-cycle), but also the quasi biennial oscillation QBO or the North Atlantic oscillation NOA which are quasi cyclic oscillations. In order to infer a long-term trend, the elimination of the influence of these variations is required. However, this is not a simple task. Another problem is the search for the reason behind a detected trend and, in case when more than one impact influences the trend, to assess the magnitude of their individual impacts. In particular, an increase of the concentration of different minor constituents in the atmosphere is observed and derived since the beginning of industrialization. However, the solar activity outside of the Schwabe-cycle (e.g. the Geisberg-cycle of an approximate century time-scale) and perhaps other natural variations have also changed since then. The parameters, such as the temperature or the water vapor concentration, have a certain trend and we have to assess which of these parameters share results from the different impacts. In the frame of sophisticated models, one can try to find an answer.

The main goal of the numerical experiment described in this chapter is the reproduction of the water vapor trend in the middle atmosphere based on derived and measured trends of methane, nitrous oxide and carbon dioxide, inclusive of the trend of the solar Lyman-alpha radiation. The effect on mesospheric ozone, NO_x , other minor constituents, and the chemical heating rate are considered in this numerical experiment. The investigation of the impact on stratospheric chemistry is excluded. Special attention is paid to the season and domain of the occurrence of noctilucent clouds NLC.

Direct measurements of atmospheric minor constituents are only available for the recent past. The same is valid for the solar fluxes of Lyman-alpha radiation. There are different indirect data and estimations. The so-called pre-industrial level of methane has been estimated to be 0.75-0.85 ppmv (roughly half the value in the modern atmosphere) [World Meteorological Organization 1999]. The value of methane in recent atmosphere amounts to 1.75 ppmv [Dlugokencky et al., 2003]. The increase of methane in the troposphere was essentially exponential since pre-industrial time. However, for about the last two decades, a decline of the rate of growth has been observed, and increase of the methane seems to be zero for the latest years [Khalil et al., 1993; Dlugokencky et al., 2003]. Although the methane growth rate slowed

down, a constant rate of enhancing methane from 0.825 to 1.7 ppmv was used for the calculation. As methane, in contrast to water vapor, is not subject of the freeze-dry process at the tropopause, the increasing methane concentrations due to intensification of agriculture and cattle-breeding can penetrate into the middle atmosphere. The N₂O concentrations are likewise rising since the time of the intensification of agriculture. An exponential increase of its concentration from a pre-industrial level of 254 ppmv at the surface to currently 324.2 ppmv was taken into consideration.

The increase of CO₂ concentration is considered. There is generally an exponential growth of its concentration but with some variations of its growth rate. The change in the growth rate mirrors the world wars or the oil crisis. The pre-industrial value of carbon dioxide at the ground is estimated to be 275 ppmv. The recent value amounts to about 368 ppmv. The exponential growth between these two values was taken in account in the model.

The Lyman-alpha insolation is the most important radiation dissociating water vapor above the middle mesosphere (roughly above 70 km) and varies strongly with solar activity. The absolute amount and the relative variation of the Lyman-alpha radiation have recently been corrected [Woods et al., 2000]. The old values used by the scientific community were based on measurements by Vidal-Madjar [1975, 1977], Vidal-Madjar and Phissamay [1980], Simon [1981]. The standard flux value for mean solar activity was $3 \cdot 10^{11}$ phot. cm⁻² s⁻¹ and the variation from solar minimum to maximum amounted to a factor of two. The latest values based on UARS measurements according to Woods et al. [2000] amount to $4.65 \cdot 10^{11}$ phot. cm⁻² s⁻¹ and the flux varies between 3.6 and $5.6 \cdot 10^{11}$ phot. cm⁻² s⁻¹ averaged over two years. Below 75 km the radiation within the Schumann-Runge band system becomes increasingly important. Depending on the wavelength, the radiation varies by only a few percentage points. The longer the wavelength is, the smaller the variation. There was an increase in solar activity since the time of first observations of NLC in 1883. The sunspot number and the geomagnetic activity confirm this statement. However, direct Lyman-alpha measurements are only available for the last two and a half solar cycles. In order to reproduce solar output of Lyman-alpha radiation, different solar proxies have been employed. Woods et al. [2000] used direct measurements by means of different satellites such as the AE-E, SME and UARS and filled the data gaps by employing solar proxies. The radiation has been reconstructed back to 1947 using the solar 10.7 cm flux available since that year. The only available direct or indirect solar proxies before 1947 are the sunspot numbers (since 1749) and the geomagnetic activity (aa-index since 1868). The geomagnetic activity varies with solar activity indicated by the sunspot number, however, there is a time delay of about two years between the sunspot number and geomagnetic activity. Surprisingly, this phase shift seems to agree with a delay of the occurrence rate of NLC. Additionally, Thomas and Olivero [2001] used the sunspot number as a proxy and calculated the Lyman-alpha flux based on a quadratic fit. The sunspot number values were quadratically fitted to the Lyman-alpha flux values given by Woods et al. [2000]. From this procedure, a quadratic formula, which can be employed for the time range before 1947 was obtained. When comparing the measured Lyman-alpha flux with the sunspot number, the correlation between the two parameters is poor for time scales of the order of few rotation periods of the sun or shorter. However, for time scales of the order of a year the situation is different. That is why the sunspot number was slidingly smoothed over 11 months for the applying in the model. For the Lyman-alpha flux the expression used in the model is

$$(\text{Lyman-alpha}) (3.396 + 1.71419 \times 10^{-2} S - 1.68423 \times 10^{-5} S^2) \times 10^{11} \text{ photons cm}^{-2} \text{ s}^{-1} \quad (4.1)$$

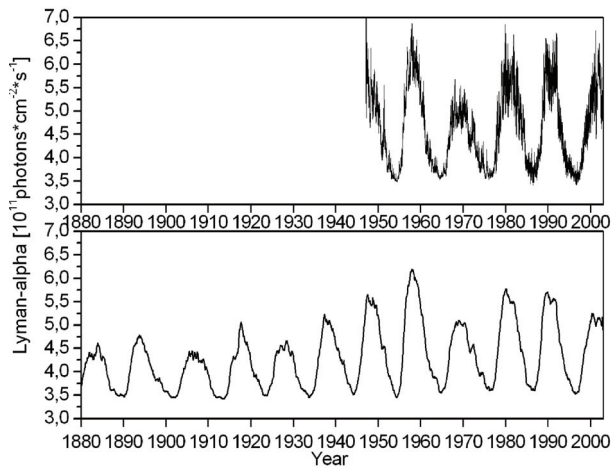
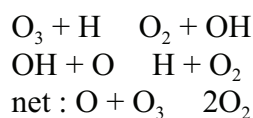


Figure 4.1. Lyman-alpha radiation from measurements (upper panel) and calculations (lower panel) at the top of the atmosphere.

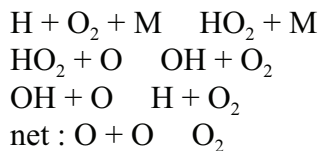
S stands for the 11-month slidingly smoothed sunspot number. Figure 4.1 shows the result of each day measurements of Lyman-alpha flux by Woods et. al [2000] (upper panel) and monthly mean calculated by formula 4.1 (lower panel). The values vary coarsely between 3.5 and 5.6 10^{11} phot. $\text{cm}^{-2} \text{s}^{-1}$ with an exception of the strongest cycle in 1957. One can recognize a general increasing trend of the maximum (and mean) values until the middle of the past century, but after that it begins to decrease. It is important to note that the minima display only a weak trend. These values (Figure 4.1, lower panel) were used to determine the dissociation rate of water vapor in the model.

4.2 Chemical aspects

Methane is finally oxidized to water vapor or decomposed to molecular hydrogen. Although a branch of the methane decomposition results in H_2 , its concentration does not essentially change with height in the stratosphere as it is oxidized by OH or $\text{O}(^1\text{D})$ to H_2O . The methane decomposition starts with a reaction with OH or $\text{O}(^1\text{D})$. The intermediate compounds of the methane decomposition will not be considered in the global model, but, according to Sonnemann et al. [1998], we use the initial decomposition reaction as a measure for the final products. The partitioning depends on the concentrations of atomic oxygen, NO and O_2 as well as the dissociation rates of H_2CO resulting in $\text{CO}+\text{H}_2$ or $\text{HCO}+\text{H}$. In other words, the initial reaction determines the life time of methane, and the follow-up reactions take place very fast. Although molecular hydrogen results from the methane decomposition its mixing ratio is almost constant in the stratosphere. The reason consists in an autocatalytic H_2 oxidation to water vapor [Sonnemann et al., 2005]. Since the oxidation of H_2O by $\text{O}(^1\text{D})$ is the main source of the OH-radicals in the stratosphere, the methane destruction forming H_2O becomes faster the more humid the atmosphere is, meaning the more methane is available. $\text{O}(^1\text{D})$ results from the dissociation of ozone. At least, within the mesosphere, the hydrogen radicals decompose ozone so that a negative feedback occurs there. The ozone destruction entails a smaller $\text{O}(^1\text{D})$ production and that reduces the hydrogen radical formation. However, in the mesosphere the photolysis of water vapor, being the hydrogen radical source, becomes more important with increasing altitude compared with the influence of $\text{O}(^1\text{D})$. Therefore, we expect a decrease of the ozone concentration if the water vapor concentration increases, particularly in the upper mesosphere and the mesopause region but also in the stratopause region, whereas the region between these domains is not so strongly affected. The reason is given, essentially, by two odd oxygen destructing cycles. In the upper mesosphere and mesopause region, ozone destroying cycle involving atomic hydrogen acts [Nicolet, 1970]:



This is a very effective cycle declined in the middle mesosphere by the fact that H will be removed from the atmosphere because it is subjected to the three-body reaction $H+O_2+M \rightarrow HO_2+M$ depending quadratically on the air density. In the middle mesosphere increasing toward the stratopause region, a second cycle becomes increasingly important:



O results from the dissociation of ozone so that this cycle ozone reduces. The relative effect is largest at or a little above the stratopause. Due to the small reaction rate the Chapman reaction $O+O_3 \rightarrow 2O_2$ plays no a great role in the mesosphere. The process becomes more important below the stratopause where the ozone concentration still strongly increases. The reaction is not directly influenced by an increasing humidity, but indirectly, if the concentrations of O and the composition between both constituents, O and O_3 , change by the influence of the hydrogen radicals. Within the stratosphere the impact of enhanced water vapor concentration is not simple to estimate, since the reactions of OH with the chlorine and nitrogen radicals, decomposing ozone and resulting in neutral HCl and HNO_3 , have to be taken into consideration. Here we do not consider the response of increasing H_2O mixing ratios on the stratospheric ozone chemistry. The rising N_2O concentration influences the NO concentration in the middle atmosphere. The oxidation of N_2O by $O(^1D)$, particularly in the stratosphere, results in the formation of two NO molecules. The global middle atmospheric circulation also conveys NO from the stratosphere into the D-layer in moderate and high latitudes in summer whereas the transport in low and equatorial latitudes is more complicated. In a large number of contributions [Taubenheim, 1997; Bremer, 1997, 2001; Bremer and Berger, 2002] the descent of the so-called reflection height of radio-waves has been used as a tracer for middle atmospheric cooling. In contrast to the lower atmosphere, CO_2 cools the upper atmosphere, entailing a decrease of the levels of constant air density. The reflection height is determined approximately by a constant level of electron density. It is assumed, if the solar activity is taken into consideration in the calculations, that in a first approximation a constant level of electron density is connected with a constant level of air density. The electron density within the D-layer is a function of the NO density, and within the water clusters region (below about 85 km), the formation of water clusters depends additionally on the water vapor and CO_2 concentrations. Thus, the estimation of the direct influence of the trends of all minor constituents upon the D-layer should be of great interest. As mentioned, a careful investigation of all influences impacting the D-layer is required to give a definitive answer.

The increase of the CO_2 concentration is jointly responsible for the warming of the troposphere and the cooling of the atmosphere above. The direct influence upon the chemistry is very small below the upper mesosphere. CO_2 is increasingly dissociated into CO and O in the mesosphere. CO reacts with OH and returns to CO_2 . Only a radical conversion takes place in this reaction from OH to H which influences the ozone chemistry rather marginally. As mentioned above, the most important impact is connected with the ion-chemistry. The model under consideration does not operate interactively. Hence, the CO_2 increase is not considered in the dynamic model but only in the chemical transport model. In other words, the change of the dynamical parameters such as temperature and global circulation is not taken into account.

4.3 Water Vapor

The hygropause separates the wet troposphere from the dry middle atmosphere. Due to a freeze-drying process water vapor concentration drops from several hundred ppmv in the troposphere to approximately 4 ppmv above the hygropause. The water vapor mixing ratio at the hygropause was used as lower boundary condition in the model because it is not possible to simulate the complicated tropospheric water vapor content and the freeze-dry process in the frame of our model. In order to calculate the water vapor trend for the middle atmosphere it is important to consider the possible trend of the lower boundary conditions. Evidence for a changing hygropause was given by Foster and Shine [1999]. They found a strong increase in the stratospheric water vapor in the latest past [Oltmans and Hofmann, 1995; Evans et al., 1998], which could only be explained by the methane increase up to 40% [Foster and Shine, 1999]. This indicates that the pre-industrial mesosphere was essentially dryer than it is now. There are two possible reasons.

The globally averaged water vapor flux within the stratosphere is directed downward [Sonnemann and Körner, 2003]. The methane moves advectively and diffusively through the tropopause into the middle atmosphere and will be oxidized to water vapor there, forming a water vapor mixing ratio maximum close to the stratopause. An upward and downward directed water vapor flux results from this peak. This is the global mean picture, which, of course, can differ locally or temporally. The increase with height of the globally averaged water vapor mixing ratio is characterized by a positive gradient. The question arises: does the gradient essentially depend on the magnitude of the water vapor maximum at the stratopause, or is it in first approximation a conservative quantity? In the latter case, the hygropause becomes proportional to the water vapor increase and also more humid while in the former extreme case, the gradient becomes increasingly larger if the water vapor mixing ratio at the hygropause is a conservative quantity (actually an unrealistic picture).

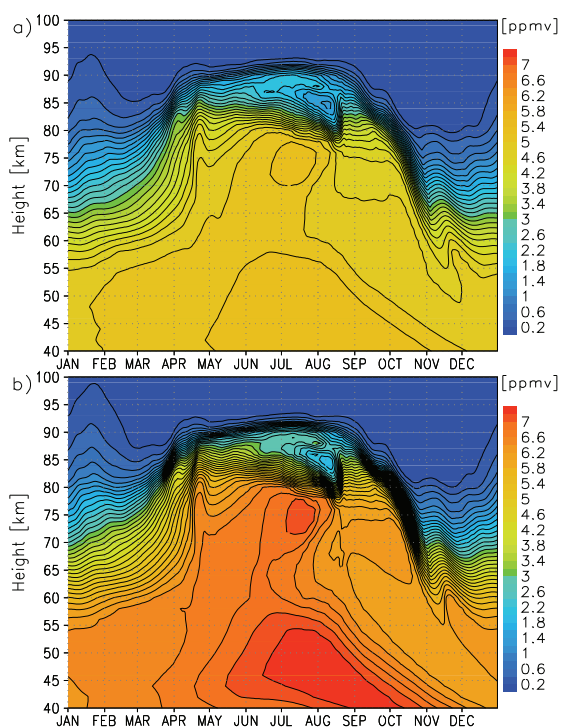


Figure 4.2. Water vapor mixing ratio [ppmv] at 67.5° N for year 1890 (a) and 1997 (b).

Due to the increase of the concentrations of the different greenhouse gases the troposphere becomes warmer and as a consequence more humid. Water vapor is the most important greenhouse gas. On the other hand water vapor is governed by the other greenhouse gases (CO₂, CH₄, N₂O, O₃ etc.) whose concentrations rise owing to anthropogenic activity. Thus, the humidity increase at the hygropause should also be controlled by the change in the tropospheric conditions. These simple arguments only provide a qualitative answer that the hygropause was dryer in 1880 than in current times. However, it is not possible to determine the true value thus far as there are no measurements before the second half of 20th century.

Figures 4.2a and 4.2b display the seasonal sections of the water vapor distribution at 67.5° N in 1890 and 1997 (both years of low solar activity) derived from the model, respectively. The figures show seasonal patterns typical for measurement

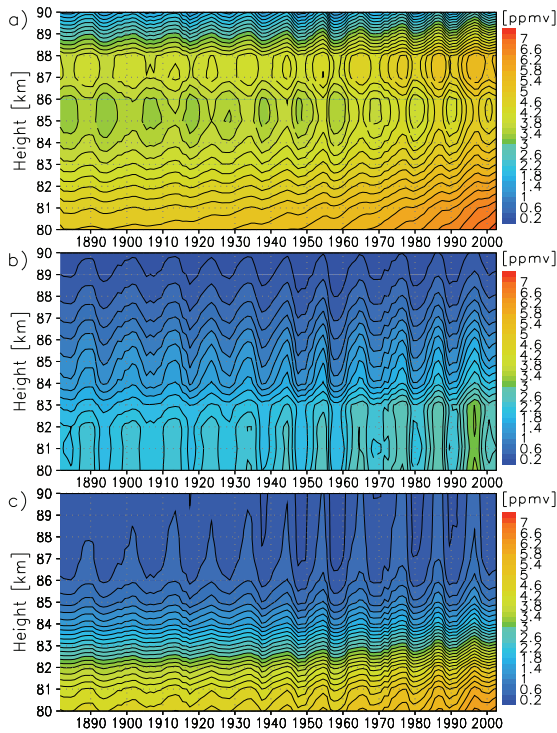


Figure 4.3. Water vapor mixing ratio at midnight near summer solstice (1st July) for 67.5° N (a), 42.5° N (b) and 2.5° N (c).

amplitude of the variation with the solar cycle [Sonnemann et al., 2004]. In contrast, a downward wind, as appears during the winter season, conveys air strongly influenced by the variable Lyman-alpha radiation to lower heights.

Figure 4.4 display the increase of the water vapor mixing ratio at different selected mesospheric altitudes (80, 83, 86 and 90 km) at 67.5° N for summer solstice (1st July). The solar cycle variation begins to be noticeable above 80 km. Within the NLC region the impact of the solar radiation is reduced, but the amplitude of water vapor due to the solar cycle impact possesses a considerable gradient between 80 and 90 km. At 80 km only a small variation exists whereas a pronounced variation occurs at 90 km. Although the condensati on nuclei for the NLC particles will be created in altitudes close to the temperature minimum at about 86 to 89 km, the NLC particles sediment and grow according to the surrounding water vapor mixing ratio, meaning the influence of the solar activity cycle on the NLC occurrence rate is dampened by the upward directed vertical wind. However, the temperature has the strongest influence on the growth of NLCs, but its variation with the solar cycle is not modeled.

Figure 4.5 depicts the calculated annual variation of the relative deviation (RD) of a diurnally averaged water vapor mixing ratio (MR) between 1997 and 1890 at 67.5° N according to

and modeling but with essentially lower absolute amounts for the early case. The diurnal variation of the water vapor mixing ratio is not significant below 80 km, but above 80 km, in the region of NLC and PMSE formation, it becomes increasingly stronger. Figure 4.3a displays the altitude-time section of the water vapor mixing ratio at 67.5° N near north summer solstice (1st July) for midnight. One can recognize the general increase of the mixing ratio at constant height. Above about 80 km the solar cycle is clearly mirrored. Figures 4.3b and 4.3c show the same relations at middle and low latitude. One finds that the influence of the solar cycle penetrates essentially deeper at lower latitudes. The reason is given by the global vertical wind patterns. The upward directed vertical wind in high and moderate latitudes during the summer season lifts air that is not strongly influenced by the variations in solar activity from the lower domain into heights where the variable Lyman-alpha radiation still penetrates. The comparison between the characteristic transport time and the characteristic time of photolysis is the decisive criterion for the

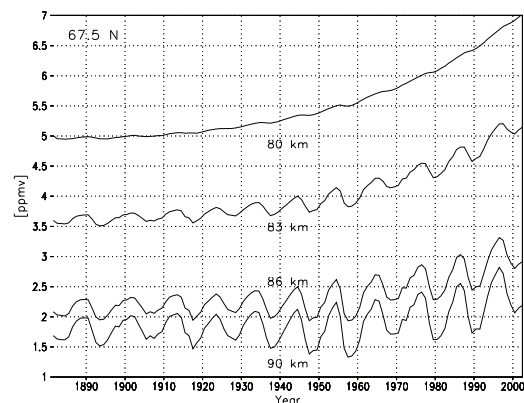


Figure 4.4. Diurnally averaged water vapor mixing ratio for summer solstice (1st July) at 67.5° N for different altitudes.

the expression:

$$RD = \frac{(MR(1997) - MR(1890))}{MR(1890)} \cdot 100\% \quad (4.2)$$

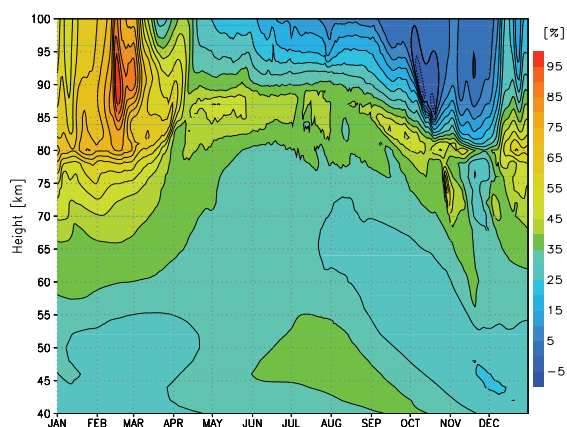


Figure 4.5. Relative deviation of diurnally averaged water vapor mixing ratio at 67.5° N.

north spring equinox (1 April) are shown in Figures 4.6a and 4.6b respectively. The figures demonstrate that the relative increase of the middle atmospheric humidity depends on altitude, latitude and season. The strongest deviations occur just in the mesopause region. In the region of NLCs and PMSEs in high summery latitudes marked by upward directed vertical winds, the relative deviations reach 35-45 %. A reason for the strong relative deviation in the mesopause region may be given by the autocatalytic water vapor production below 65 km [Sonnemann et al., 2005] and the meridional transport. The more humid the atmosphere, the more effective the process of autocatalytic water vapor production.

The relative deviation is not enough informative because in regions of low values of the water vapor mixing ratio it can be large but the absolute change is not significant. Vice versa, if values of water vapor mixing ratio are large enough even for small relative deviation a high absolute changes can occur. Figure 4.7 shows annual variation of absolute deviation of water vapor mixing ratio at 67.5° N between 1997 and 1890. The regions of strongest absolute deviation correspond to regions of maximums water vapor (Figure 4.2b) and occur during the summer at altitudes approximately 45-55 km and 70-80 km. Figures 4.8 and 4.9 correspond to figures 4.6a and 4.6b but show the absolute deviation of water vapor mixing ratio. As Figure 4.8 makes clear the

Up to 85 km, the water vapor trend is generally positive. There is a range of slightly decreasing water vapor mixing ratios above this border in September/October, whereas the increase is very strong in this domain from January until April. The absolute values are very small there so that weak changes entail large relative variations. The main reason for this behavior is the fact that the Lyman-alpha radiation also slightly increased during the years of solar activity minimum and thus it was higher in 1997 than in 1890.

The relative deviations in a latitudinal section for north summer solstice (1st July) and north spring equinox (1 April) are shown in Figures 4.6a and 4.6b respectively. The figures demonstrate that the relative increase of the middle atmospheric humidity depends on altitude, latitude and season. The strongest deviations occur just in the mesopause region. In the region

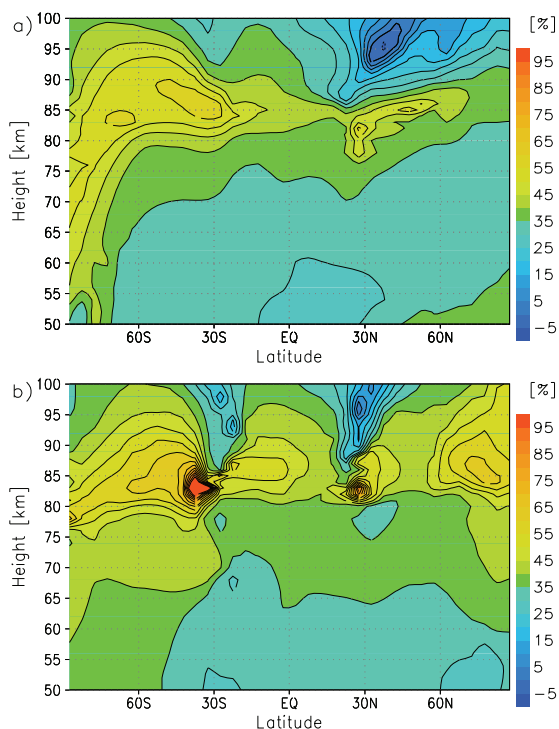


Figure 4.6. Relative deviation of diurnally averaged water vapor mixing ratio between 1997 and 1890 in an altitude-latitude section for north summer solstice (a) and for spring equinox (b).

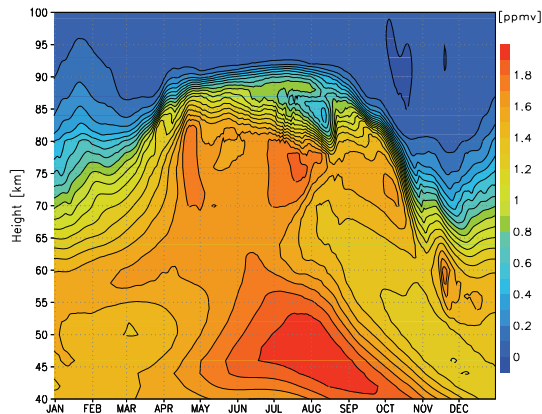


Figure 4.7. Absolute deviation of diurnally averaged water vapor mixing ratio at 67.5° N.

increases with height up to the mesopause region. This statement reflects the fact that methane first has to be converted into water vapor and molecular hydrogen during the upward motion through the atmosphere but there is a positive feedback between decreasing ozone and increasing water vapor as it will be discussed in the section 4.4.

water vapor mixing ratio in NLCs region has increased by 1.5-1.7 ppmv. It is advisable to use solar minimum conditions, as the Lyman-alpha flux for the minimum years did not show a change (the change from minimum to minimum is small), whereas the flux in the maximum phases changes strongly from cycle to cycle. The largest relative deviations can be found during winter. However, considering the absolute growth of the mixing ratio values, the strongest increase is in summer. The relatively small values in the lower thermosphere of the northern middle latitudes are connected with a strong downward directed vertical wind. Generally, the magnitude of the RD

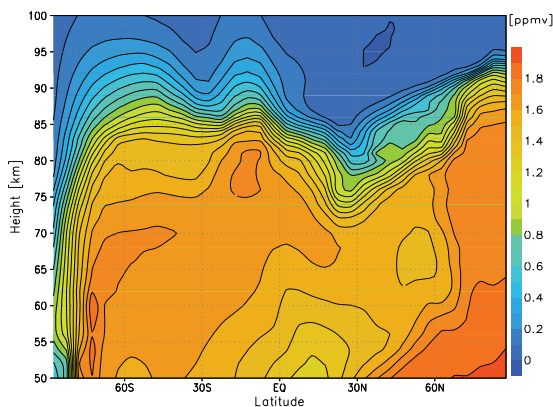


Figure 4.8. Absolute deviation of diurnally averaged water vapor mixing ratio for north summer solstice (1 July).

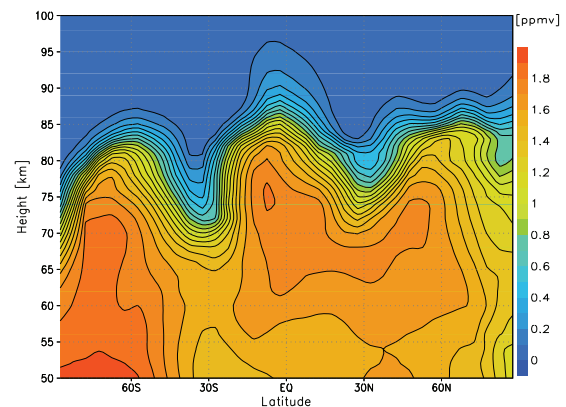


Figure 4.9. Absolute deviation of diurnally averaged water vapor mixing ratio for north spring equinox (1 April).

4.4 Ozone

Ozone is the main source of $O(^1D)$ oxidizing water vapor (see 3rd zero cycle for water vapor in appendix E). The production is strongest near the daytime secondary ozone maximum just between 85 and 90 km - the altitude of the NLC-PMSE region. This is a positive feedback process enhancing the water vapor mixing ratio stronger than expected from the methane increase alone. Below 65 km there is no strong reduction of the ozone mixing ratio, although water vapor increased by more than 30%. The explanation is simply given by the fact that the odd oxygen concentration increases with decreasing height stronger than the hydrogen radicals depending on the rising methane concentration. Consequently, the odd oxygen loss reaction $O+O_3 \rightarrow 2O_2$ becomes more important compared to the loss reactions when including the hydrogen radicals. Although the reaction rate of this process is relatively small, this disadvantage is compensated

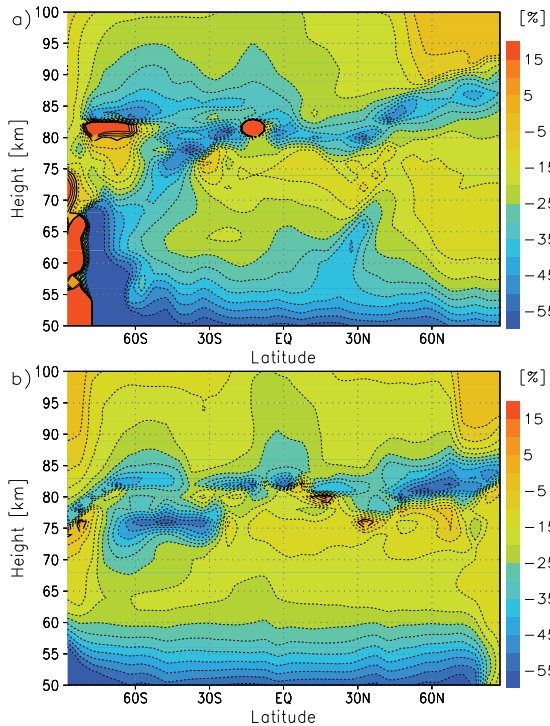


Figure 4.10. Relative deviation of diurnally averaged ozone mixing ratio for north summer solstice (a) and for spring equinox (b).

values of water vapor decrease again owing to the strong decrease of ozone with increasing height. For completeness of the discussion, Figures 4.11 and 4.12 show absolute deviation of the ozone mixing ratio for north summer solstice and spring equinox, respectively. During the north summer solstice (Figure 4.11) the largest absolute decrease of the ozone mixing ratio occurs at 50 km from 60° S to 60° N and at 85-95 km near winter pole and around 30° N in the summer hemisphere and equals 0.9-1.2 ppmv. During the north spring equinox (Figure 4.12) the regions of largest decrease is placed at 50 km between 60° S and 60° N and in the mesopause at latitudes around 30° in both hemispheres and reach values of 0.7-0.9 ppmv.

The chemical system responds in a nonlinear manner in the mesopause region. This

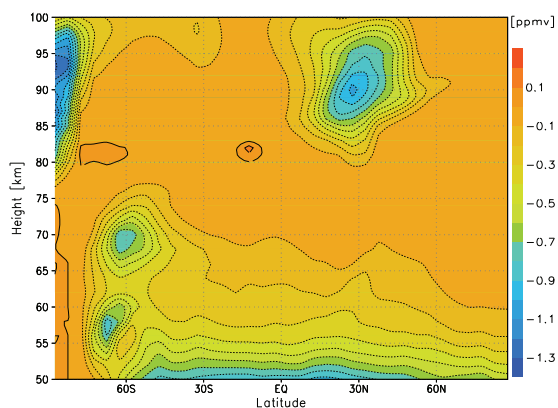


Figure 4.11. Absolute deviation of diurnally averaged ozone mixing ratio for north summer solstice.

by the increasingly larger concentrations of O and O₃ with decreasing height than the concentrations of the hydrogen radicals.

Figures 4.10a and 4.10b depict the relative deviation of the diurnally averaged ozone concentration in a latitudinal section for north summer solstice and equinox conditions. Generally, the ozone concentration decreases the most around the mesopause and stratopause, with the exception of a small area in high latitudes. At and above the stratopause a further region of stronger ozone loss is to recognize whereas the middle mesosphere is less strongly impacted. There is a remarkable reduction of ozone contributing to the general cooling of the mesosphere since 1890. In the upper mesosphere/mesopause region almost all methane is decomposed. The further increase of the relative values of the water vapor mixing ratios within the mesopause region, as can be seen in figure 4.6a, essentially results from the simultaneous decrease of ozone due to an amplified formation of hydrogen radicals resulting from water vapor increase. In the lower thermosphere, the relative

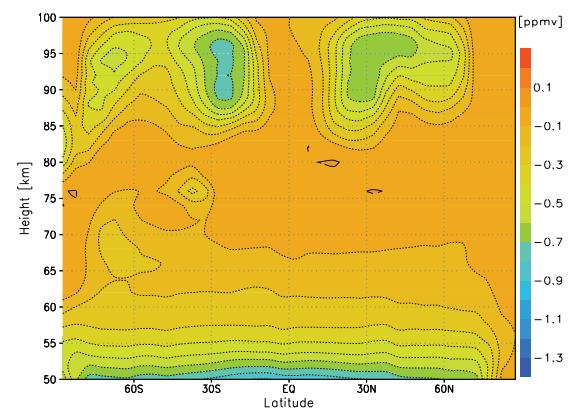


Figure 4.12. Absolute deviation of diurnally averaged ozone mixing ratio for north spring equinox.

finding was investigated in a large number of publications by Sonnemann, Feigin and coworkers and other groups. As the latitudinal sections in Figures 4.10a and 4.10b demonstrate, different regions of an ozone increase (red areas) occur below the mesopause. The cause is a nonlinear response of the photochemical system. As the integration time step has to be relatively large for trend calculations (15 minutes) and, additionally, the odd oxygen species are treated as family, effects such as subharmonics or chaos cannot occur in the calculations as large time steps and the family concept suppress these phenomena [Sonnemann and Grygalashvyly, 2005]. Apparently the system tends to create a bistable behavior.

Figure 4.13 shows an example of the diurnally averaged ozone mixing ratios at 81 km altitude in two different latitudes for 1st January. A bistable behavior seems to occur which, in one case, appears under conditions of small water vapor concentrations and disappears for higher values, while, in the other case, it becomes dominant for larger water vapor concentrations. The behavior is triggered by the solar cycle. Figure 4.14 exhibits an example at 83 km altitude and 22.5° N latitude for 1st July. A clear decreasing ozone trend is recognizable, but beginning after 1930 a bistable response occurs. The possibility of a trigger solution under the condition of a hydrogen flux was discussed in Yang and Brasseur [1994]. Our results may hint at a bistable behavior but, on the other hand, the integration of the system is too coarse to get a definitive answer.

Below the mesopause, the system tends to respond in a nonlinear manner. However, it is impossible to give a definitive answer on the basis of a relatively coarse integration procedure, so an improved investigation is necessary. The chemical reasons for a possible trigger solution just around the ozone minimum at 80 km were discussed in Hartogh et al. [2004]. Yang and Brasseur [1994] showed its existence in a very simplified model. Certainly, the ozone decrease in the stratopause region is more important. Different groups discussed the so-called ozone deficit problem [e.g., Eluszkiewicz et al., 1993; Siskind et al., 1995] consisting of a systematic underestimation of ozone by the standard models only in the stratopause region (upper stratosphere-lower mesosphere). Crutzen et al. [1995] did not find a deficit. This finding points to the fact that the ozone determining processes are not completely understood. We mentioned already that the second catalytic cycle is responsible for the decrease if the humidity increases. This cycle acts, of course, in the whole atmosphere, but hydrogen radicals increase faster toward the stratopause than atomic oxygen decreases. A second fact has to be taken into consideration: namely, the positive feedback between ozone and the ozone dissociation rate. This effect was first taken into calculation in Sonnemann et al. [2005]. The ozone dissociation rate is determined

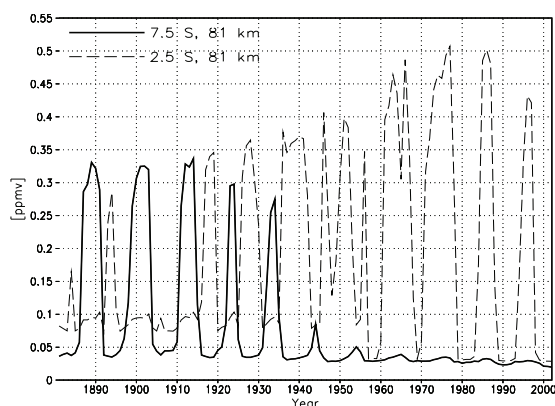


Figure 4.13. Diurnally averaged ozone mixing ratio at 81 km, 2.5° S (dashed line) and 7.5° S (solid line) for 1st January.

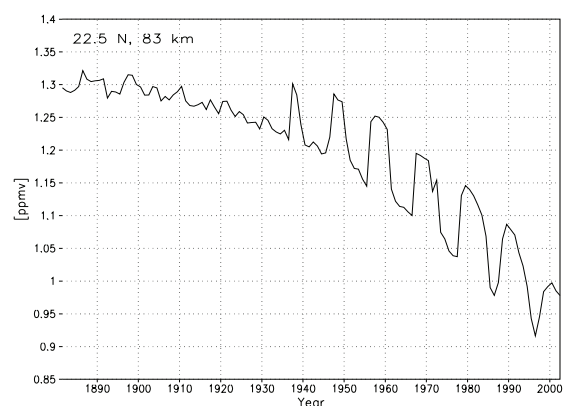


Figure 4.14. Diurnally averaged ozone mixing ratio at 83 km, 22.5° N for 1st July.

by the absorption of the radiation of ozone itself. This is the so-called self-shielding effect. An ozone decrease enhances the radiation dissociating ozone, which amplifies further ozone destruction in the domain where the ozone dissociation rate declines the most with decreasing height. This is approximately the altitude below 60 km, including the extended stratopause region. Above this height a change of ozone has no large absorption effect. This feedback is usually not considered in the models, but the measurements reflecting the reality contain this effect. A decrease of ozone by 10 to 14 % just at the stratopause but not above this domain up to 75 km was inferred from microwave measurements in Lindau (52.66° N, 10.13° E), if comparing the observations with the ozone reference model derived from SME-satellite measurements 20 years earlier. This finding could be an indication of an increasing humidity in the latest 20 years. In the upper domain around the mesopause, the solar influence is essentially stronger and the relations are exceedingly more complicated than at the stratopause.

The ozone decrease in the mesosphere/mesopause region was an expected effect because the concentrations of the hydrogen radicals increase, and particularly hydroxyl, and due to the amplified first catalytic cycle (see section 4.2) including H and OH as catalysts. Thus, the trend of hydroxyl will be discussed in the next section 4.5.

4.5 Hydroxyl

A very important change of the chemically active minor constituents concerns OH in the OH-layer. The airglow in the Meinel bands system is used by different groups to derive the temperature and for analysis of gravity waves [Taylor and Garcia, 1995; Taylor, 1997; Taylor et al., 1998], but OH itself is also a subject of investigation [e.g., Offermann and Gerndt, 1990; Summers et al., 1996; Bittner et al., 2002]. The Meinel bands airglow layer results mainly from the reaction $O_3 + H \rightarrow OH^* + O_2$. The main loss process of the vibrationally excited states is quenching by air particles. The chief loss of OH is the reaction with atomic oxygen. Since O decreases with decreasing height but the air density increases, the OH-layer lies somewhat lower than the OH*-layer. Considering the production term of OH*, H increases but O₃ decreases, reducing the airglow layer. Depending on season, latitude and vibrational number, the calculations show 20-50% decrease of the OH* concentration, but the altitude of the layer remained over the years. Thus, airglow measurements can be applied for the study of anthropogenic changes in the mesopause region. In contrast to this finding, the OH-layer became more pronounced owing to the decline of the loss term by reaction with O. Simultaneously, the

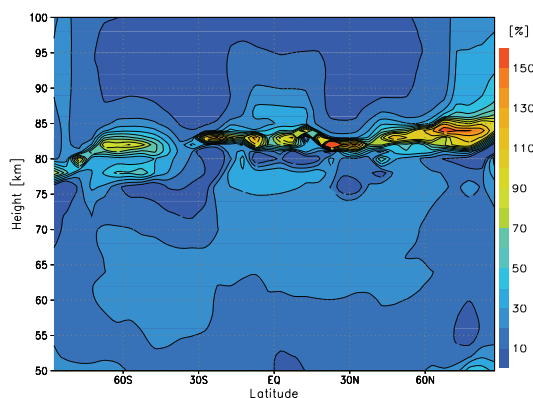


Figure 4.15. Relative deviation of diurnally averaged hydroxyl mixing ratio for north spring equinox.

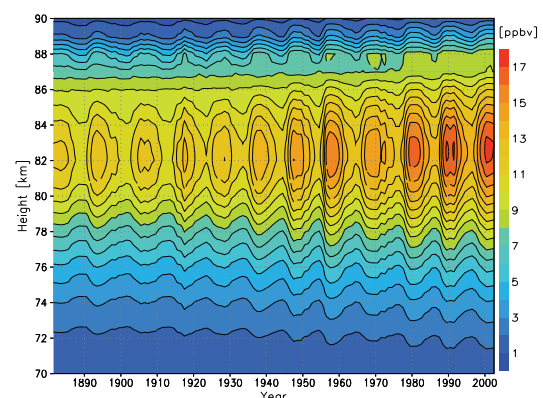


Figure 4.16. Trend of the OH-layer at 67.5° N for north summer solstice (1st July).

height of the OH-layer increased.

As an example, Figure 4.15 depicts the relative deviation of the diurnally averaged hydroxyl mixing ratio according to the conditions shown in Figure 4.10b (1st April). The OH-layer is located in the mesopause region. Figure 4.16 displays its increasing trend of diurnally averaged hydroxyl mixing ratio at 67.5° N for summer solstice, which is strongly modulated by the solar cycle.

4.6 Carbon Monoxide

The most spectacular anthropogenic increase of a minor constituent is that of CO₂. As mentioned, here the change of the mesospheric chemistry owing to the CO₂ increase is only briefly considered and the influence of the thermal regime of the middle atmosphere is neglected. There are some contributions dealing with the impact of a CO₂ doubling on the thermal regime

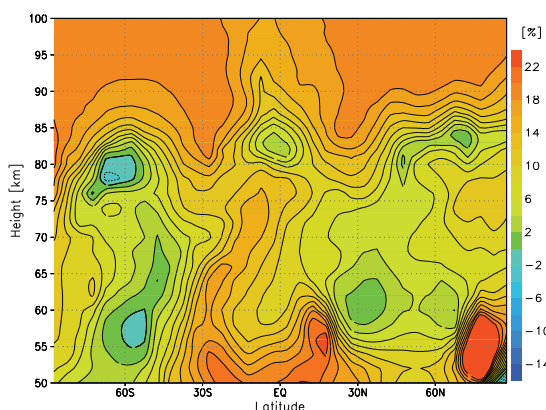


Figure 4.17. Relative deviation of diurnally averaged CO mixing ratio for north spring equinox (1st April).

of the upper atmosphere [Berger and Dameris, 1993; Keating et al., 2000; Bremer and Berger, 2002], but no study additionally considers the response of the chemistry in the MLT region. Figure 4.17 shows the relative deviation of the CO concentration for 1st April. The increase of the CO mixing ratio depends on height, but also on latitude and season. The lifetime of CO is relatively long (for [OH] 10⁷ cm⁻³ results 6.67 10⁵ s). The impact on the composition of the hydrogen radicals is very small and not shown here as only a radical conversion takes place from OH to H and no radical loss occurs. However, the distribution of OH influences the mixing ratio of CO. The figure displays a generally negative trend in the stratosphere. The reason consists in the fact that the production of OH increased essentially stronger between 1890 and 1997 than CO in the stratosphere, so that the loss of CO by OH is more efficient than the increased formation of CO by the photolysis of CO₂. In the mesosphere the picture is not uniform. Although CO increased in most regions, there are distinct domains of a small inverse trend resulting from larger OH-concentrations there.

4.7 NO_x

The primary mechanism by which extreme solar events affect the middle atmosphere is via production of nitric oxide (NO) after energetic particle impacts on molecular nitrogen and oxygen. The NO_x catalytic cycle is the primary loss mechanism for ozone in the middle stratosphere. Solar storms can also affect the stratospheric ozone by downward transport of NO_x into the stratosphere.

However, highly energetic solar protons can result in immediate NO_x enhancements directly in the stratosphere, although this happens very seldom. More frequently, energetic protons and electrons lead to a delayed enhancement of stratospheric NO_x. That is, production of NO_x first occurs in the thermosphere and mesosphere. Under appropriate conditions of downward directed vertical wind, the NO_x produced will then descend into the stratosphere.

The calculations presented in this work were carried out by employing an exponential

increase of nitrous oxide (N_2O) from a value of 254 ppbv in the year 1880 up to the present value of 310 ppbv. N_2O is a relatively inert species in the lower atmosphere and as a source in the atmosphere has, until recently, been attributed entirely to natural processes. Soil emissions from nitrification and denitrification processes are thought to be the main source of nitrous oxide to the atmosphere. The emissions from the oceans also play a significant role. The tremendous increase in fertilizer use for agricultural practices increases the amount emitted from the soil, producing an observable anthropogenic impact. Biomass burning is also thought to contribute a significant amount to the atmosphere. The importance of nitrous oxide is twofold. First, its global warming potential (GWP) is 200 times greater on a molecule-by-molecule basis than carbon dioxide. Second, the two significant removal processes of oxidation by $O(^1D)$ resulting in two nitric oxide (NO) molecules and photolysis by higher energy ultraviolet radiation, where it is also converted to nitric oxide. This additional source of nitrogen oxide in the stratosphere can then undergo catalytic destruction of ozone, leading to higher levels of ultraviolet radiation reaching the lower atmosphere.

4.8 Chemical Heat

The chemical heating is a very important diabatic heating source influencing the thermal conditions under which NLC will be formed. One could expect that a decline of the odd oxygen concentrations should also reduce the chemical heating rate, but the concentrations of the odd hydrogen constituents increased at the same time, so that this fact compensates the negative effect. The chemical heating is, in essence, determined by the stepwise recombination of atomic oxygen to molecular oxygen leaving its latent chemical energy at the place of recombination. The latent chemical energy is both downwardly transported from the thermosphere and locally created by the formation of O due to the dissociation of O_2 . These processes are not directly affected by the increasing humidity. The photolysis of water vapor itself plays no great part in the energetic balance. The stepwise recombination of atomic oxygen takes place via the formation of ozone and both the formation of OH and HO_2 within the catalytic cycles. As a consequence, the height of recombination changes if the hydrogen radical concentration alters. This process depends on the vertical wind direction. As discussed above, the chemistry of the middle atmosphere represents an intricate nonlinear system. This system is characterized by different feedbacks. One of these mechanisms is connected with the production of chemical heat, which acts in two ways: it alters the wind system and particularly the vertical component, and changes the chemical

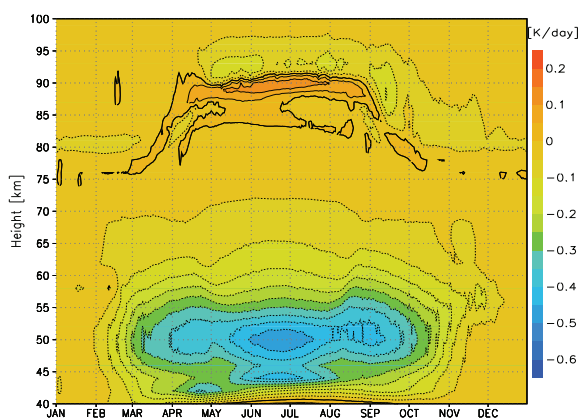


Figure 4.18. Annual variation of absolute deviation of diurnally averaged chemical heating rate at 67.5° N.

reaction rates of the temperature-dependent reactions. The calculations revealed two regions of strong influence. Figure 4.18 shows the absolute deviation of a diurnal chemical heating rate at 67.5° N between 1890 and 1997. The relative deviation of the chemical heating rate is less informative. The figure displays two regions marked by the strongest absolute changes occurring during summer. The first region is placed at the summer mesopause (between 87 and 91 km) and is characterized by the strongest increase of chemical heating rate. The most significant reactions for the chemical heat in the region 85-90 km are $OH+O$, $O+HO_2$ and O_3+H .

Hence, the increase of the chemical heating rate in this region is caused by the rising humidity in the mesopause region due to the enhanced odd-hydrogen production; however, this is damped by the fact that the concentrations of the odd oxygen constituents decrease with increasing the concentrations of the odd hydrogen constituents. A changed thermal regime feeds back to the wind system and influences the chemical reaction rates. The second region of strongest absolute deviation is located close to the stratopause and has a negative sign. The main reaction of the production of chemical heat in the stratopause region is given by the three-body reaction $O+O_2+M$. Its reaction rate increases with decreasing temperature. Consequently, the system is characterized by a negative feedback in both regions. Figure 4.19 shows the latitudinal behavior of the absolute deviation of the diurnal chemical heating rate near north summer solstice (1st July).

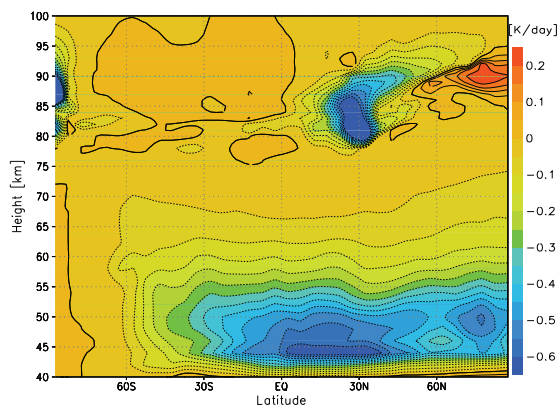


Figure 4.19. Absolute deviation of diurnally averaged chemical heating rate for north summer solstice (1st July).

The figure illustrates the latitudinal extension of both regions. The trend of chemical heating rate has negative sign from equator to approximately 50° N for all heights during summer season, but it change the sign from 50° N to north pole in mesopause region.

One of the most interesting questions is, how much the change of the composition of atmospheric minor constituents influenced the condition for the formation of ice particles in the NLC region, meaning the conditions in the summery high latitudes. The temperature has the most important influence on the creation of NLCs and PMSEs. It is assumed to be dropped in the middle atmosphere due to the amplified radiative cooling by increased CO_2 concentration. However, the cooling is not a homogeneous process affecting all altitudes in the same way. A mysterious fact is the finding that the height of the NLC has not noticeably declined since the time of first observation in 1883 [Jesse, 1885, 1891; von Zahn and Berger, 2003]. The term “equithermal submesopause” was introduced by Lübken et al. [1996] and reflects the significant repeatability of the mean mesopause temperature during the last 40 years and the NLC height since first observation. Recently, Lübken [2001] found no temperature trend in the mesosphere in high latitudes in summer. These are unexpected findings not simple to interpret. A cooling of the whole middle atmosphere should shift the levels of constant air density downward, as assumed in the papers about the change of the radio-wave reflection height using the technique of the phase-height measurement [e.g., Taubenheim, 1997; Bremer, 1997, 2001; Bremer and Berger, 2002]. In the mesopause region, the concrete height is decisive for the sign of the temperature change if the levels of constant air density decline. For a height above the mesopause (defined by the temperature minimum), the temperature increases owing to its positive gradient and may be compensated by a cooling trend in the vicinity of the considered height. Below the mesopause, according to the negative temperature gradient, the temperature decreases. The degree of super-saturation is given by the Clausius-Clapeyron Equation. A drop of the levels of constant pressure also entails a decrease of the partial pressure of water vapor. At a constant height, this could be compensated by the increasing humidity. Both influences, the decrease of temperature and rise of humidity, should increase the occurrence rate of NLC, as indeed has been observed since the time of their first observation [e.g., Gadsden, 1998]. The only question is why this did not lower their lower border, which is located below the mesopause. The explanation, possibly, is that the positive trend of chemical heating rate at high

latitude in mesopause (Figures 4.18 and 4.19) partially compensate the cooling due to CO₂ increase. These both processes are in competition and the result is the absence of temperature trends in mesopause at high latitudes during the summer, as it was found by Lübken [2001]. Thus, the chemical heat can play a role in stabilizing of mesopause and formation of “equithermal submesopause” at high latitudes in summer. In light of our calculations, at least in the mesopause, there is no contradiction between measurements of Lübken [2001] and Hauchecorne et. al. [1991], or Bremer and Berger [2002], who found in the mesosphere and mesopause at mid latitudes (44° N and 50.7° N, respectively) negative trends of temperature, because the trend of chemical heating rate at mid latitudes is negative for all altitudes during the summer (Figure 4.19) and cannot compensate the anthropogenic cooling. Apparently, this static picture is not comprising enough. The global polar anti-cyclone changes and with it the complete circulation. Possible weakening of the upward vertical wind as a result of the cooling of the underlying atmosphere decreases the adiabatic cooling. The collision between CO₂ and O seems to be an efficient cooling process [Crutzen, 1970]. A reduction of the atomic oxygen concentration also makes this cooling process more inefficient. As it was mentioned already the change of the chemical heating rate tends to increase in that area and season. Breaking gravity waves are a rather important diabatic heating source controlled by processes in the lower atmosphere which are subjected to climatic change. Normally, the models are tuned by a more or less arbitrary spectrum of gravity waves so that a required global temperature distribution results. Also, the propagation of planetary waves and, in the winter season, the occurrence of sudden stratospheric warming influences the thermal regime of the mesopause region. This enumeration of influences and the brief discussion of them make clear that no simple answer can be given. In order to investigate the trend of the conditions in the NLC region, at least, an interactive operating model is required considering all essential processes. Also an increase of the occurrence rate of NLC with increasing humidity is expected, as suggested by Thomas et al. [1989].

4.9 Summary and Conclusions

The influence of the rising concentrations primarily of methane, but also of dinitrogen oxide and carbon dioxide since the pre-industrial era was investigated. The global 3D-model COMMA-IAP designed for the exploration of the MLT-region and particularly the extended mesopause region was used for calculations. A quadratic fit using the sunspot number available since 1749 as the only solar proxy for the Lyman-alpha flux before 1947 was derived to calculate the solar Lyman-alpha flux back to the pre-industrial time. The fit was based on Lyman-alpha flux values derived by Woods et al. (2000) available since 1947. The calculated Lyman-alpha flux values have been utilized to determine the water vapor dissociation rate. The water vapor trend analysis is based on estimated methane trends since the pre-industrial era. An exponential increase of methane was taken for calculations. An unsolved and intricate problem for the model calculations consists of the water vapor mixing ratio at the hygropause during the time range of trend calculation. It was assumed that the hygropause was dryer at the pre-industrial time than presently and used a very conservative value of 10 %. The methane oxidation results in a more humid middle atmosphere. According to the rising methane concentration, that yields two water vapor molecules per methane molecule, the water vapor mixing ratio increased. The increase of water vapor mixing ratio depends on height, season and solar activity. A small time delay of a few years is caused by the slow transport through the middle atmosphere. The solar influence on the water vapor mixing ratio due to the variation of the Lyman-alpha radiation is insignificant

below about 80 km within summery high latitudes, but it becomes increasingly more important above this altitude. The increasing water vapor concentration should impact the NLC occurrence rate, but the relations in the mesopause region are very intricate. The rising water vapor concentrations enhance the hydrogen radical concentrations and these reduce the mesospheric ozone, particularly in the mesopause region, owing to catalytic odd oxygen destruction processes. A second region of stronger ozone decrease is located in the vicinity of the stratopause. This model assertion was confirmed by microwave measurements of ozone in middle latitude at Lindau, Germany when comparing the observations with data of the ozone reference model established from satellite measurements 20 years ago. The reduced ozone concentrations form less amounts of $O(^1D)$ being an effective H_2O destroyer. As a result the H_2O concentration increases in the mesopause region stronger than expected from the methane increase only. Another influence of increasing hydrogen radical concentrations concerns the OH-layer, which became more pronounced and the maximum height increased a little. The change of the chemical heating rate was discussed. In the mesopause region the chemical heating rate increased whereas it decreased in the stratopause region. The positive trend of chemical heating rate at the high latitude mesopause during summer could play a role of stabilizing mechanism and could be one of the reasons of a “equithermal submesopause”. In this work we did not consider the change of NO_x due to the increasing N_2O concentrations.

Increasing CO_2 concentrations somewhat increase the CO content of the mesosphere with the exception of some regions where CO slightly decreases. In these areas the increase of OH over-compensates for the rise of CO. The influence of CO upon the chemistry is very small. This is also valid for the impact of the NO_x chemistry upon the odd oxygen-odd hydrogen system of the MLT region. The main effect of increasing carbon dioxide is connected with a cooling of the upper atmosphere. The trend analysis revealed a decrease of CO in the stratosphere as a result of relatively stronger growth of OH as the only CO destroyer. The cooling, and consequently the change of the dynamics and the chemical reaction rates, is not considered in the model. A bistable state of the chemistry around 80 km hints at a nonlinear response of ozone, but this effect has to be investigated in more detail. The model does not run interactively thus far and the dynamic model is based on the state of the present atmosphere, so the annual variations of the dynamical fields did not change from year to year over the calculated period. Hence, all trends result from the chemistry and, to a small extent, from the variation of the Lyman-alpha radiation. Thus the model reproduces the present atmosphere very well but there could be some changes of the dynamical parameters (wind vector, temperature, pressure) for the pre-industrial atmosphere.

Chapter 5

Ozone

5.1 Middle Mesospheric Maximum (MMM) of Ozone Near the Polar Night Terminator

Ozone measurements by means of the Microwave Limb Sounder (MLS), on board UARS since 1992, and by the Cryogenic Infrared Spectrometers and Telescopes for the Atmosphere (CRISTA), instruments flown on board of the Shuttle Palette Satellite in August 1997, brought evidence for a singular area of enhanced ozone concentration around an altitude of 72 km near the polar night terminator [Marsh et al., 2001]. The same finding was shown by ground-based millimeter wave measurements at the ALOMAR facility from October 1995 to June 1996 [Jarchow et al., 2000]. The original ground-based device and refurbishments have been described in Hartogh et al. [1991] and Hartogh and Jarchow [1995]. The phenomenon has been termed “tertiary ozone maximum” and interpreted by a decrease in atomic oxygen loss owing to the absorption of radiation forming hydrogen radicals from water vapor [Marsh et al., 2001]. This is a nighttime effect only. The maximum ozone mixing ratio is about 3.5 ppmv, whereas under normal conditions it drops below 1 ppmv.

The spatio-temporal behavior of the ozone-mixing ratio in the upper mesosphere/mesopause region under nearly polar night conditions is not completely understood or reproduced by models thus far. Based on our sophisticated 3D-model of the dynamics and chemistry of the middle atmosphere (0-150 km) particularly designed to investigate the extended mesopause region, the spatio-temporal structure of this phenomenon is examined and discussed in terms of its chemistry. The most marked feature, reproduced by our model, is a pronounced ozone maximum around 70 km, also called the tertiary ozone maximum, and a strong drop of the mixing ratios around 80 km. The first feature was found by means of ground-based microwave measurements at mean latitude at Lindau (51.66° N) and high latitude at ALOMAR (69.29° N) during the night in the winter season. It was, however, absent during the daytime hours. The calculations by our model brought evidence that the enhanced ozone values occur in a latitudinal band close to the polar night terminator. It is confined both to a height range of approximately 66 to 77 km and to a certain latitudinal range which changes with season according to the change of the polar night terminator. For constant latitude, two annual maxima of the ozone mixing ratio occur nearly symmetrically to winter solstice. The higher the latitude, the more distant these maxima appear. The theoretical analysis of this phenomenon also brought evidence that ozone is formed under nearly grazing incidence conditions of radiation. The radiation dissociating water vapor is absorbed almost completely. This leads to reduction of the formation of hydrogen radicals which destroy odd oxygen. However, some radiation is still producing atomic oxygen.

This atomic oxygen is converted into ozone during the short twilight periods close to the polar night terminator. The loss of the accumulated ozone takes place partly by the Chapman reactions of a pure odd oxygen system and partly by catalytic reactions. The radicals HO_x take part in this destruction of ozone. These HO_x radicals are formed due to $\text{O}(^1\text{D})$ oxidation of the even hydrogens H_2 and H_2O and a residual photolysis of H_2O . The $\text{O}(^1\text{D})$ oxidation becomes important because the ozone dissociation rate is only slightly reduced for grazing incidence conditions in that domain. Within the region of the strong ozone decrease, around 80 km, the chemistry is marked by a steady increase of atomic hydrogen, which entails a drop of ozone and HO_2 . The poleward directed meridional wind transports ozone into the area of the polar night darkness.

5.2 Results

Figure 5.1 calculated by COMMA-IAP displays a latitudinal-seasonal section of the midnight ozone-mixing ratio at 72 km. The figure demonstrates the location of the enhanced ozone values close to, but outside of, the polar night terminator. Increased ozone concentrations occur along arcs on both hemispheres during the winter season. The winter polar regions do not show an ozone enhancement. The maximum values exceed 4 ppmv but the average is below that value. The height of 72 km was chosen because the effect is most pronounced in the calculations at this height. The effect spreads into middle latitudes but has a relatively strong gradient toward the poles.

Figure 5.2 (model results) exhibits the altitude-season section of ozone at 67.5°N which is close to the ALOMAR latitude. The figure displays two relatively isolated regions of ozone enhancement around 72 km. The first one starts in September and reaches its largest values in the beginning of November. The second one finishes at the end of March and its maximum occurs in mid February. The winter solstice values are only slightly enhanced. At the upper part of the figure the so-called second ozone maximum in the mesopause region can be seen but is not permanently present. During the entire year the 80 km domain is characterized by the lowest mixing ratios. At the lower part of the figure, a clear annual variation occurs with maximum values during summer solstice. The tertiary ozone maximum has a height extension of approximately 5 km. The early winter peak (October-November) is located somewhat higher (about 2 km) than the late winter one (January-March). As can be inferred from figure 5.1, the

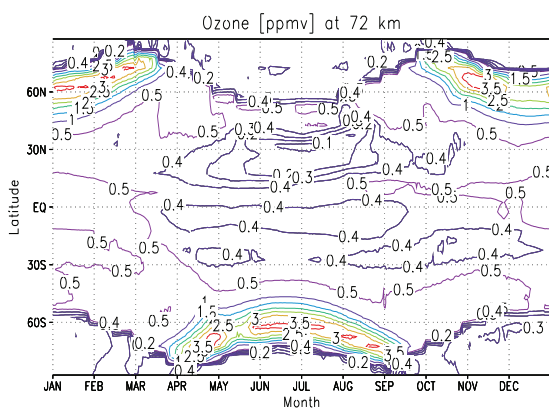


Figure 5.1. The midnight ozone mixing ratios [ppmv] depicted in a latitude-season section at 72 km altitude showing the arcs of the tertiary ozone maximum close to the polar night terminator.

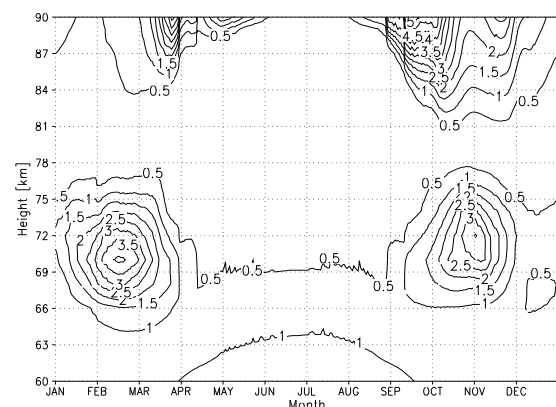


Figure 5.2. The altitude-season section of the ozone mixing ratio [ppmv] at 67.5°N .

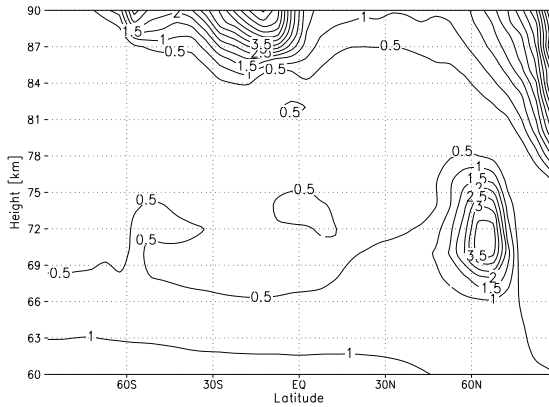


Figure 5.3. The altitude-latitude section of the ozone mixing ratio [ppmv] for November 10.

time difference between the early and late maximum grows with increasing latitude and the maxima coincide at about 60 degrees around the winter solstice.

Figure 5.3 shows the nighttime ozone distribution in an altitude-latitude section for November 10th. One can see the singular area of the tertiary ozone maximum around 60° N at 71 km. At the top of the figure the secondary ozone maximum is clearly to recognize. The maximum depends strongly on latitude and reflects dynamical patterns, particularly those of the vertical wind system. Downward directed wind transports atomic oxygen from the thermosphere

to heights below 100 km where it, owing to the increasing efficiency of the three-body reactions, will be transformed into ozone or will be recombined into molecular oxygen. This contributes to a remarkable increase of the chemical heating rate at that height. The secondary maximum of the absolute values, occurs at lower altitudes, and the daytime values are essentially smaller than those of the night. At the utmost latitudes in the mesopause region very large ozone concentrations occur. The cause is a downward transport of atomic oxygen within the polar vortex, which will again be transformed into ozone. The domain of enhanced polar ozone values finishes at about 75 km and it is clearly separated from the singular region of the tertiary ozone maximum by an area of very small values. This fact is evidence that the tertiary ozone maximum is not a result from any transport but has to be explained in terms of local chemistry. In contrast to the result presented here, the calculation published by Marsh et al. [2001] exhibits a deep “ozone hole” in the polar area. Also, the model by Summers et al. [1997] shows only slightly enhanced ozone values being a part of the globally extended secondary ozone maximum.

Figure 5.4 exhibits the nighttime ozone mixing ratios measured at ALOMAR in winter 1995/1996. These observations show a start of the development of the tertiary ozone maximum in the beginning of November and a finish approximately in April. There is, unfortunately, a gap of data after solstice but one can infer that the values are smaller around solstice. The distribution is strongly modulated by planetary scale oscillations, as it is known from the winter anomaly of the electron concentration of the D-layer. These oscillatory patterns make it difficult to determine the precise time of the strongest tertiary ozone layer, but the first maximum seems to occur at the end of November. The planetary wave activity also modulates the vertical winds and consequently the transport of minor constituents like NO. Atmospheric warming events are characterized by a reversal, or at least weakening, of the wind system. The possibility that the tertiary layer is due to a direct transport of odd oxygen from above can be ruled out as the band of small ozone values above the maximum precludes this. However, within this

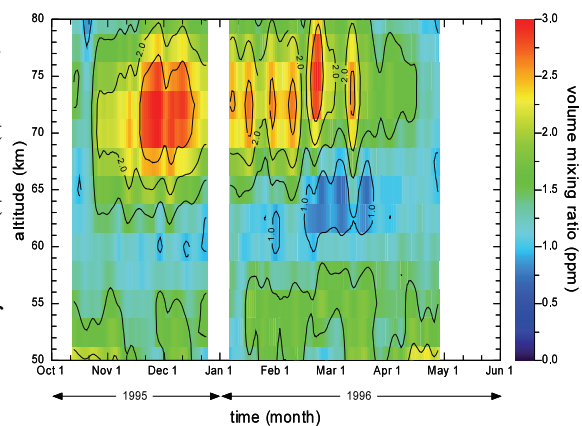


Figure 5.4. Annual variation of the nighttime average of the ozone mixing ratio at ALOMAR from October 1995 to April 1996 showing distinct maxima around 72 km altitude during the winter season.

region the atomic hydrogen concentration is sufficiently large that a vertical transport of hydrogen radicals could reduce ozone; this would mean that periods of relatively small ozone values are connected with periods of stronger downward directed vertical wind. Another possible explanation could be related to the fact that the O_2 -column density depends on temperature. The higher the temperature is, above a certain altitude, the greater is the column density. As will be discussed in the next section a large O_2 -column density favors ozone formation. Observations at Lindau provide evidence that enhanced wintertime ozone values extend to middle latitudes, albeit with decreasing amplitude. The maximum ozone mixing ratios are in the order of 3 ppmv at ALOMAR somewhat smaller than the model peak values of about 4 ppmv, although the observed data are smoothed and averaged over the night.

5.3 Discussion

The mesospheric ozone distribution is almost exclusively determined by a pure odd oxygen odd hydrogen chemistry. The hydrogen radicals H, OH, and HO_2 , the so-called odd hydrogen constituents, catalytically destroy the odd oxygen constituents O and O_3 marked by an odd number of oxygen atoms. The most efficient cycle consists of the reactions $O_3+H \rightarrow O_2+OH$ and $O+OH \rightarrow O_2+H$. Their net reaction is given by $O_3+O \rightarrow 2O_2$. The loss of the hydrogen radicals takes place through reactions of the hydrogen radicals themselves, and the efficiency of the loss depends on the composition of the radicals. The net source of both the primary odd hydrogen constituents H and OH and the primary odd oxygen constituent O is related to photolytic processes. At a constant altitude the values of the corresponding dissociation rates depend on the solar zenith angle.

The tertiary ozone maximum in the vicinity of the polar night terminator has been interpreted in terms of stronger absorption of radiation that dissociates water vapor than for the radiation that dissociates molecular oxygen [Marsh et al., 2001]. Molecular oxygen is almost the only absorber for radiation that dissociates both molecular oxygen and water vapor. Due to the large solar zenith angle near the polar night terminator, the column density of molecular oxygen along the transmission path of radiation is large. Below the mesopause, the dissociation rate of water vapor is mainly determined by the Lyman-alpha radiation due to a very large dissociation cross-section of it at the strong Lyman-alpha line. The cross-section at Lyman-alpha of the main absorber O_2 is three orders smaller. The dissociation rate of O_2 is with decreasing height increasingly determined by the radiation from the Schumann-Runge bands having a much smaller absorption cross-section than that at Lyman-alpha. As long as the Lyman-alpha radiation is not yet absorbed, the dissociation rate of H_2O decreases stronger than that of O_2 . The atomic oxygen production increases compared with the hydrogen radical formation. Thus, ozone formed from atomic oxygen increases under the conditions of increasing solar zenith angle. Figure 5.5 demonstrates this behavior. It displays the ratio of the relative water vapor dissociation rate to that of molecular oxygen at 72 km altitude depending on the solar zenith angle. The term “relative” means that for each zenith angle the dissociation rates at 72 km were divided by the dissociation rates for 0° . This ratio is unity for

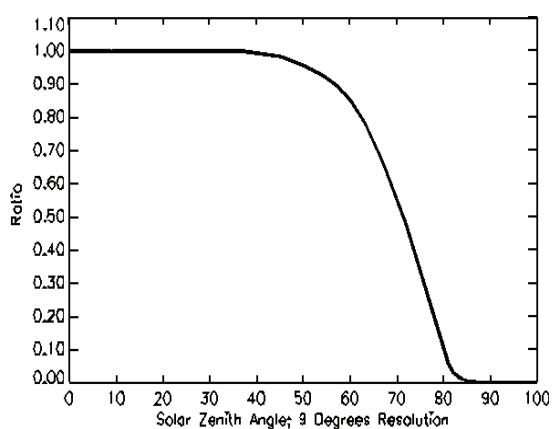


Figure 5.5. Ratio of the relative dissociation rates of water vapor to molecular oxygen.

0°, it approaches zero for high zenith angles, and is very small around grazing incidence angles (80°-90°). The ozone concentration would considerably increase if it would not be confined by the reaction with atomic oxygen. The dissociation rate of ozone is determined by radiation in the Hardley bands. The absorption cross-section of O₂ is extremely small for this wavelength range so that the radiation, dissociating ozone, decreases only due to absorption by ozone itself. In the upper mesosphere the ozone concentration is too small to get a noticeable absorption effect. This is why the radiation that dissociate ozone is nearly constant for solar zenith angles smaller than grazing incidence and begins to decrease only after 90° and is completely absorbed after 100°. In this case the radiation passes through lower altitudes where it penetrates layers of large ozone density. The dissociation of ozone forms O(¹D), which confines the ozone concentration both after quenching and reaction of O with O₃ and oxidation of H₂ and H₂O by O(¹D). This results in the formation of hydrogen radicals. The dissociation rates for angles around, and particularly after, sunset are not easy to calculate and the computation involves the danger of errors because the actual ozone distribution has to be taken into calculation and the O₂-column density depends on the current temperature profile. A common feature in calculation and observation is the band of small ozone values around 80 km. The altitude of this band declines toward the poles. It separates the secondary ozone maximum from the tertiary ozone maximum.

The secondary maximum results from the O₂-dissociation rate strongly increasing with height that determines the net production term for atomic oxygen and from a downward transport of atomic oxygen from the thermosphere. The secondary ozone maximum occurs during the night close to the absolute maximum of atomic oxygen that is located between 95 and 100 km. Simultaneously; a meridional transport toward north takes place within the polar winter vortex. Particularly, the vertical wind modulates the secondary ozone maximum. Above the maximum, the ozone production by the three-body reaction O+O₂+M → O₃+M becomes increasingly inefficient as it depends quadratically on the exponentially decreasing air density. During the night the ratio of concentration of atomic oxygen to concentration of atomic hydrogen determines the ozone concentration. As the atomic hydrogen concentration is essentially influenced by the advective and diffusive transports, the secondary ozone maximum is characterized by a large variability of altitude and concentration. The important reaction H+O₂+M → HO₂+M that converts atomic hydrogen into HO₂ also depends quadratically on the air density. This conversion is effective at the height of the tertiary ozone maximum (i.e.72 km), but not at 80 km. Atomic hydrogen and HO₂ are characterized by an opposite variation.

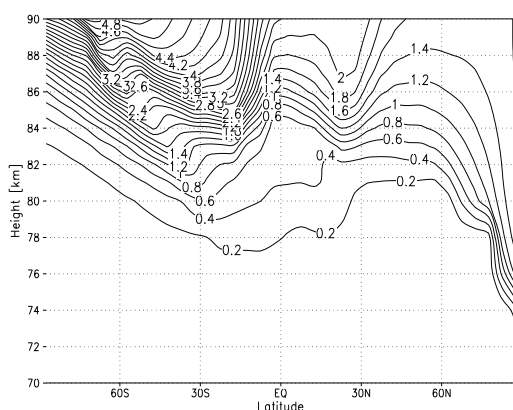


Figure 5.6. Altitude-latitude section of H [ppmv] at noon for the north winter solstice.

Figure 5.6 shows a height-latitude section of atomic hydrogen at noon for north winter solstice calculated by COMMA-IAP. Within the polar night area the H-concentration is large and downward transported. At the same time, H reduces ozone on the downward moving path. The levels of constant pressure are decreased in winter so that the conversion of H into HO₂ takes place more slowly at a constant geometric height relative to that in summer. The reaction of H with HO₂ suppresses the accumulation of this species. Figure 5.7 displays the same state of affairs as shown in figure 5.6 but for HO₂. The inverse behavior can be recognized. The partitioning

between the individual hydrogen radicals influences the efficiency of the odd oxygen destruction. The ozone destruction by H is more than two orders in magnitude more efficient than that by OH. There is a positive feedback in the way that a larger H-concentration decreases ozone and that reduces the formation of HO₂ according to the reaction OH+O₃ → HO₂+O₂. Hence, the most important hydrogen radical loss process - the reaction of H with HO₂ - is weakened. The calculations show a very complicated response of the CTM within the whole mesopause region. In comparison with measurements carried out at ALOMAR and Lindau the COMMA-IAP model reproduces the spatio-temporal behavior of the tertiary ozone maximum as a phenomenon occurring close to the polar night terminator and spreading into middle latitudes very well. However, the model is unable to create oscillatory variations with a planetary time scale. It does yield strong irregular variations on time scales of more than a month. A still unsolved problem in the model thus far seems to be the distribution of ozone within the very high latitude above 80 km during the polar night. Generally, the calculation of the downward transport of minor constituents within the wintertime polar vortex is an indicator of the quality of a model and CTM COMMA-IAP reproduces this feature well.

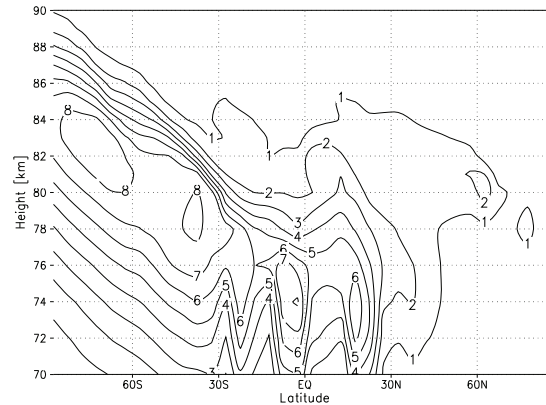


Figure 5.7. Altitude-latitude section of HO₂ [ppbv] at noon for the north winter solstice.

5.4 Conclusions

The reason for the formation of the tertiary ozone maximum around 72 km in the vicinity of the polar night terminator is the larger absorption cross section of water vapor for the Lyman-alpha radiation (being the source of the hydrogen radicals) than that of molecular oxygen. The absorption cross section of H₂O at the corresponding wavelength is about three orders of magnitude greater than that of O₂. As a result the radiation in the Schuman-Runge bands penetrates deeper into the mesosphere than the Lyman-alpha radiation. The Lyman-alpha radiation determines essentially the water vapor photolysis rate above 70 km for an overhead sun having unity optical depth of Lyman-alpha at about that height. This effect strengthens for increasing solar zenith angle. Consequently, the formation of the hydrogen radicals decomposing ozone is reduced whereas a small odd oxygen production still takes place from radiation in the Schumann-Runge bands and is responsible for the small accumulation of ozone in the vicinity of the polar night terminator. The chemical decomposition of ozone includes reactions with atomic oxygen (Chapman reactions) and with the residual hydrogen radicals formed by the reactions of H₂O and H₂ with O(¹D), which itself results from the dissociation of ozone, and a remaining photolysis of H₂O. At grazing incidence the dissociation rate of ozone is still nearly undiminished at the height of the tertiary ozone maximum so that, owing to the large ozone values, O(¹D) has comparably large concentrations. At around 80 km the situation is completely different. The small conversion of H into HO₂ due to the small air density results in large concentrations of H suppressing an accumulation of ozone there. The destruction of the odd oxygen compounds by the odd hydrogen species also depends on the composition of the odd hydrogens. A growth of H leads to a reduction of odd oxygen. The decline of ozone around 80 km is a separate effect but both the effects are connected by the dynamics. Comparing the

chemistry with the advective transport one will find that both influences are important in order to explain the whole phenomenon. The constituents are transported by the meridional wind from the area close to the polar night terminator into the polar night domain, sinking there and changing the efficiency of the chemical reactions at the same time. The complex interaction between dynamics and chemistry requires a solution within the framework of an advanced three-dimensional model employing an advective transport scheme characterized by very small numerical diffusion such as used here which is also able to consider the strong tidal winds correctly.

The impact of the enhanced ozone concentration on the aeronomic state seems to be small because all reactions slow down under condition of small radiation, meaning the response time of the system increases. However, ozone also determines the composition of the hydrogen radicals reducing atomic hydrogen. Perhaps large ozone concentration can cool the air a little locally by infra red emission like CO_2 . As the tertiary ozone maximum is a combined effect of chemistry and transport the simultaneous measurement of ozone and OH^* would provide information about the influence of the hydrogen chemistry on ozone. Generally, in order to evaluate the models, it would be very desirable to carry out continuous ozone measurements in the upper mesosphere/mesopause region within the polar night area.

Chapter 6

Non-linear Effects in MLT Region

6.1 General Discussion

As early as 1987, Sonnemann and Fichtelmann found that the photochemical system of the mesosphere represents a nonlinear enforced chemical oscillator driven by the diurnally periodic insolation. This system is able to produce chemical resonances if the characteristic chemical response time is in the order of one day. This is precisely true in the mesopause region. It was shown in the joint paper by Fichtelmann and Sonnemann [1987] that this system is able to create subharmonic oscillations of period-2 (here and after period- n means a period of n -days), period-3 and chaos depend on the period of insolation. Such phenomena are due to the nonlinear response of the system. The period of a subharmonic oscillation, in short subharmonics, is a multiple of the fundamental period amounting to a day, in case of the chemistry of the Earth's atmosphere, which is driven by the diurnally periodic solar insolation. In an ideal case for a period- n , every n day repeat the same diurnal variations for all constituents, whereas the diurnal variations of the individual days differ within this period of n days. For $n > 2$, a so-called deterministic chaos arises. More about deterministic chaos can be found in work of Schuster [1984]. As early as 1918 Duffing showed that such periodically driven nonlinear oscillators are able to create cascades of subharmonic oscillations. The current state of the art of findings regarding nonlinear processes in atmospheric photochemical systems was described, summarized and analyzed by Thompson and Stewart [1991] and Feigin [2002]. Abarbanel [1995] treated the problem of the analysis of observed chaotic data comprehensively and thoroughly. The same method applied to the atmospheric chemistry when considering observed chaotic time series has also been explored by Feigin et al. [2001]. Some theoretical investigations and methodical problems of the nonlinear response of the tropospheric photochemical system have been examined in publications by Krol and Poppe [1998] and Poppe [1999].

The highly idealized system of Sonnemann and Fichtelmann [1987], considering only the odd oxygen constituents O and O₃ and the odd hydrogen species H, OH and HO₂ as variable compounds (phase variables), was improved later. The behavior of this dynamic zero-dimensional model was systematically investigated using water vapor concentration, the ratio of daytime to nighttime hours (reflecting season and/or latitude) and air density (reflecting the geometric height) as control parameters [Fichtelmann and Sonnemann, 1992; Sonnemann and Fichtelmann, 1997]. Particularly, the paper by Sonnemann and Fichtelmann [1997] investigated the behavior from the point of view of chaos research. Yang and Brasseur [1994] showed that the photochemical system of the mesosphere has a trigger solution if fluxes from the

thermosphere into the mesosphere are taken into account. In the meantime, the group from Nizhny Novgorod further analyzed the nonlinear response of this system and derived the so-called essential model of the chemistry of the mesopause region [Konovalov et al., 1997; Feigin et al., 1998; Konovalov and Feigin, 2000; Feigin et al., 2001; Feigin, 2002]. They found that the effect, in essence, results from an interplay between atomic oxygen and atomic hydrogen. The nonlinear behavior of the system was further investigated by Montecinos [1996], Johnson et al. [1998], Montecinos and Felmer [1999] and Scott et al. [2000]. Montecinos and Felmer [1999] found that the period-2 is a stable oscillation of the photochemical system. They also reported on multiple solutions.

The control parameter “frequency of solar insolation” seems to be a trivial parameter for the Earth’s atmosphere, as the Earth’s rotation period of 24 h is constant. However, it was shown that the zonal wind moving an air parcel around a parallel results in a Doppler shift of the period of solar insolation [Sonnemann, 2001]. Under real conditions the shift of the period amounts to between +4 and -7 hours. On the basis of a simplified 1D-model considering a changing zonal wind only, the system again created subharmonics when the zonal wind exceeded a critical velocity. This so-called photochemical Doppler effect has been studied in more detail based on three-dimensional calculations, but a nonlinear response was not observed [Sonnemann and Grygalashvyly, 2003].

Kulikov and Feigin [2004] investigated reaction-diffusion waves in the mesospheric photochemical system caused by horizontal eddy diffusion. It was shown that when the spectrum of oscillation contains marked second subharmonics, reaction-diffusion waves in the form of traveling fronts and pulses of the phase of two-day oscillations may be excited.

The influence of turbulent diffusion on the nonlinear behavior was investigated by means of a one-dimensional model using the diffusion coefficient as a control parameter [Sonnemann and Feigin, 1999a and 1999b; Sonnemann et al., 1999]. A very complicated system response has been found. Different subtle and catastrophic so-called space-bifurcations, creating subharmonic and chaotic attractors, occur for a changing diffusion coefficient. The nonlinear response seems to be restricted to a certain height interval of upper mesosphere/mesopause, but actually the difference between the concentration amplitudes for consecutive days becomes smaller the more distant the height from this interval is. This behavior has been called the onion bifurcation. The most essential finding was, however, that strong diffusion suppresses the nonlinear response of the system. The critical values of the diffusion coefficient for the creation of a first subharmonic oscillation by a subtle bifurcation, a period-2 oscillation, ranges in the order of $K \sim 10^5 \text{ cm}^2/\text{s}$. This is comparable with real relations at the lower and middle mesopause region. As very small diffusion coefficient of the order of $K \sim 10^4 \text{ cm}^2/\text{s}$ have been frequently derived, particularly around and below 80 km [e.g. Lübken, 1997], the question arose whether a nonlinear response of the photochemical system can also occur under real conditions.

Although different hints to a subharmonic period in the mesosphere and mesopause region have been published, no direct evidence could be given for a chemically induced two-day oscillation thus far. Azeem et al. [2001] investigated mesospheric ozone and temperature data obtained by the Microwave Limb Sounder (MLS) on board the UARS and found two-day wave in ozone most pronounced near 30° latitude in the southern summer hemisphere in late January. The results seem to indicate that the two-day wave in the ozone is chemically driven in the mesosphere region via changes in reaction rates that are strongly temperature dependent. However, the authors could not investigate the mesopause region, and only discussed a region where a chemical two-day wave cannot be created.

The well-known phenomenon of the quasi two-day wave in the prevailing wind detected

by Doyle [1968], and later by Müller [1972], is commonly interpreted in terms of dynamic processes. The same dynamic explanation is given for the two-day variation in temperature [Wu et al., 1993]. The observation of a two-day variation in the oxygen green line volume emission rate, at a height where the characteristic time for atomic oxygen is too long to produce such an oscillation, was interpreted by an excitation from below [Ward et al., 1997].

The main goal of investigation discussed below is to give an evidence by modeling that the photochemical system of the upper mesosphere/mesopause region is able to respond in a nonlinear manner under certain conditions.

6.2 Mesopause Region

In the following some results of modeling will be shown which proof the existence of an intrinsic period-2 in the photochemical system of the mesopause region. The numerical experiment was carried out by calculations over 100 days with dynamical data and declination which does not change from one day to another one, in other words for a permanent repeated date for some selected dates of year as 1st July, 31st July, 1st January, 31st January, 22nd March and 22nd September. The calculations were started from precalculated with full annual cycle of the chemical distribution for each chosen date. After approximately one month of calculation the transients died away. The system then operates in an almost limit cycle mode. A limit-cycle on a plane or a two-dimensional manifold is a closed trajectory in phase space having the property that at least one other trajectory spirals into it either as time approaches infinity or as time approaches minus-infinity. Thus, if such calculations show subharmonic oscillations, it can be only the result of nonlinearity of the photochemical system, but cannot be dynamically induced. Some examples of these calculations which give an evidence of the existence for such oscillations are presented below. For these calculations the integration time step was reduced to 60 s and ozone and atomic oxygen were transported not in family, but separately. Only under these conditions the photochemical system created subharmonic oscillations.

Figure 6.1 shows a survey of calculations of the ozone mixing ratio for the northern hemisphere at 83 km altitude for a permanent 1st July. The ozone mixing ratios are indicative for other constituents because ozone is the best measurable constituent in the mesopause region. The figure clearly display a period-2 oscillation from about 33° N to 56° N. The largest amplitudes occur around 46° N. Around 37.5° N a weak period-4 occurs. Only the fundamental period-1 has been found on the southern hemisphere up to low northern latitudes. Figure 6.2 display an altitude-time section at 42.5° N of the same constituent. The figure shows that the two-day oscillation occurs approximately between 80 and 85 km with a maximum close to 83 km.

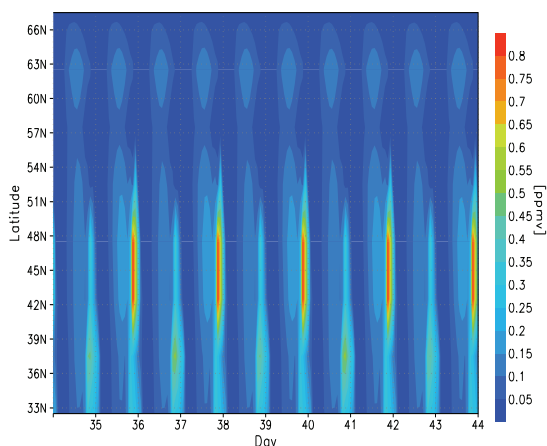


Figure 6.1. Ozone mixing ratio [ppmv] in northern hemisphere between 32.5° N and 67.5° at 83 km for repeated 1st July.

The calculations carried out for the south summer season do not simply result in a mirrored behavior. This finding result primarily from the dynamic model, which is based on the Berlin ozone climatology of the stratosphere being asymmetrical with respect to the hemispheres under comparable seasonal conditions and it is partly due to the eccentricity of the Earth's orbit [Pawson et al., 1998]. Figure 6.3 shows a cutout

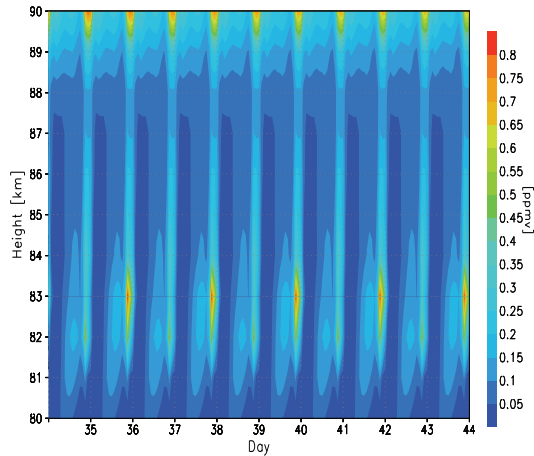


Figure 6.2. Altitude-time section of the ozone mixing ratio [ppmv] at 42.5° N according to the results presented in figure 6.1.

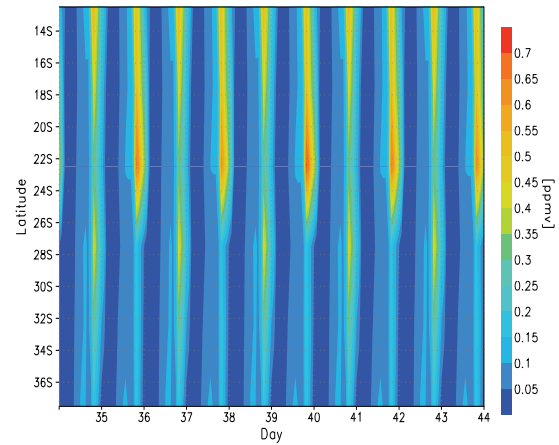


Figure 6.3. Ozone mixing ratio [ppmv] between 37.5° S and 12.5° S at 83 km for repeated 22nd December.

between 14° S and 36° S of the ozone mixing ratio at 83 km for a permanent December 22nd. The effect occurs in the southern hemisphere in middle to low latitudes of the northern hemisphere for this date. The position of the regions of nonlinear response changes with date. Period-2 oscillations occur during the entire summer season. The figure displays clear period-2 oscillations however, with a phase shift between about 25° S and 26° S.

The period-2 is the preferred subharmonics, but as Figure 6.4 demonstrates the next period doubling can also be created by the model. The figure shows the diurnal variations of ozone at 2.5° N at 83 km height for a permanent July 31st after more than 40 days of calculation. The amplitude difference for the system in the same phase reaches 0.3 ppmv and occurs after sunset, when the dissociation of water vapor is reduced but dissociation of molecular oxygen still exists and is not significantly reduced compared with that of water vapor. In reality such amplitude differences are masked by the natural variability due to the dynamics and can be observed only in cases of not to large wind and eddy diffusion. Figure 6.5 shows an example at 83 km and 12.5° N for a permanent January 31st. The representation starts after the beginning of calculations with a permanent wind and declination from one day to the other one - that is called “permanent” date, and on this figure one can see the genesis of the system. The system

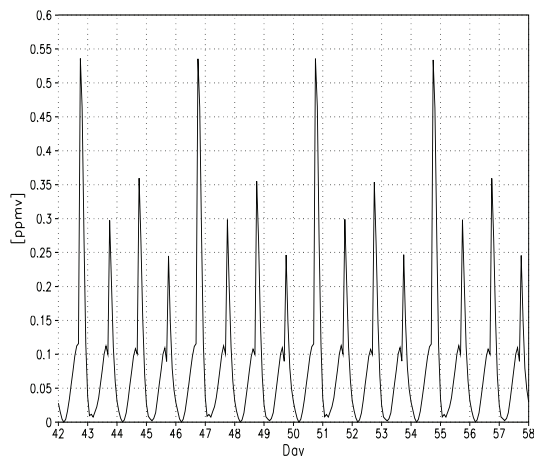


Figure 6.4. Diurnal variation of ozone mixing ratio [ppmv] at 2.5° N at 83 km for repeated 31st July.

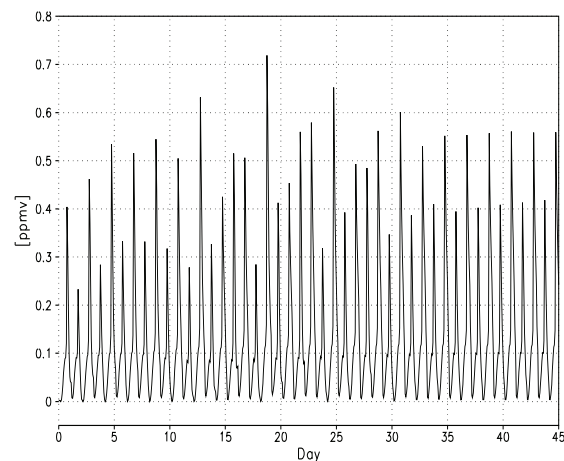


Figure 6.5. Diurnal variation of ozone mixing ratio [ppmv] at 83 km and 12.5° N for repeated January 31st.

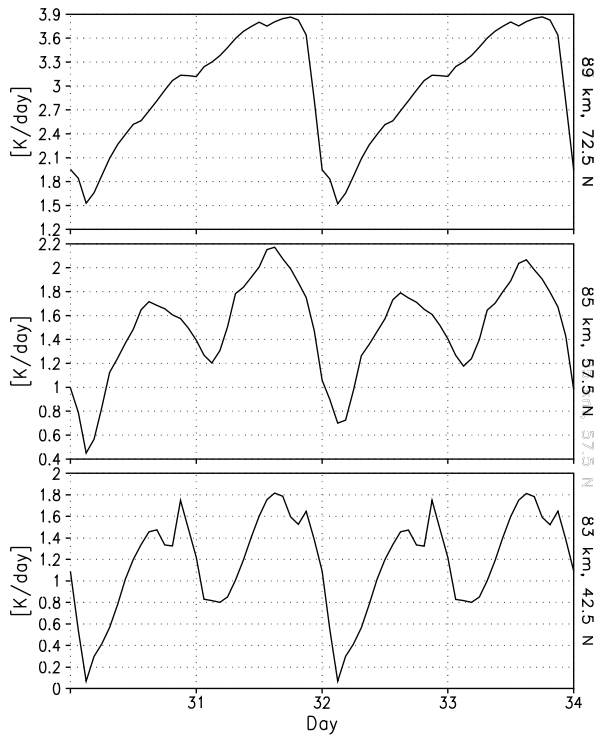


Figure 6.6. Diurnal variations of the total chemical heating rate for 4 consecutive days for an amplitude of 5 K/day [Forbes, 1982]. In a permanent July 1st at different latitudes and altitudes where it most pronounced.

responds immediately with the creation of a transient period-2 oscillation (days 1-12). After these 6 subharmonic periods a transient quasi period-6 occurs and then changes finally into a period-2 again approaching a limit cycle.

The chemical two-day oscillation induces a two-day oscillation of the chemical heating rate. Figure 6.6 depicts the diurnal and day-to-day variations of the total chemical heating rates for 4 consecutive days at different altitudes and latitudes for the July 1st. It is evident that the two-day oscillation of the individual species is connected with a marked thermal two-day variation of the chemical heating. As Figure 6.6 indicates, the pumping by chemical heating is a robust effect. The temperature amplitude of the chemical heating rate ranges in the order necessary to excite a certain two-day wave in the prevailing wind in the mesopause region but it is too small to

explain the full effect which needs minimum observations, maximum amplitudes of the prevailing wind components are usually attained at heights between 80 and 95 km [Craig et al., 1980; Ward et al., 1996] which correspond to the occurrence height of the nonlinear response. However, the two-day variations of the temperature or ozone have been found at the lower mesosphere but not only in the mesopause region [Wu et al., 1995; Azeem et al., 2000]. This could be caused by a different effect than that what creates a two-day wave in the mesopause region. The measurements of the prevailing wind indicates a maximum around 90 km altitude and only small values at 75-80 km [Harris, 1994; Palo and Avery, 1996; Thayaparan et al., 1997]. Unfortunately, our model is not interactively coupled. Therefore, it is not possible to say whether the chemical heating essentially feeds back to the dynamics, also influencing the vertical transport above and below the region of nonlinear response. Such transport could amplify the amplitude of the chemical heating rate due to a modulated transport of atomic oxygen, carrying almost only the latent chemical heat, as found by Ward et. al. [1997]. Actually relating to observations, it would be difficult to distinguish between dynamically induced or chemically caused quasi two-day variation (e.g. of measured ozone). The reason is that the amplitude of the chemical two-day oscillation between alternating days is not larger than would result from a temperature induced variation.

Another possible way of studying of the nonlinear system is the description of its behavior in the phase space. A trajectory describes the movement of a phase point within a phase subspace and an attractor reflects the motion in case of limit cycle. In the phase space the attractors are indicative for the nonlinear response of the system. Figures 6.7 and 6.8 display examples of quasi attractors for ozone versus atomic oxygen and ozone versus atomic hydrogen, respectively, at 83 km height and 42.5° N for a permanent July 1st. The data from calculations were stored every 1.5 h and therefore, the curves appear to be very angular. In reality they are

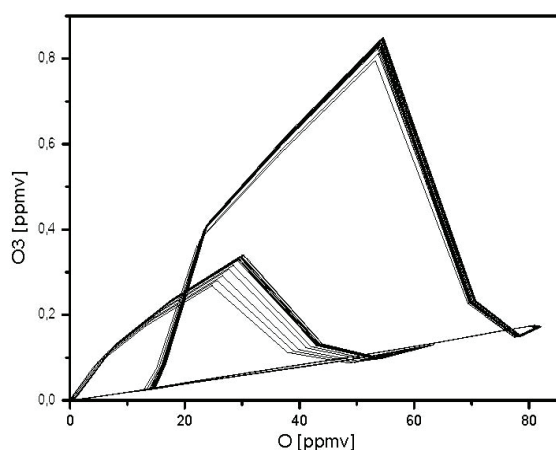


Figure 6.7. Quasi attractor in O_3 - O phase-space at 83 km and 42.5° N for a permanent 1st July.

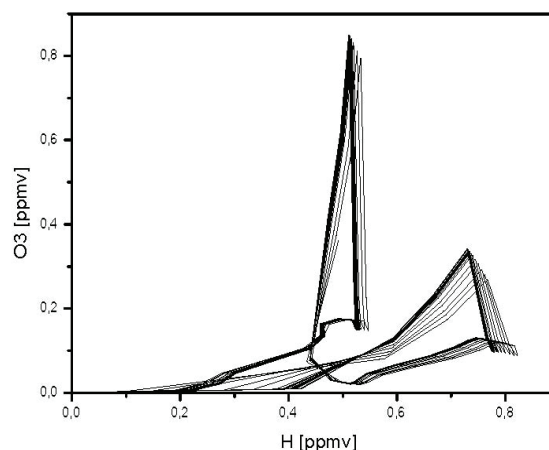


Figure 6.8. Quasi attractor in O_3 - H phase-space at 83 km and 42.5° N for a permanent 1st July.

smoothed. Although the calculations based on a permanent date the figures do not represent an ideal limit cycle because the long-living constituents still change slowly during the time period considered. Both of the different diurnal variations can be clearly recognized as separate loops.

The results presented here clearly show that a so-called “two-day wave” in the chemistry of the mesopause region can occur under favorable conditions but also that the two-day variation is not a general feature of the dynamics (totally independent of two-day waves induced by the dynamics because in the calculations only the dynamics for a certain day, which repeated each day of calculations, were used). In order to use certain conditions, the system was integrated under the conditions of a continuously repeating date. In reality, the conditions change slightly according to the running date. This concerns the slightly seasonally changing radiation conditions but it refers more to all influences connected with the changing dynamics. As in the climatological mean, the dynamic patterns do not normally change drastically within a period of one or two weeks. The creation of, at least, a transient period-2 oscillation is expected under real conditions in favorable locations. Figure 6.9 displays the diurnal variations of ozone at 83 km and 2.5° N under real conditions. There is a quasi period-2 which jumps into a period-4 and returns finally to a period-2. The amplitudes of the diurnal variations change permanently.

Water vapor concentration is an important chemical parameter, because it determines the behavior of the nonlinear photochemical system in the upper mesosphere/mesopause region, as it was shown in the paper of Yang and Brasseur [1994]. It was found that too dry (less than 1 ppmv) or too humid (larger than about 6 ppmv) atmosphere does not create a period-2. Also, the ratio of daytime to nighttime hours play an important role. In the case studied by Sonnemann and Fichtelmann [1997], the period-2 amplitude amplified with increasing daytime hours after a subtle start for about 2 daytime hours, but it decreased again after 14 daytime hours. The height range of the nonlinear response is shifted upward if the water vapor concentration increases. This may be a reason why at high latitudes this range is located higher because the humidity also increases toward the summer pole. Another fact that has to be considered is the increase of the level of constant air density in summer and the prolongation of the sunshine hours. In the mesopause region the water vapor concentration acts in the chemical system, above all, via the product $J_{H_2O}[H_2O]$ where J_{H_2O} stands for the dissociation rate of water vapor. During the years of high solar activity J_{H_2O} is about 50% larger in the mesopause region than during the years of minimum of solar activity. Although the water vapor concentration is reduced during the phase

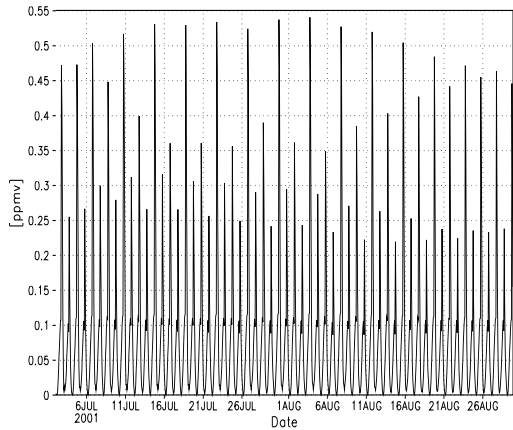


Figure 6.9. Diurnal variation of ozone mixing ratio at 83 km and 2.5° N calculated under real conditions.

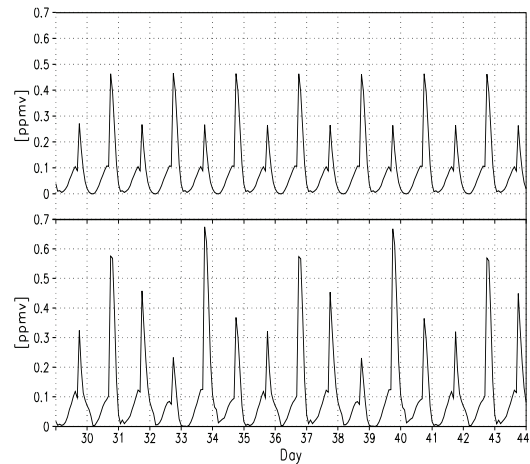


Figure 6.10. Comparison of the diurnal variations of ozone mixing ratio [ppmv] at 83 km altitude and 2.5° N latitude between high (upper panel) and low solar activity (lower panel) for a permanent July 1st.

of high solar activity due to enhanced photolysis, this effect does not compensate the increased dissociation rate, so that the product is larger than under mean conditions [Sonnemann and Grygalashvily, 2004]. A clear effect is the increase of the ozone concentration for decreasing solar activity due to the decrease of hydrogen radicals which destroy the odd oxygen constituents (ozone and atomic oxygen). Figure 6.10 shows a comparison of the diurnal variations of ozone at 83 km altitude and 2.5° N latitude between high (upper panel) and low solar activity (lower panel) for a permanent July 1st. In case of high solar activity a period-6 occurs that is doubling of a period-3. Fichtelmann and Sonnemann [1992] found that the period-3 is an inherent period of the chemical system of mesopause, also indicating that the system has the potential to respond chaotically. In other regions of nonlinear response, the period-2 oscillation is conserved with solar activity but the amplitudes of the oscillating species changes according to the solar activity.

6.3 Middle Mesospheric Ozone Oscillations at the Polar Day Terminator

The creation of subharmonic oscillations in the chemistry within the mesopause region could be a real effect in the atmosphere under favorable conditions of relatively low turbulent diffusion. The 1D-calculations by Sonnemann and Feigin [1999a] came to value of $K < 2 \cdot 10^5 \text{ cm}^2/\text{s}$, a not too strong vertical wind (<about 2 cm/s) and not too small water vapor mixing ratios (in calculations by means of simplified models mixing ratios had to be >1-2 ppmv) like those occurring in the summer hemisphere. But within the region of the polar mesospheric summer echoes and noctilucent clouds (PMSE-NLC region) at high latitudes in summer a freeze-drying takes place just at that height where the two-day oscillation can occur. Under this condition, the water vapor mixing ratio drops to a few tenths of a ppmv [Berger and von Zahn, 2002; Rapp, 2003]. The calculations using simplified models showed that these values of water vapor mixing ratio are too small to create a subharmonics [Sonnemann and Fichtelmann, 1997; Feigin et al., 1998]. Therefore, it is rather unlikely that the effect of subharmonic creation appears under the condition of freeze-drying. The model used did not consider a micro-physical code of ice particle genesis, thereby causing the freeze dry effect.

Figure 6.11 shows the same state of affairs as displayed Figure 6.2 at 72.5° N but outside

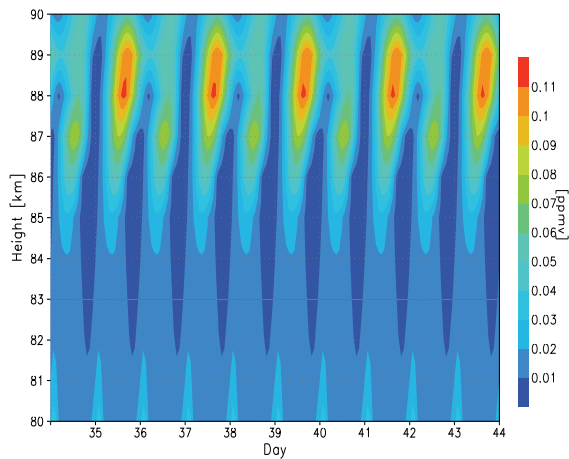


Figure 6.11. Altitude-time section at 72.5° N according to the results presented in Figure 6.1.

of the occurrence range of period-2 oscillation shown in Figure 6.1. There is practically no period-2 at 83 km but there is a pronounced two-day oscillation between 86 and 90 km with a maximum at 88-89 km. A phase jump occurs between 87 and 88 km. Generally in our model, the height region of the nonlinear response increases with increasing latitude but is strongest for the highest latitudes. The same calculations carried out for equinoxes does not yield a strong indication of a period-2 oscillation anywhere. Figure 6.12 displays the diurnal variations of the four most important chemically active species for a permanent July 1st. All constituents show clear two-day

variations of their mixing ratio.

The chemistry at the highest summery latitudes is not a subject of any nonlinear effects in our model. A two-day oscillation at 77.5° N was still found but not at 82.5° N. The main reason certainly consists in the fact that there is no, or only a very short night, meaning only a smoothed diurnal variation could drive the chemical oscillator [Sonnemann and Fichtelmann, 1997]. The photochemical system has an unequivocal solution for all sets of constant dissociation rates. As the system is a nonlinear radiatively driven chemical oscillator, it needs a radiative excitation for a clear day-to-night difference. Additionally, in winter the water vapor concentrations are too small to create a period-2 oscillation.

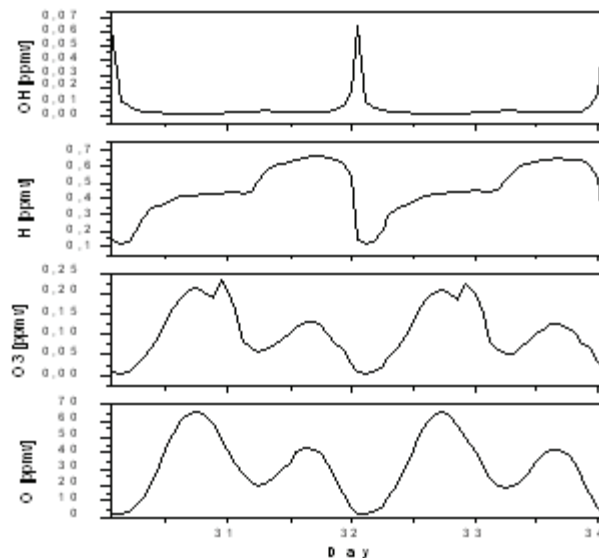


Figure 6.12. Diurnal variation of the four most important chemically active species for four consecutive days at 84 km and 62.5° N for permanent July 1st.

6.4 Summary and Conclusions

Different measurements in the upper mesosphere/mesopause region revealed a periodicity of quasi two days, however, there is no direct observational evidence thus far for a period-2 oscillation caused by nonlinearity of the photochemical system.

The main goal of this chapter was to demonstrate that the chemical system in the mesopause region is able to create subharmonic oscillations under nearly realistic conditions. The global 3D-model of the dynamics and chemistry produces these phenomena within the mesopause region at certain latitudinal regions, particularly during the summer season under the condition of relatively weak vertical winds, not too strong turbulent diffusion, and not too small water vapor concentrations. The occurrence of transient subharmonics after a sudden change of a system parameter, such as turbulence, vertical wind velocity or humidity, seems to be possible. The two-day oscillation of the active chemical constituents entails a two-day variation of the chemical heating rate which in the real atmosphere feeds back to the dynamics. As our model does not operate interactively, this response cannot be calculated by means of the present model version. Therefore, the development of a model with full interactive coupling in which the chemical heating rate feeds back to the dynamics is a first priority.

Chapter 7

Influence of Sudden Stratospheric Warmings on the Mesopause Region

7.1 The Sudden Stratospheric Warming (SSW)

The phenomenon of sudden stratospheric warming (SSW) was discovered and described in 1952 by Scherhag. It consists of a sudden increase of temperature in the stratosphere for high and middle latitudes in winter during a time range of one or two weeks. The observations show that the warming first appears at high altitudes near mesopause region and then descends into the lower stratosphere with an expansion from the pole towards the middle latitudes. This phenomenon reaches its maximum intensity near 65° N latitude with temperature values increasing to about 60 K in the stratosphere [Schoeberl, 1978]. During the strongest events - the so-called major warmings - the zonal wind reverses from westerly to easterly [e.g. Labitzke, 1981]. The temperature change in the mesopause region and the mesosphere between about 65 and 85 km shows a significant anti-correlation with that in the stratosphere during the SSW. According to the definition of the World Meteorological Organization (WMO), a SSW happens when, at the 10-hPa level or below, an increase of the latitudinal mean temperature poleward from 60° N latitude and an associated circulation reversal occurs. Sudden stratospheric warmings are classified as major warmings, which are considered in this chapter, and minor warmings, which are not discussed here. In a minor warming, the increase of the temperature is not so significant and the zonal wind and the meridional temperature gradient in the stratosphere usually weaken but do not reverse. The average temperature difference at 10 hPa between maxima of major or minor warming and the undisturbed atmosphere is about 30 K. According to our present knowledge, the reasons for the phenomenon are planetary waves propagating from the equator to the pole and their ability to penetrate through the winter stratosphere [Charney and Drazin, 1961]. Planetary waves transport heat and momentum from mid-latitude into the polar region, passing through the winter tropopause and reaching the upper stratosphere where they dissipate and raise the temperature dramatically by a release of eddy heat. One can find a more comprehensive theoretical explanation of this phenomenon in the papers of Holton [1976], Schoeberl [1978] and McIntyre [1982] and in the model studies of Kouker and Brasseur [1986] and Tao [1994].

There are only few investigations dealing with the influence of SSWs on the chemistry in the mesosphere-lower thermosphere (MLT) region [Liu and Roble, 2002; Sigernes et al., 2003; Siskind et al., 2005]. The goal of this chapter is particularly to investigate the influence of SSWs

on the distribution of minor constituents within the mesosphere/mesopause region by means of global 3D-model of dynamics and chemistry.

7.2 Effects During SSW in the Extended Mesopause Region

Table 1.

<i>N</i>	reaction	reaction rate	heat [kcal / mole]
1.	$O + O_2 + M \rightarrow O_3 + M$	$k_1 = 6 \cdot 10^{-34} \left(\frac{300}{T}\right)^{23}$	- 25.47
2.	$O + O_3 \rightarrow O_2 + O_2$	$k_2 = 1.5 \cdot 10^{-11} e^{-\frac{2218}{T}}$	- 93.65
3.	$H + O_3 \rightarrow OH + O_2$	$k_3 = 1.4 \cdot 10^{-10} e^{-\frac{470}{T}}$	- 76.90
4.	$OH + O_3 \rightarrow O_2 + HO_2$	$k_4 = 1.6 \cdot 10^{-12} e^{-\frac{940}{T}}$	- 37.45
5.	$HO_2 + O_3 \rightarrow OH + 2O_2$	$k_5 = 1.1 \cdot 10^{-14} e^{-\frac{500}{T}}$	- 31.00
6.	$O + O + M \rightarrow O_2 + M$	$k_6 = 4.7 \cdot 10^{-33} \left(\frac{300}{T}\right)^2$	- 119.40
7.	$OH + O \rightarrow H + O_2$	$k_7 = 2.2 \cdot 10^{-11} e^{-\frac{120}{T}}$	- 16.77
8.	$HO_2 + O \rightarrow OH + O_2$	$k_8 = 3.0 \cdot 10^{-11} e^{-\frac{200}{T}}$	- 53.27
9.	$H + O_2 + M \rightarrow HO_2 + M$	$k_9 = 5.7 \cdot 10^{-32} \left(\frac{300}{T}\right)^{16}$	- 49.10

The COMMA-IAP model provides climatological means of all calculated atmospheric quantities. In order to investigate phenomena such as SSWs or the propagation of planetary waves the LIMA model was developed. In this study, the influence of the SSWs on the distribution of minor constituents within the mesosphere/mesopause region was investigated using the LIMA model. The dynamics and temperature changing with the occurrence of SSWs impact essentially the chemistry of the mesosphere-lower thermosphere (MLT) region. The dynamics triggers the transport of long-lived minor constituents such as water vapor in the mesosphere and atomic oxygen in the lower thermosphere. The temperature determines considerably the magnitude of the chemical reaction rates. Additionally, as shown in the paper of Sonnemann and Grygalashvyly [2003], the change of the zonal wind has a considerable influence on the composition of chemical active minor constituents. All these influences are more carefully discussed below.

Figure 7.1 shows the temperature dependence for the most important reaction rates for typical variation of temperature in the mesosphere/mesopause region during a SSW. The numbers of the reactions correspond to Table 1. K1 is the only reaction forming ozone. It increases with decreasing temperature. The most important reaction rate of ozone destruction, K3, decreases with decreasing temperature. The same (decrease with decreasing temperature) is

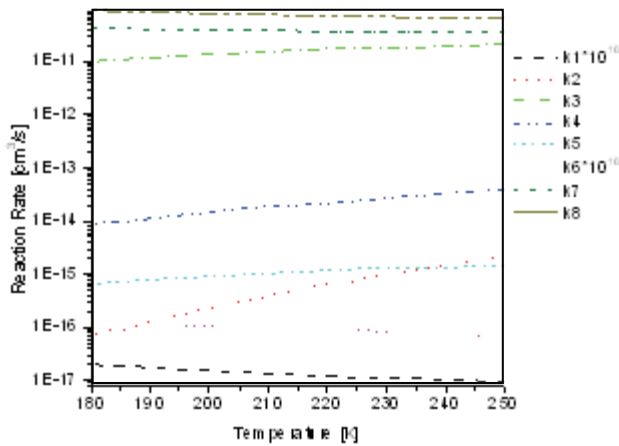


Figure 7.1. The reaction rates of most significant reactions for ozone loss/production in the mesosphere.

ozone increase under the condition of decreasing temperature. Figure 7.2 displays the annual variation of the temperature at 67.5° N in 2001 calculated by LIMA. The calculations reproduce two major warmings occurring in this time ranges: in the end of January/February and in the end of December. Additionally, there was a minor warming after the middle of the February. The sudden stratospheric warming starts in the mesosphere and reaches the lower stratosphere approximately two weeks later. The calculations show a maximum temperature increase in the stratosphere of 50 K larger than the value of the climatological mean. For both cases, the stratospheric warmings are connected with mesospheric cooling of about 30 K. These results are in agreement with measurements [Siskind et al., 2005].

Figures 7.3a-7.3d depict the diurnally averaged temperature, zonal, meridional, and vertical wind for the period January to April 2001 within the height region between 70 and 100 km. Figure 7.3a, when compared with Figure 7.2, demonstrates that the temperature decrease in the mesosphere/mesopause region starts approximately two weeks before (third quarter of January) the major SSW occurrence by definition of WMO (in year 2001 this is February 11), confirming observational findings [Siskind et al., 2005]. The zonal wind shown on Figure 7.3b

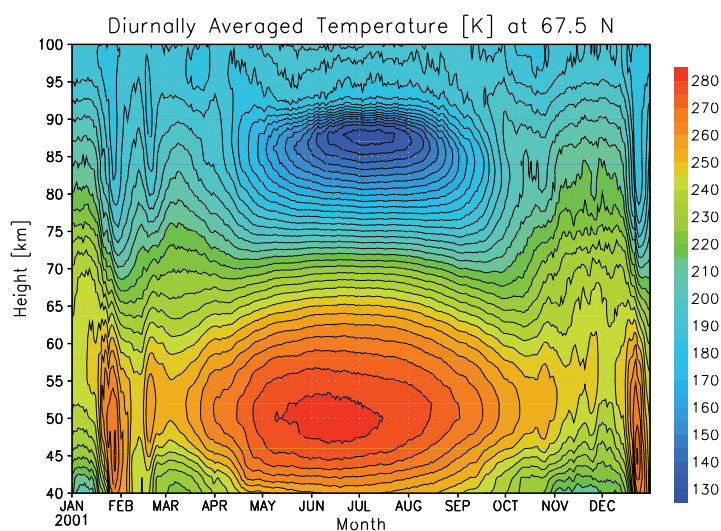


Figure 7.2. Annual diurnally averaged temperature at 67.5° N in year 2001 calculated by LIMA.

true for other reaction rates (K2, K4 and K5) that destroy ozone. Thus, both influences (increase of K1 and decrease of K2-K5) act to increase ozone when temperature decreases. However, the chemistry is more complex and one has to consider also the behavior of the other constituents involved in the ozone chemistry. This particularly concerns atomic oxygen being the source gas for ozone. The loss processes for atomic oxygen increases with decreasing temperature, which tends to reduce ozone. However, these influences are not so strong so that the enhanced atomic oxygen loss cannot compensate for the

tends to weaken and changes its direction at the time of minimum temperature. Figure 7.3c shows that the diurnally averaged meridional wind has its strongest positive values (toward the pole) just before the warming event and then rapidly reverses its direction. Figure 7.3d displays the vertical wind is marked by a quasi oscillatory behavior that is normally more pronounced at heights of 95-100 km. The vertical wind has a strong influence on the distribution of the minor constituents, because very large

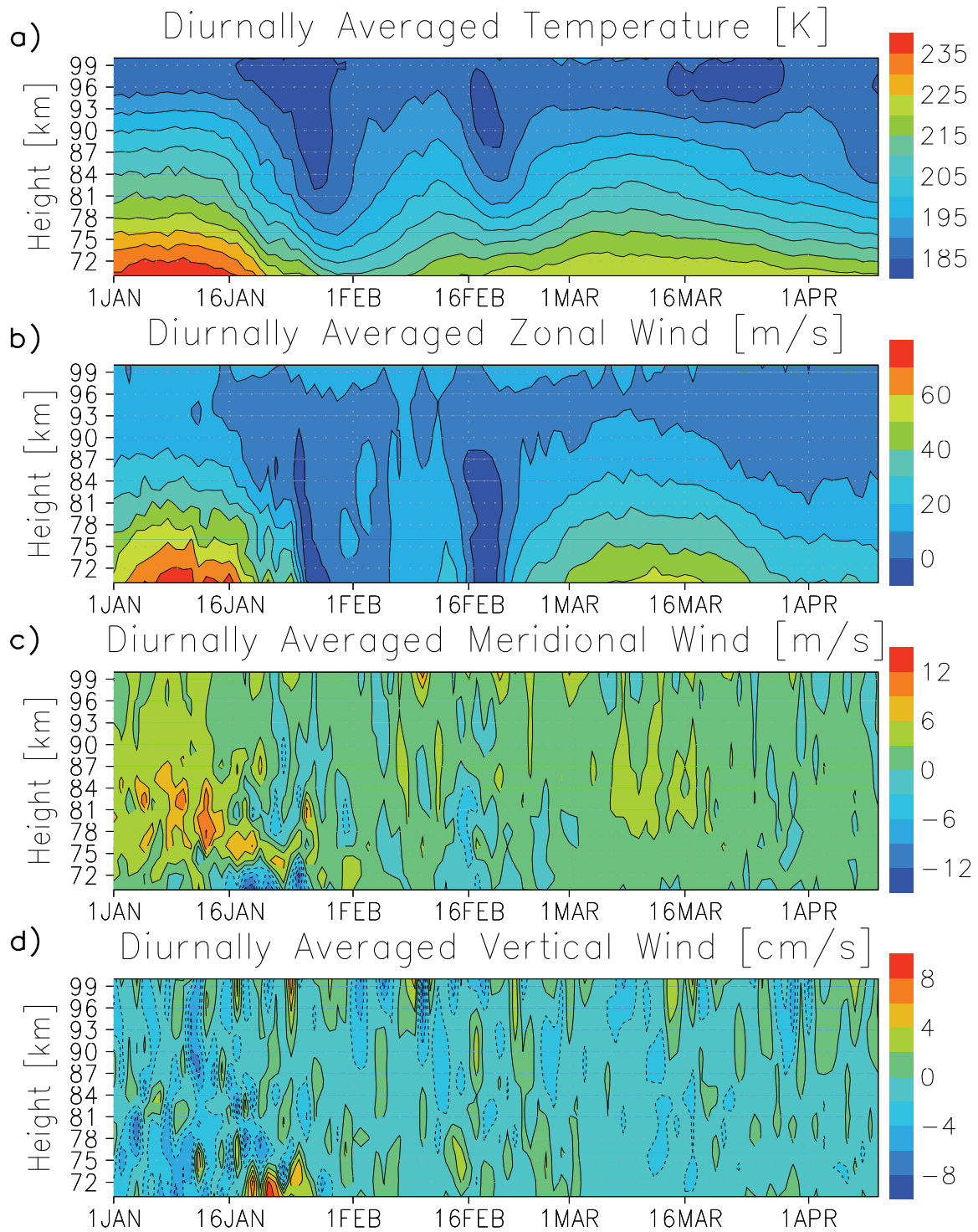


Figure 7.3 a-d. Diurnally averaged temperature (a), zonal wind (b), meridional wind (c) and vertical wind (d) at 67.5° N calculated by LIMA.

vertical gradients of the mixing ratios of different minor constituents such as water vapor, atomic oxygen, atomic hydrogen etc. occur in the upper mesosphere/lower thermosphere. The vertical wind modulates the distribution of minor constituents. Downward directed wind in the lower thermosphere conveys atomic oxygen into lower layers, raises the ozone concentration,

influences the distribution of the hydrogen radicals and increases the chemical heating rate. Atomic hydrogen is also transported, which determines the hydroxyl and hydroperoxy (HO₂) layers. But the changes in distribution of minor constituents in the mesosphere/lower thermosphere during SSWs which are shown and discussed below can not be explained by the influence of the vertical wind, because, as Figure 7.3d shows, there is no clear correlation between vertical wind and SSW like in the case of the zonal wind. Also the horizontal wind influences the distribution of long-lived minor constituents. Horizontal wind components are essentially stronger than the vertical component but the horizontal concentration gradients are usually much smaller. However, particularly in the vicinity of the polar night terminator marked by large meridional concentration gradients, the horizontal transport plays a considerable role. The impact of the zonal wind cannot be neglected as large concentration gradients of the chemically active families occur particularly during sunrise and sunset. The influence of the zonal wind on the chemistry of the MLT region has been investigated by Sonnemann [2001], Sonnemann and Grygalashvily [2003]. They found that in the middle to upper mesosphere in winter the prevailing west wind regime enhances the nighttime concentration of ozone compared with the case of zero zonal wind. The zonal wind reversal during a SSW (Figure 7.3b) should reduce the nighttime ozone concentration but the decreasing temperature (Figure 7.3a) and changed meridional wind direction from southward to northward (Figure 7.3c) overcompensate this effect.

Figures 7.4 a-d exhibit the time variation of the most important minor constituents. Figure 7.4 a shows the diurnally averaged ozone mixing ratio around the height of the secondary ozone maximum. The diurnally averaged values are mainly determined by the large long-lasting nighttime values of ozone. There is generally an oscillatory behavior in the region of the secondary ozone maximum (85-100km). The largest values (up to 9 ppmv) occur shortly after the time of SSW, after the decrease of the temperature in the mesopause/upper mesosphere region during the end of January. In the period of temperature minimum itself even the ozone concentration is reduced. The amplitude of the concentration oscillations decreases after the event. In the altitude range 72-75 and high latitudes the tertiary ozone maximum coinciding with the SSW period (end of November -beginning of March) [Hartogh et al., 2004].

As Figure 7.4b demonstrates, the variation of the diurnally averaged absolute atomic oxygen concentration having maximum values as large as $1.8 \cdot 10^{12} \text{ cm}^{-3}$ correlates very well with that of ozone. The reason is that the ozone production term is mainly determined by atomic oxygen. Figure 7.4c shows the diurnally averaged water vapor mixing ratio. It also reveals some oscillations which are induced by winds. During the SSW-period the mixing ratios are weakly enhanced but in the period of large odd oxygen concentration they are slightly reduced [Sonnemann et al., 2006]. Figure 7.4d exhibits the diurnally averaged atomic hydrogen mixing ratio. There is a clear anticorrelation to the variations of the odd oxygen constituents (see Figures 7.4a and 7.4b) with an exception of the March/April period.

Figure 7.5a shows the so-called nighttime tertiary ozone maximum around 70 to 74 km having mixing ratios up to 3 ppmv [Hartogh et al., 2004]. The Figures 7.5b -7.5d show the dynamical parameters: temperature, zonal and meridional wind during midnight, respectively. Comparing Figures 7.5b with 7.5a, it becomes clear that the time ranges of large ozone concentrations correspond to that of low temperature. Figure 7.5c makes clear that the zonal wind changes to summer conditions (negative values of an east wind system) during the period of SSW. The meridional wind (Figure 7.5d) also changes to summer conditions (blowing toward the south) with a certain time delay for the first SSW.

The vertical wind modulates the time behavior of all constituents by the vertical transport

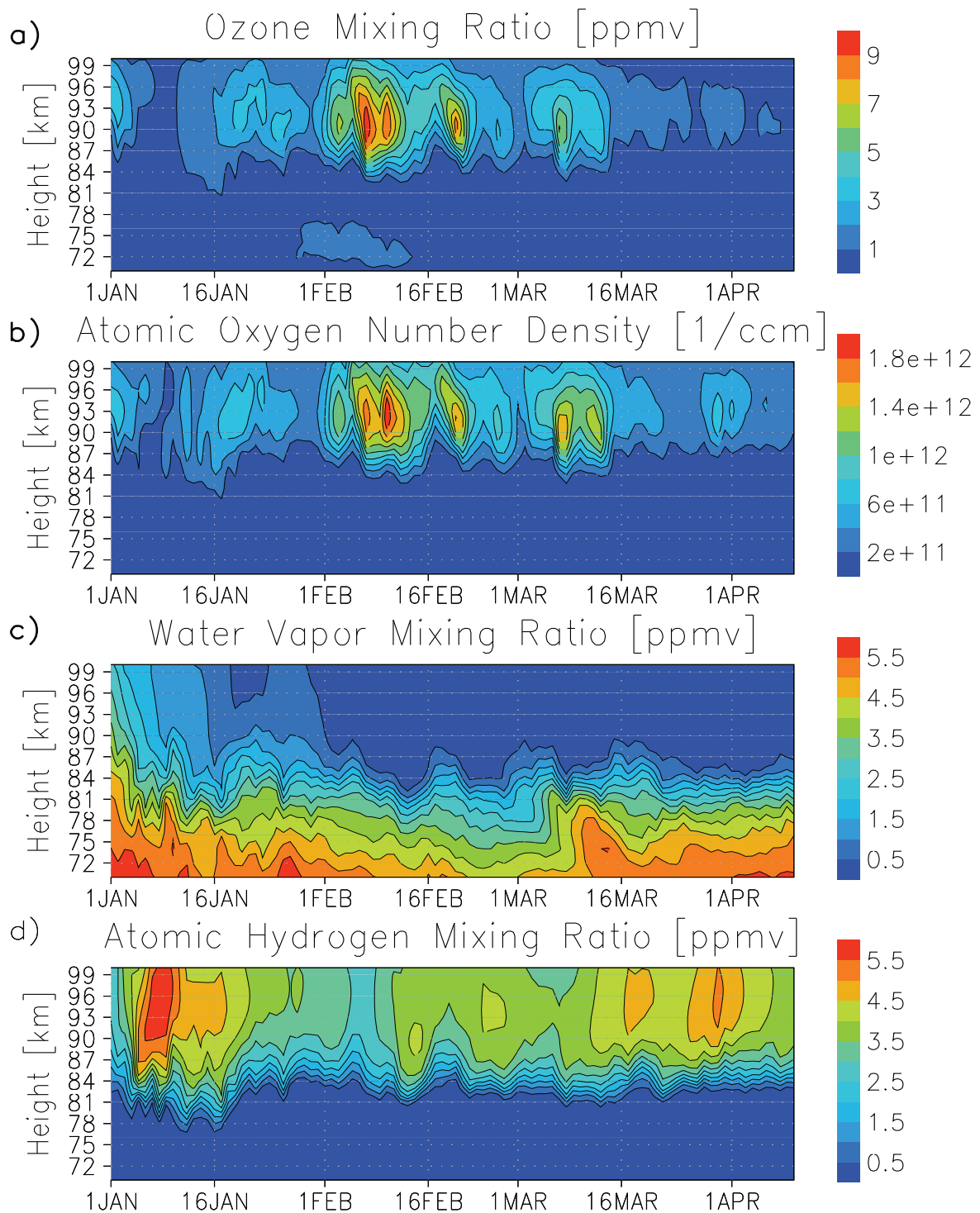


Figure 7.4 a-d. Diurnally averaged chemical constituents at 67.5° N, calculated by LIMA.

of long-lived constituents but its impact is rather different at various altitudes. In order to check the influence of the vertical wind on the distribution of any constituent one has to compare the characteristic vertical transport time with the corresponding characteristic chemical time of a family or a long-lived constituent. The downward directed vertical wind transports atomic oxygen from the lower thermosphere to regions where it will be converted into ozone by the

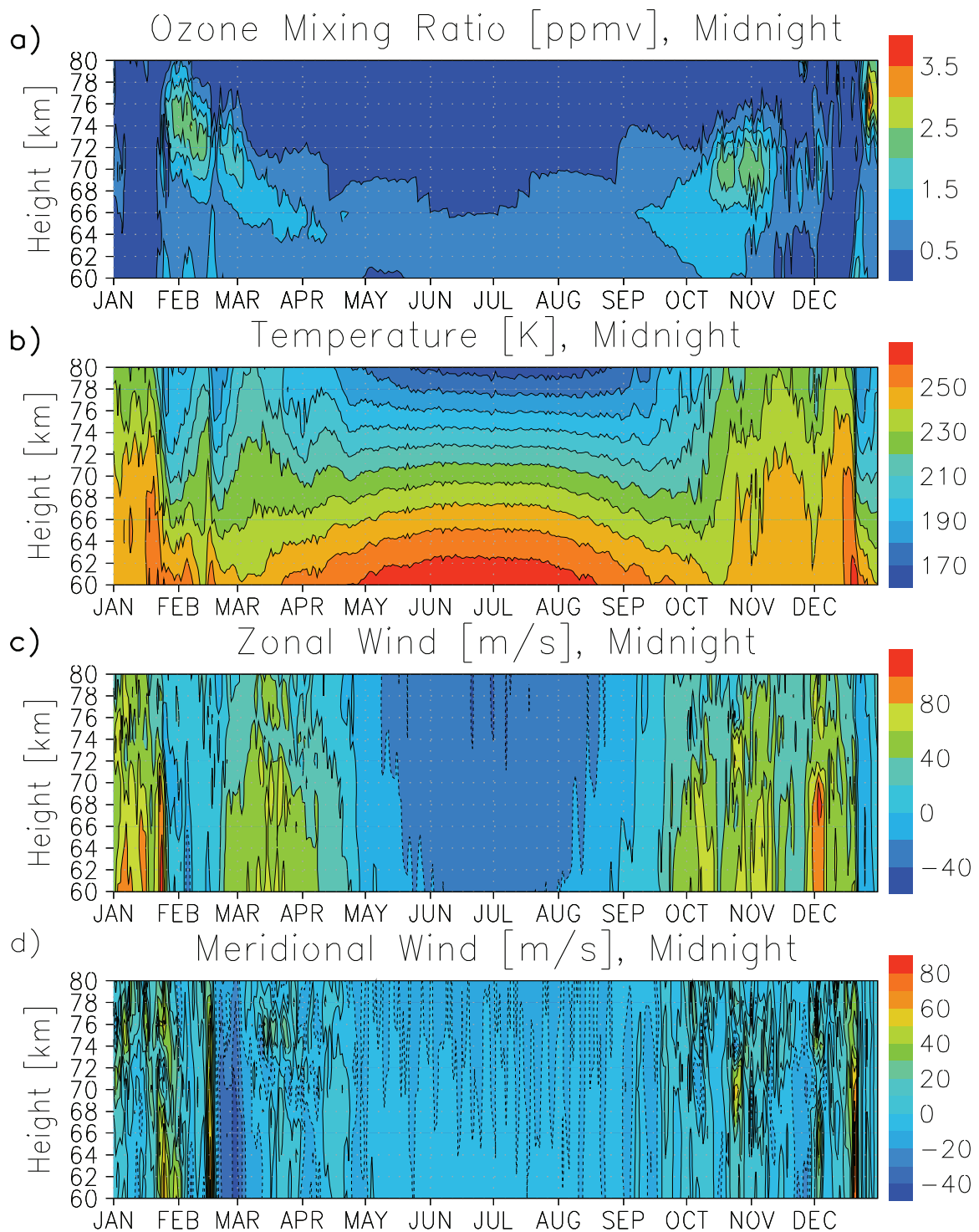


Figure 7.5 a-d. Ozone (a), temperature (b), zonal (c) and meridional(d) winds at 67.5° N, midnight, calculated by LIMA.

reaction K1. The characteristic time of this process depends quadratically on the air density, meaning the process is very slow (from a few days up to several weeks) within the mesopause region and above. Thus, atomic oxygen reveal only a slight diurnal variation above the mesopause at the height of the secondary ozone maximum. In contrast, the ozone loss during

daytime is a fast process with a characteristic time of about 100 s. During the night atomic hydrogen determines the characteristic time of ozone. Taking into consideration the large reaction rate K3 and the absolute largest atomic hydrogen densities around the mesopause the nighttime destruction of ozone is still a relatively fast process (several hours to a day). However, the destruction depends on the rather variable atomic hydrogen concentration that is also determined by vertical transport. Hence, there is a clear anticorrelation between nighttime ozone and atomic hydrogen. The OH*-airglow layer depends on both these oppositely varying constituents and the reaction rate depends only slightly on the temperature. The main source of atomic hydrogen at the height of the airglow layer is water vapor that depends strongly on the vertical upward transport. However, the vertical wind is not characterized by a uniform (summery) upward motion during the SSW event. Therefore, the maximum concentration of OH* during the SSW is a result of the large ozone values overcompensating for the atomic hydrogen minimum.

Figures 7.6a-7.6c display the layers of the diurnally averaged hydroperoxy radical, and the production rate of the excited states of hydroxyl radical and the hydroxyl, respectively. The OH*-layer corresponding to the layer of the Meinel band airglow lies approximately 5 km higher than the OH-layer. During the SSW the layers tend to become thinner and the altitudes increase by about 4-5 km compared to their height before the SSW occurred. Figure 7.6d shows the influence of the SSW on the chemical heating rate. Evidently, the chemical heating rate increases significantly after the time of SSW. This behavior could be expected as atomic oxygen, being the most important constituent for the chemical heating rate, also strongly increases after the SSW event.

Figures 7.7a-7.7d show the diurnal variations of ozone and hydroxyl before and during the time of SSW. The date before the event is January 13th, when the temperature was not yet decreased, and the date of SSW is January 28th, when the temperature of the mesopause was minimum. In the time of SSW, the secondary maximum of ozone during the night is essentially more pronounced in the whole domain (with exception between 80 and 85 km) than before the event occurred. During the daytime, the behavior is inverse but the diurnally mean behavior is determined by the large nighttime values of ozone with absolute maximum mixing ratios up to 4.8 ppmv at 92 km. The altitude of the secondary ozone maximum is decreased during the SSW by 4 km. In addition, the tertiary ozone maximum with maximum values of more than 2 ppmv around 72 km is clearly developed on January 28th whereas before the SSW there is no indication of enhanced ozone concentration. Likewise, the diurnal variation of hydroxyl changes strongly in the time of SSW. The mixing ratios of OH increase by a factor of 2 and the altitude of the layer rises by 4-6 km. The shape of the hydroxyl layer becomes full-blown and thinner whereas the nighttime increase of OH starts later.

At the time of SSWs the chemical system of the mesopause/upper mesosphere, which is well described by the odd oxygen-odd hydrogen chemistry, is driven from equilibrium state by the drastic changes of temperature and wind regime. This is one of the reasons for the ozone oscillatory behavior. Another reason is vertical wind oscillation. The vertical wind delivers atomic oxygen from the low thermosphere into regions where it is converted into ozone by the reaction K1. At the same time, the reaction rates for ozone destruction K2-K5 tend to go down with decreasing temperature. The increasing reaction rate K1 with the decreasing temperature and the inverse behavior of K2-K5 in the mesopause region during a SSW both lead to rising ozone concentration. Secondly, a more significant reason for the ozone increase during a SSW is the wind structure. Before a SSW occurs, when the meridional wind strongly blows poleward, odd oxygen (where it is comparably stronger produced by the photodissociation of molecular oxygen) is transported from mean latitude into the polar night region. In the polar night region, the atomic

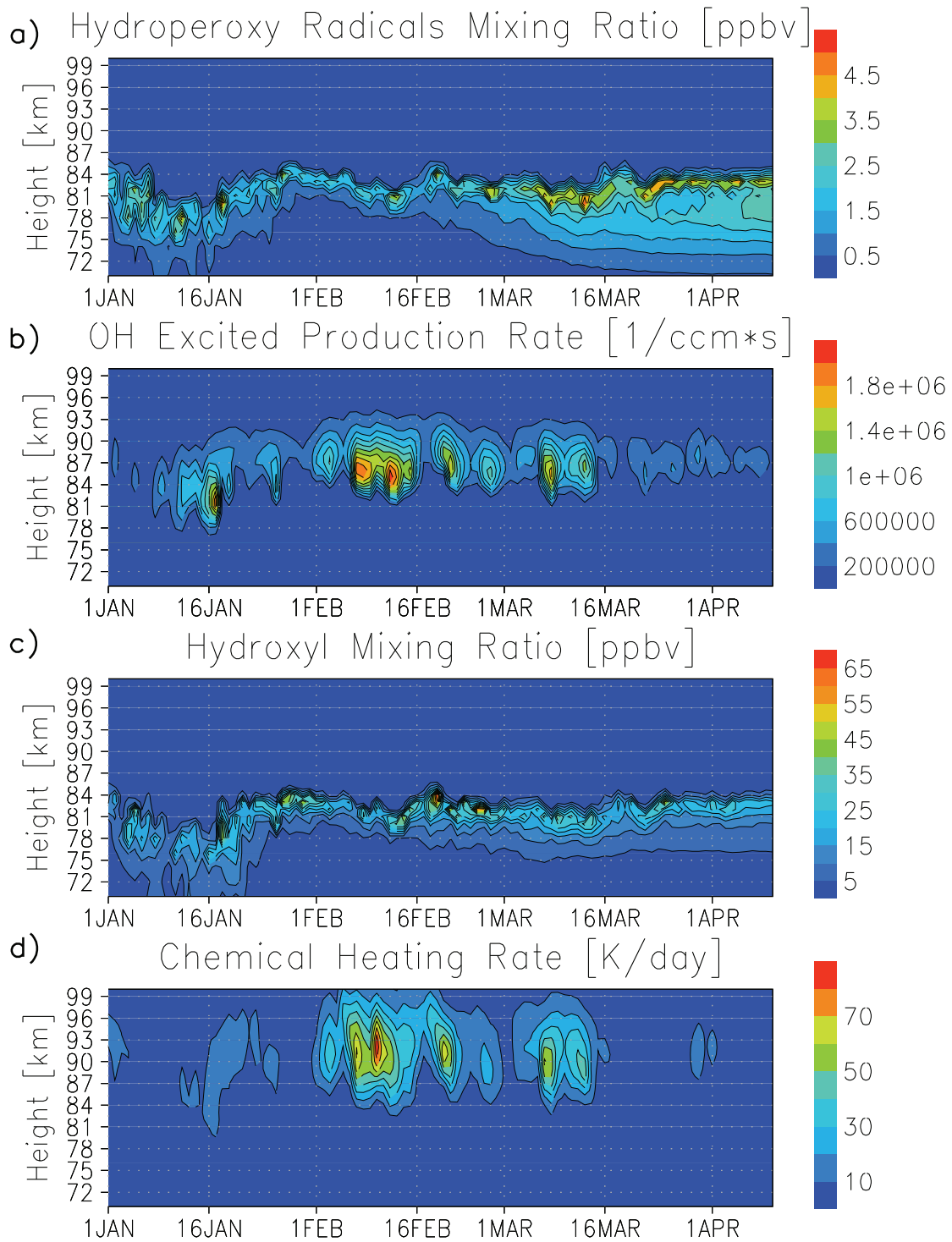


Figure 7.6 a-d. Diurnally averaged hydroperoxy radical (a), the production rate of the excited states of hydroxyl radical (b), the hydroxyl (c) and chemical heating rate (d) at 67.5° N, calculated by LIMA.

oxygen accumulates and converts to ozone and is then transported equatorward when the meridional wind changes its direction. The constituents of the odd hydrogen family play a significant role in the ozone destruction in the mesopause region. They destroy ozone by the

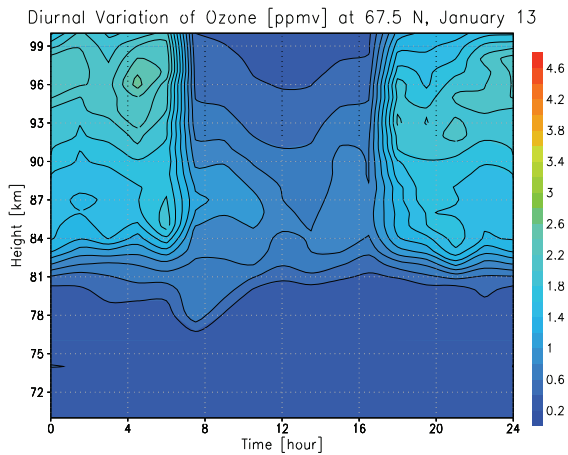


Figure 7.7a. Diurnal variation of ozone at 67.5° N before SSW (13 January), calculated by LIMA.

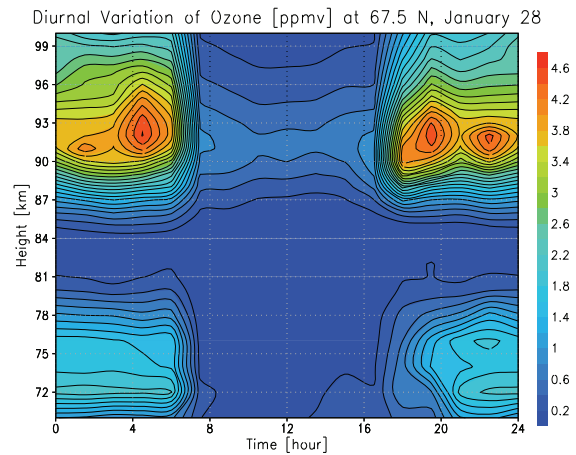


Figure 7.7b. Diurnal variation of ozone at 67.5° N in time of SSW (28 January), calculated by LIMA.

reactions K3-K5, which are strongest with atomic hydrogen according to the large reaction rate of 10^{-11} cm³/s and the highest amount of the atomic hydrogen compared to the other odd-hydrogen constituents. The mixing ratios of the ozone and atomic hydrogen are anticorrelated because of the reaction K3. The main source of the odd hydrogen constituents in mesopause is the water vapor photodissociation. Water vapor slightly decreases toward the polar area beginning at mean latitudes. The strong downward wind in time of SSW could be the reason for the odd hydrogen compounds reduction. As a result the odd hydrogen diminution causes less destruction of the ozone. This is a third reason for the ozone increase.

The tertiary ozone maximum was measured by means of the microwave technique at ALOMAR and Lindau. The observations were compared with calculations and described by Hartogh et al., [2004]. The existence of the tertiary ozone maximum during SSW can be explained by the same arguments as the secondary ozone maximum: by the temperature decrease and dynamical influences. At the altitudes of 68-78 km, within the period of tertiary ozone maximum, zonal wind becomes close to zero or changes its direction. This intensifies the effect of occurrence of a tertiary ozone maximum due to zonal wind effect on the photochemistry (ZWEPC) [Sonnemann, 2001; Sonnemann et al., 2003].

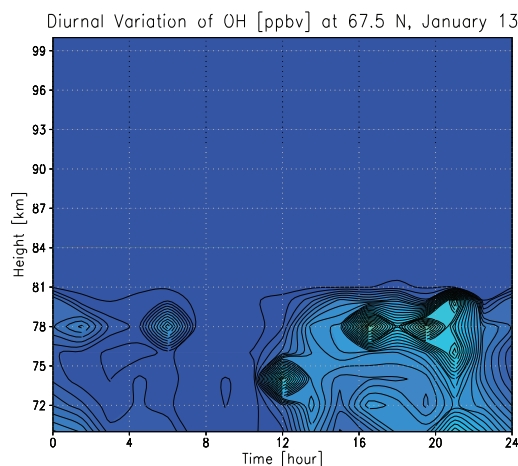


Figure 7.7c. Diurnal variation of hydroxyl at 67.5° N before SSW (13 January), calculated by LIMA.

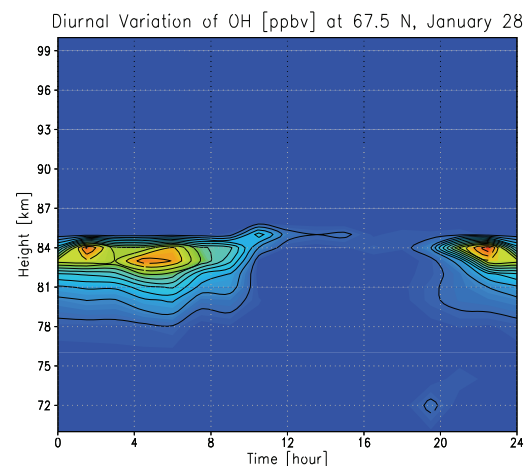


Figure 7.7d. Diurnal variation of hydroxyl at 67.5° N in time of SSW (28 January), calculated by LIMA.

As mentioned above, the net source of hydroxyl radicals in the mesopause/upper mesosphere is the photodissociation of water vapor, $\text{H}_2\text{O}+h\nu \rightarrow \text{H}+\text{OH}$. It is mainly formed by the reaction K3. The hydroperoxy radicals have the source reaction K4. The main loss terms of the hydroxyl and hydroperoxy radicals are determined by interaction with atomic oxygen in the reactions K7 and K8. The reactions with ozone (K4 and K5) play a minor role. One can see by comparison of Figures 7.6a,c with 7.4a,b that the shape of the upper border of hydroxyl and hydroperoxy radical layers mirrors the shape of the lower border of the atomic oxygen maximum and the secondary ozone maximum. The reactions with atomic oxygen (K7 and K8) are more significant for odd hydrogen destruction because of larger atomic oxygen number density and the reactions are about 4 orders in magnitude faster than K4 and K5. The increase of the reaction rates K7 and K8 with decreasing temperature determines the fact that the hydroxyl and hydroperoxy radical layers become thinner during SSW. The altitude of the layers increases and the thickness declines during the stratospheric warming due to interaction with enhanced values of the atomic oxygen concentration.

One of the damping mechanisms for the disturbed mesopause/mesosphere chemical system is the influence of chemical heat. Downward winds transport atomic oxygen recombining in the mesopause region contributing to the chemical heat which negatively feeds back to the downward wind. On the other hand, the latest measurements of temperature in the mesopause during SSW from SABER (Sounding of the Atmosphere with Broadband Emission Radiometry onboard the NASA TIMED satellite) show correlation of temperature gradients in the stratosphere below 1 hPa (approx. 48 km) and above 0.01 hPa (approx. 80 km) that can be caused by the strong chemical heating [Siskind et al., 2005].

The diurnal variations of the chemical constituents before the SSW and during a SSW are very different. Similar to ozone, the hydroxyl radicals night/day difference is more pronounced and values of absolute maximum are larger in time of warming. During SSW the secondary ozone maximum appears before sunrise (approx. 5 LT) and after sunset (approx. 19 LT) at the altitude 91-93 km. Comparably to the ozone behavior before the SSW, the absolute maximum of ozone during SSW is shifted down by four km due to stronger downward wind during SSW. The hydroxyl radicals maximum is shifted upward by 4 km because of the interaction with tertiary maximum of the ozone at its upper border.

7.3 Summary and Conclusions

During a SSW the mesopause/mesosphere temperature drops and the zonal wind changes its direction. The most important finding is an increase of the secondary and tertiary maximum of ozone due to the temperature decrease and change of the wind structure. The oscillations of the nighttime ozone maxima are caused by the change of the temperature and the dynamic patterns. The layers of the hydroxyl and hydroperoxy radicals become more narrow and their altitudes increase by four kilometers, caused by interaction with all active chemical species, and the Meinel band airglow layer becomes more intense. The chemical heating rate rises considerably in the model calculations. This effect results from downward transport of latent chemical heat by atomic oxygen from the lower thermosphere. The maximum of the chemical heating rate ranges some kilometers below of the atomic oxygen maximum. The mesopause chemistry is a so-called odd oxygen-odd hydrogen chemistry, where both chemical families interact with one another. In this case, the external disturbances have a strong influence on the mesopause chemical system. During the time of SSW, the changes of the wind and temperature regime play a role in such disturbances. The increasing mixing ratios of some of the minor

constituents leads to intensification of chemical interactions, resulting in the increase of chemical heat induced by the interactions. The chemical heat influences the temperature and the vertical wind with an opposite sign to the initial vertical wind and temperature at the beginning of SSW. In this manner, the chemical system of mesopause compensates with external forces and tends to be damped. The SSW phenomenon shows us an example of such behavior. Thus, LIMA gives an ability to study small scale effects which occurs during SSW.

Chapter 8

Other Results

8.1 Chemical Heating Rates

8.1.1 The Problem

The understanding of the energy budget in the MLT region is still very limited. There are several mechanisms by which the middle atmosphere is heated and cooled. Some fraction of the energy absorbed from the sun or generated by exothermic chemical reactions may be converted into the kinetic or potential energy of the molecules. The remaining fraction of the energy is converted into the internal energy of the molecules (exciting vibrational and rotational states). Two paths exist by which the energy is converted into heat. The excited molecules may be quenched by collisions or they may react chemically with other molecules. In this process the internal energy is ultimately converted to heat. The excited molecule can also lose its internal energy by spontaneous emission of radiation.

The importance of exothermic chemical reactions in heating the middle atmosphere has been noted by many researchers. A one-dimensional model considering the heat deposition of exothermic reactions in the mesopause region was developed by Crutzen [1971]. Further studies of chemical heating are from Brasseur and Offermann [1986], Mlynczak and Solomon [1991a], Mlynczak and Solomon [1991b], Mlynczak and Solomon [1993], and Meriwether and Mlynczak [1995]. The models used for the calculations of the heating rates in the papers of Garcia and Solomon [1983], Garcia and Solomon [1985], Mlynczak and Solomon [1993] are two-dimensional. The diurnal variations of the mixing ratios of the constituents that contribute to the chemical heating implicate a diurnal variation of the heating rate itself. Ozone especially has a strong diurnal variation at mesopause heights. Three-dimensional modeling is therefore desirable to get results including the diurnal variations. The first three-dimensional calculation of chemical heating rates was published by Sonnemann et al. [1997].

The most important quantity controlling the chemical heating rate is the concentration of atomic oxygen. The atomic oxygen concentration of the mesopause region is mainly influenced by O-fluxes from the thermosphere. The O-flux is completely controlled by vertical wind and eddy diffusion. Considering the model, due to the fast molecular diffusion, the thermospheric O-concentration will chiefly be determined by the arbitrarily fixed upper boundary values. The most important contributions to the chemical heating rates are listed in Table 1 of Chapter 7. Due to the quadratic dependence on O, the reaction N₆ strongly influences the chemical heating rate.

The second most important reaction in the mesopause region is the reaction N3. The reactions N2, 7-9 have only minor importance for the chemical heating rate.

The rate of conversion of chemical potential energy into other forms in a bimolecular reaction is given by

$$\frac{\partial Q}{\partial t} = k_r [R_1][R_2] \Delta E, \quad (8.1)$$

where k_r is the reaction rate, R_1 and R_2 are the reactant number densities, and E is the exothermicity of the reaction. The heating rate that would occur if the total exothermicity of reaction was converted into heat can be calculated from thermodynamical principles

$$\frac{\partial T}{\partial t} = \frac{2 k_r [R_1][R_2] \Delta E}{7 k_b M}, \quad (8.2)$$

where k_b is Boltzmann's constant and M is the total number density at a given altitude. The factor 2/7 arises from the relation between the specific heat capacity at constant pressure and the gas constant. For termolecular reactions, the heating rate is given by

$$\frac{\partial T}{\partial t} = \frac{2 k_r [R_1][R_2] \Delta E}{7 k_b}. \quad (8.3)$$

The chemical heating rate for the reaction N3 is reduced by Meinel band emission with 60% efficiency [Mlynczak and Solomon, 1993]. Some results of calculation are discussed below.

8.2 Results

Figures 8.1-8.3 depict the diurnally averaged chemical heating rates for spring equinox. Figure 8.1 represents the total rate and illustrates that the maxima of the total chemical heating

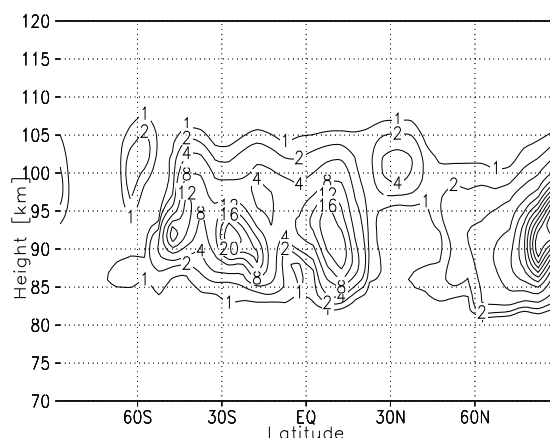


Figure 8.1. Diurnally averaged total chemical heating rate [K/day] for north spring equinox.

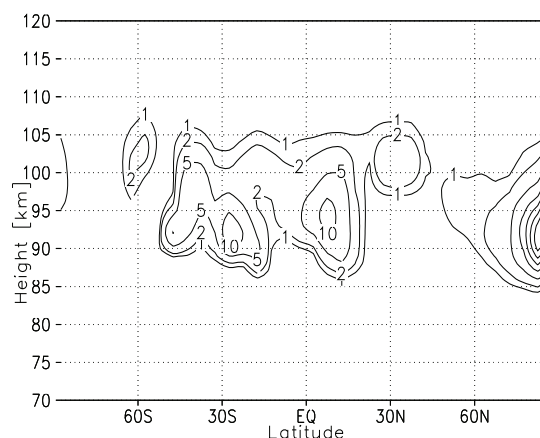


Figure 8.2. Diurnally averaged chemical heating rate [K/day] from reaction N6 for north spring equinox.

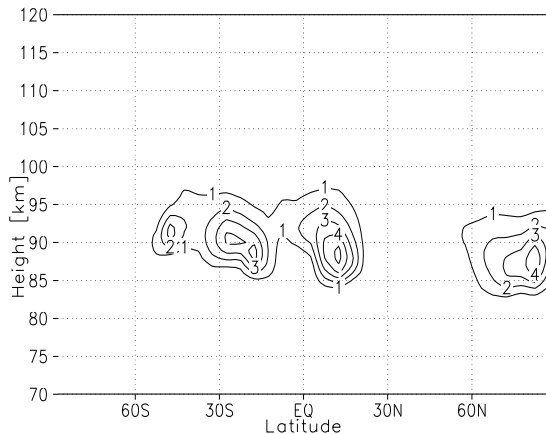


Figure 8.3. Diurnally averaged chemical heating rate [K/day] from reaction N3 for north spring equinox.

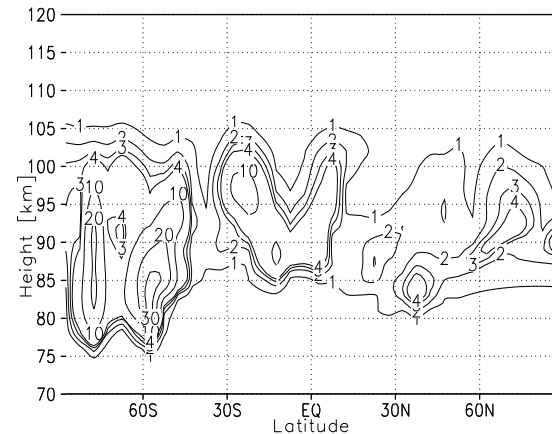


Figure 8.4. Diurnally averaged chemical heating rate [K/day] for north summer solstice.

rate lies close to the maximums of chemical heating rate due to atomic oxygen (Figure 8.2). Figures 8.2 and 8.3 correspond to the two most important reactions N6 and N3, respectively. The global absolute maximum is located near the equator. There is a region of strongly enhanced chemical heat at high latitudes in the spring hemisphere, due to reactions N3 and N6. The behavior of the chemical heating rate changes at solstice. Figure 8.4 shows diurnally averaged total chemical heating rates for summer solstice. Because of the long winter nights characterized by considerably enhanced ozone concentration, the diurnally averaged chemical heating rate rises for the reactions which contain ozone (N2-N5). Consequently, the winter values exceed those of the summer ones. There are descending winds in winter transporting atomic oxygen from the thermosphere into the mesopause region. Conversely, there are ascending winds in summer, which counteract such a transport of chemical energy. Ultimately, because of the global upper thermospheric meridional winds, the thermospheric atomic oxygen concentration is higher in winter than in summer. In general, the maximum of the total chemical heating rate varies from a few K/day up to more than 40 K/day locally in regions of strong downward transport of atomic oxygen. Results published by different groups show heating rates of the same order of magnitude as presented in this work [Brasseur and Offermann, 1986; Mlynczak and Solomon, 1991a; Mlynczak and Solomon, 1993; Riese et al., 1994]. The highest amounts of the chemical heating rate appear around 90 km. Chemical heating is an essential energy input into the 80-100 km region and is comparable to the other diabatic sources as, for example, breaking gravity waves. With regards to numerical modeling, interactive treatment of dynamics and chemistry will be necessary for more reliable representation of this process.

8.2 Computation of OH* and OH.

8.2.1 Introduction

The airglow measurements in the Meinel bands are widely used to obtain information about the temperature in the mesopause region and mesosphere [von Zahn et al., 1987; Offermann and Gerndt, 1990; She and Lowe, 1998] and the behavior of gravity waves [Tarasick and Shepherd, 1992; Makhlof et al., 1995]. The observation of hydroxyl can be applied for studying its long-term behavior. Measurements of the OH concentration can be used to derive

atomic oxygen concentration [Thomas, 1990; McDade and Llewellyn, 1987; Takahashi et al., 1996]. Near the mesopause, the concentration of ozone at night is determined by the balance between production by the reaction of atomic with molecular oxygen N1 and losses by reactions with atomic hydrogen N3:

$$[O_3] = \frac{k_1[O][O_2][M]}{k_3[H]} \quad (8.4)$$

The production rate for excited hydroxyl is:

$$P_{OH} = k_3[H][O_3] \quad (8.5)$$

Substituting (8.4) into (8.5), it is clear that the production rate of excited hydroxyl is proportional to the atomic oxygen concentration.

$$P_{OH} = k_1[O][O_2][M] \quad (8.6)$$

Russell and Lowe [2003] and Russell et al. [2005] used this relationship to derive a seasonal, global climatology of atomic oxygen from observations made by WINDII (Wind Imaging Interferometer) onboard UARS (Upper Atmosphere Research Satellite).

As the principal source of odd hydrogens (H, OH, HO₂ and H₂O₂) in the mesosphere and mesopause region is considered to be water vapor, the measurements and calculations of hydroxyl give us indirect information about water vapor. During the daytime we can derive an expression for water vapor as a function of hydroxyl, because odd oxygen (O and O₃) and odd hydrogen are in a flowing photochemical equilibrium during the daytime. Such expression would not be useful, because airglow measurements are possible only during the night, but odd oxygen and odd hydrogen are not in photochemical equilibrium during the night, as for both constituents the loss far exceeds the production. Thus, analytic expression for nighttime dependence of water vapor on hydroxyl cannot be derived. Nevertheless, retrieving the water vapor by airglow measurements in region 78-87 km is possible if assimilate this data in a semiempirical model, and for this case we need correct model of relaxation of excited hydroxyl for solution of the inverse problem.

Moreover, hydroxyl is a chemically active constituent that plays a significant role in chemical processes both within the mesosphere/mesopause region and in the autocatalytic water vapor formation [Sonnemann et al., 2005].

The main production of OH* is given by the reaction H+O₃ → OH*+O₂ in which vibrationally excited hydroxyl is produced and then relaxed by collisions and spontaneous emission forming OH. The principle loss of OH results from the reaction OH+O → H+O₂. The primary net source of the hydrogen radicals is the photolysis of water vapor as was mentioned above. Increasing water vapor concentrations entail an increase of hydrogen radicals in the MLT-region. However, this increase will be modulated by the change of odd oxygen. According to both mentioned reactions, the hydrogen radicals destroy the odd oxygen family. As both the production and the loss term are reduced by decreasing odd oxygen concentration, the OH concentration is not strongly affected by the decline of the odd oxygen concentration. This is not true in the same way for excited OH*, which is formed by the reaction of ozone with atomic hydrogen. As mentioned above the principle loss of OH* is quenching by collisions with air

molecules. Increasing H concentrations reduce O₃ so that both effects have the tendency to compensate changing humidity. OH* is responsible for the airglow emission in the infrared Meinel bands. Hydroxyl peroxide (HO₂) is closely coupled with the OH concentration. Its concentration is smaller than that of OH and it is chemically less important compared to OH. The main reaction of HO₂ production is given by OH+O₃ → HO₂+O₂, which is characterized by a relatively low reaction rate, whereas the principle loss HO₂+O → OH+O₂ is very effective. The smaller efficiency of production rate and higher efficiency of loss rate of HO₂ are the reasons for smaller values of HO₂ compared with those of OH.

8.2.2 Calculation of the Concentrations of OH* in the Different Excited States

In order to derive the expression for the calculation of excited hydroxyl at each vibrational level we assume that hydroxyl is in photochemical equilibrium at each vibrational level. Thus, we can calculate it as the ratio of production term to the loss term. In the production and loss terms we summarize contributions from the chemical reactions, contribution due to deactivation by quenching and due to spontaneous emission. The following expression includes all the processes that were taken into account in the model of relaxation:

$$[OH_v] = \frac{k_3(v)[O_3][H] + k_8(v)[HO_2][O] + p[OH_{v+1}][O] + q(v+1)[OH_{v+1}][N_2] + \sum_{\nu=v+1}^9 Q_{\nu\nu} [OH_\nu][O_2] + \sum_{\nu=v+1}^9 A_{\nu\nu} [OH_\nu]}{k_7(v)[O] + p[O] + q(v)[N_2] + \sum_{\nu=0}^{v-1} Q_{\nu\nu} [O_2] + \sum_{\nu=0}^{v-1} A_{\nu\nu}}, \quad (8.7)$$

where k_i are the reaction rates, v is the vibrational number, p , q , Q are the quenching rates for quenching by atomic oxygen, molecular nitrogen and molecular oxygen, respectively, and A are the Einstein-coefficients for spontaneous emission. The numerator shows the production terms for each vibrational number v and the denominator contains the loss terms. The first term in the numerator describes the main source of vibrationally excited hydroxyl, which is the reaction of atomic hydrogen with ozone. The dependence of the reaction rate on vibrational number $k_3(v) \propto f_v k_3$, where f_v is the nascent distribution. The nascent distribution published by Charters et al. [1971] has been extrapolated to lower vibrational numbers employing the information theory [Steinfeld et al., 1987] and then renormalized to the Einstein coefficients [Nelson et al., 1990]. This distribution populates the five highest vibrational levels, from level $v = 5$ (1%) to level $v = 9$ (47%). The second term in the numerator is the secondary source of vibrationally excited hydroxyl. The dependence of the reaction rate on the vibrational number is given by $k_8(v) \propto e_v k_8$, where e_v - is the nascent distribution [Makhlouf et. al., 1995]. The three lowest vibrational levels (40%) and the not excited level (60%) are populated by this distribution [Kaye, 1988]. The first term in the denominator of expression describes the chemical loss of OH_v by reactions with atomic oxygen. The reaction rates $k_7(v)$ depend on the vibrational number [Takahashi et. al., 1981]. The third term in the numerator and the second in the denominator describe the process of quenching by atomic oxygen. Unfortunately there is a lack of knowledge about the quenching rates for these reactions and their dependence on the vibrational number, thus they are taken as constant [Adler-Golden, 1997]. The second quencher is molecular nitrogen. For this quencher a "cascade" scheme (single-quantum relaxation) was applied [McDade and Llewellyn, 1987]. In this case, for all vibrational levels, excited molecules pass to the next lower vibrational level (OH_v+M → OH_{v-1}+M). The quenching rates $q(v)$ depend on the vibrational number

as described in [Makhlouf et.al., 1995].

As was pointed out by many researchers the most efficient quencher for OH* is molecular oxygen [McDade and Llewelyn, 1987; Makhlouf et.al., 1995; Adler-Golden, 1997]. The fifth term in the numerator and the third one in the denominator of formula above show that in the model the transitions from all highest vibrational levels to all lowest ones were taken into account. In order to derive quenching rates for all transitions a semiempirical parameterization [Adler-Golden, 1997] was used:

$$Q_w = C \cdot P_v^{\Delta v}, \quad (8.8)$$

where C is an empirical constant, P_v is the probability factor of transition $v \rightarrow v'$ which depends on the vibration number. The power Δv is the difference between vibrational numbers for a given transition $v \rightarrow v'$, in other words $\Delta v = v - v'$.

For the spontaneous emission in the present work, all transitions from higher values to lower values of the vibrational number were taken into account [Turnbull and Lowe, 1998].

8.2.3 Results

Figures 8.5-8.6 show latitude-height sections of the diurnally averaged hydroxyl mixing ratio for the north summer and north winter solstice, respectively. The decrease of the hydroxyl layer altitude from 80-90 km near the summer pole to 70-80 km near the winter pole is determined by the corresponding gradient of the water vapor concentration. Thus, for retrieving the temperature from airglow measurements the seasonal variation of altitudes of the OH layer must be taken into account.

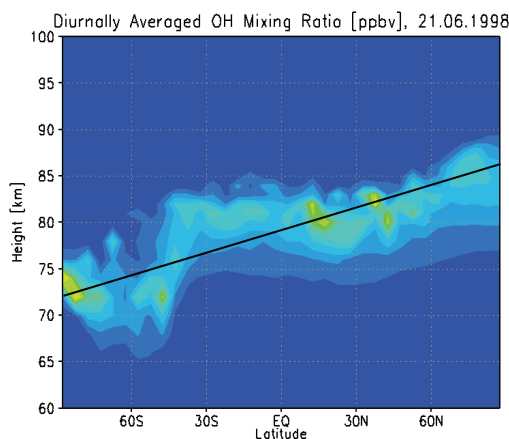


Figure 8.5 Diurnally averaged OH mixing ratio [ppbv] at 21.06.1998 calculated by LIMA.

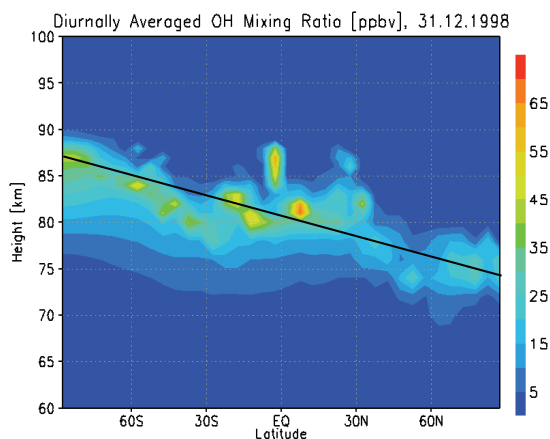


Figure 8.6. Diurnally averaged OH mixing ratio [ppbv] at 31.12.1998 calculated by LIMA.

Figures 8.7-8.9 display the annual behavior of diurnally averaged hydroxyl mixing ratios for equatorial (2.5° N), middle (47.5° N) and high (67.5° N) latitudes, respectively. Near the equator, an annual variation is almost absent. The calculations for high and middle latitudes show annual variations of the height of the OH layer and a semiannual variation of the OH number density. The annual variation of the height of the hydroxyl layer for high and middle latitudes is determined by the annual variation of water vapor. The summer maximum of the hydroxyl

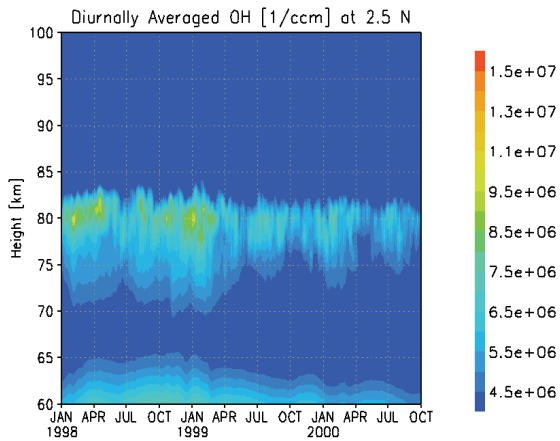


Figure 8.7. Diurnally averaged OH concentration [1/ccm] at 2.5° N calculated by LIMA.

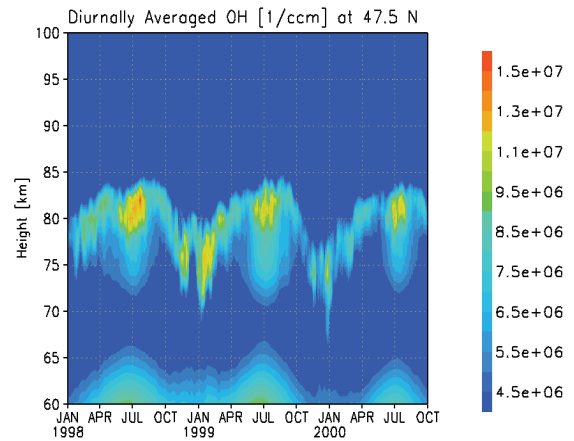


Figure 8.8. Diurnally averaged OH concentration [1/ccm] at 42.5° N calculated by LIMA.

number density is governed by increasing water vapor concentration at high and middle latitudes in the summer season. The winter maximum is caused by the increasing ozone concentration in the mesopause region during winter.

Figure 8.10 exhibits a comparison between the height and the ground state concentration of hydroxyl (shaded area) with those ones of the excited hydroxyl of vibrational number 9 (black

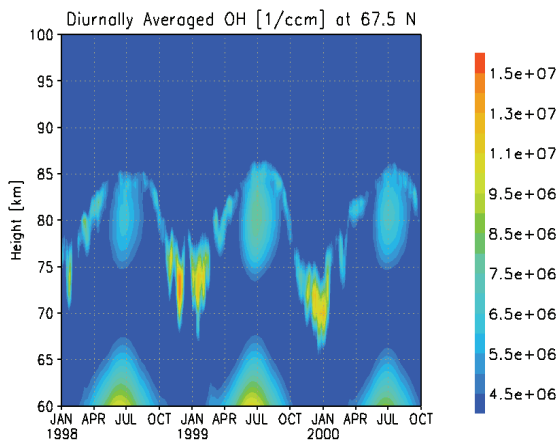


Figure 8.9. Diurnally averaged OH concentration [1/ccm] at 67.5° N calculated by LIMA.

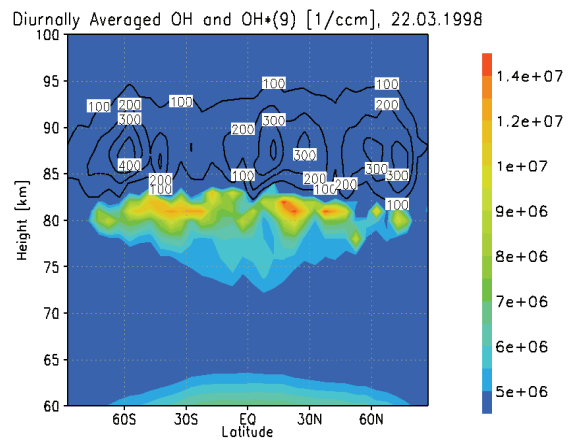


Figure 8.10. Diurnally averaged OH and OH*(v=9) concentrations [1/ccm] for 22.03.1998 calculated by LIMA.

lines) at spring equinox. The maximum of the excited hydroxyl is placed approximately 6 km higher than the maximum of the ground state hydroxyl and its concentration is clearly smaller.

The behavior of the vibrationally excited hydroxyl is illustrated by Figures 8.11 and 8.12. They depict globally and diurnally averaged excited states of hydroxyl at 67.5° N for different vibrational numbers at spring equinox. These figures demonstrate that with the decrease of the vibrational number, the altitude of the corresponding layer decreases. However, their concentration values rise under these conditions. These results are in good agreement with available measurements from a rocket experiment [Backer and Stair, 1988].

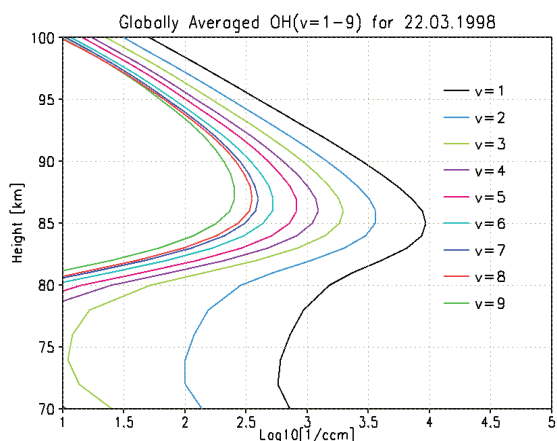


Figure 8.11. Globally averaged excited states of hydroxyl for different vibrational numbers for 22.03.1998 calculated by LIMA.

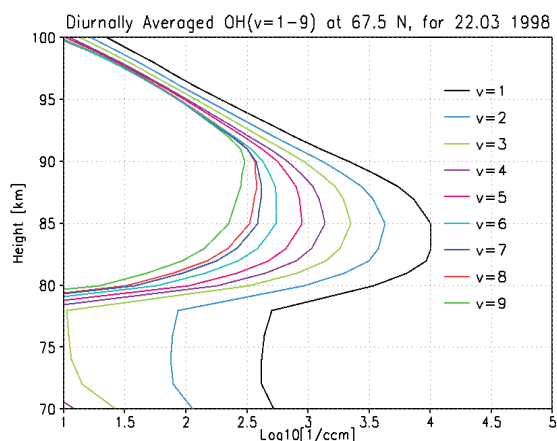


Figure 8.12. Diurnally averaged excited states of hydroxyl for different vibrational numbers for 22.03.1998 at 67.5° N calculated by LIMA.

8.3 Summary and Conclusions

In this chapter the submodels for calculations of chemical heating rates and for calculations of relaxation of excited hydroxyl were introduced and discussed.

The development of interactive coupled models of the dynamics and chemistry requires the calculation of chemical heating rates. The transport of latent chemical energy from the thermosphere into the mesopause region plays an important role for the heat balance in the region 80-100 km. The extreme values of total chemical heat reach more than 40 K/day and occurs at high latitudes during the winter under condition of downward transport of atomic oxygen. The chemical heating rate has a significant annual and latitudinal variation.

An improved kinetic model for the Meinel bands of OH* airglow has been constructed. The general features of the OH and OH* distribution were investigated by means of this model applying with the GCM LIMA. The most marked feature is a semiannual variation in middle and high latitudes with maxima around the solstices. The variation is controlled by the annual behavior of ozone and water vapor. A semiannual variation was also found by Offerman et al. [2000]. The OH* maximum is placed about 5 km higher than the OH layer. The height of OH* maximum at high and mean latitudes changes with season from 87 km during summer to 75 km during winter. This fact is important for temperature observations by airglow measurements. The altitudes of layers decrease with increase of the vibrational number approximately by 0.5 km per vibrational number. The concentration rises with increasing vibrational number. The model of relaxation can be applied for different purposes, for example for retrieving of altitude for temperature measurements by airglow emission, but additional experimental investigations and modeling are necessary to quantitatively test this model and improve our understanding of OH* behavior in the atmosphere.

Chapter 9

Summary and Outlook

9.1 The Most Important Results

During the last years, some improvements were implemented into the CTM. First, the Walcek scheme was applied to the advective transport scheme. Second, the Lyman-alpha radiation was parameterized according with solar activity using the sunspot number as a proxy. The chemical scheme was extended with regard to the CO-CO₂ chemistry and to the plasma constituents. CH₄, CO₂ and NO₂ trends were parameterized for long-term calculations. Finally, the dynamical output of LIMA has been applied to the CTM. A large number of model experiments were carried out in order to investigate topical geophysical problems. These computer experiments also represent the focal point of this work.

Below is a list of the most important results published in peer-reviewed international journals.

1. The influence of the zonal wind on the photochemistry of the mesosphere-lower thermosphere (MLT) region was investigated. This impact is called the photochemical Doppler effect and turned out to be a very robust effect playing a rather important role in the Earth and Martian middle atmosphere. These results aided in understanding the ozone behavior in its so-called tertiary maximum, also termed middle mesospheric maximum of ozone (MMM), and the variations during SSWs and planetary wave activity.
2. The solar influence on the photochemistry of the MLT-region due to the 11-year solar cycle was studied, particularly at high latitudes. An important result was that the varying Lyman-alpha radiation does not essentially impact the water vapor concentration at high latitudes below about 70 km during the summer season. Above 70 km the Lyman-alpha radiation has a significant influence on the water vapor mixing ratio with maximum impact on its values at high latitudes during summer. The explanation is given by the strong upward wind in summer that conveys humid air into the domain of stronger photolysis of water vapor.
3. The tertiary ozone maximum placed at high-latitude in the middle mesosphere, and spreading into the middle latitudes with decreasing amplitude, was correctly calculated and its features and annual time behavior was examined. The calculations showed that at high latitudes an annual double peak occurs. The reason for this phenomenon was analysed and it was found that, on the one hand, the differently strong decrease of the dissociation rates for ozone, molecular oxygen and water vapor with increasing solar zenith angle cause this effect. On the other hand, westward zonal wind direction typical for winter enhances the nighttime ozone of the middle mesosphere in the domain of the mesospheric wind jet. Additionally, one has to consider that the annual

variation of water vapor with lowest values in winter amplifying the wintry ozone enhancement and the annual temperature variation reduce this effect.

4. The influence of anthropogenic methane and carbon dioxide increase on the long-term behavior of minor constituents in the MLT region was studied. It was found that the water vapor mixing ratio rose in the middle atmosphere by 30%-60% with a maximum in the mesopause region since the preindustrial time (due to methane oxidation) but that the ozone concentration decreased simultaneously in the extended mesopause region.

5. The enhanced water vapor mixing ratios in the upper mesosphere at high latitude during the summer was studied and explained by the autocatalytic water vapor production from the H₂-reservoir below 65 km. Due to the very long effective lifetime of water vapor in the domain between 65 and 75 km, the water vapor is lifted upward by the vertical wind without a strong decrease during this transport.

6. Two-day oscillations and the non-linear behavior of ozone in the mesopause region were investigated. It was shown that the occurrence of a period-2 oscillation depends essentially on the vertical wind velocity and the season. During winter the effect is absent. Subharmonics also entails a subharmonic oscillation of the chemical heating rates.

7. The influence of sudden stratospheric warming (SSW) phenomena on the MLT region was studied. During SSWs, drastic changes of the composition occur. The causes are changes in temperature and advective transport. However, an accurate description of the variation of the minor constituents during the SSW requires the employment of an interactive coupling of dynamics and chemistry in the model. This is because the composition change feeds essentially back to the dynamics.

9.2 Open Questions and Future Improvements of the CTM

There are still different possibilities and ways to improve the model and to continue the model experiments. Some of these improvements have been listed below:

1. The LIMA triangular (simplex) net adaptation to the transport scheme of the CTM.

The interpolation from one net to another one takes too much computer time. However, the triangular net adaptation is necessary for future coupling.

2. Assimilation of ECMWF ozone data into the CTM.

This is necessary for the implementation of a more sophisticated self-consistent stratospheric chemistry in the model.

3. Provide full coupling of dynamics and chemistry.

An important task for the future work consists in the interactive coupling of the CTM with the dynamic model part of LIMA. The chemistry feeds essentially back to the dynamics. For example, ozone is the most important absorber of solar UV radiation, and carbon dioxide, water vapor, ozone etc. are infrared active constituents determining the cooling of the middle atmosphere. The chemical heating rate is rather important within the extended mesopause region. The collision of atomic oxygen with carbon dioxide transfers heat to vibrational states of carbon dioxide, thus cooling the atmosphere and so on. The changed temperature fields entail altered wind fields that influence the transport of these gases.

4. The implementation of a parameterization for the meridional diffusion in the model. Such improvement will make the model more precise, especially for the high latitudes near the poles.

5. The implementation of seasonally dependent eddy diffusion coefficients into the model. This would particularly improve the modeling in the extended mesopause region.

6. The plasma code is not applicable to high geomagnetic latitudes. It describes only undisturbed

mean and low latitudes. Particle precipitation and cosmic rays have to be considered. The NO_x chemistry has to be improved, and particularly the thermospheric sources depending on geomagnetic latitudes have to be modeled thoroughly. The water cluster chemistry is only parameterized and has to be essentially improved also including negative ions and processes important in the PMSE region.

Appendix A

History

The development of the current model has a long history. As early as 1983, Rose developed the first version of a primitive equation 3D-model. This model was the basis of all succeeding model versions, which have been abbreviated with COMMA standing for Cologne Model of the Middle Atmosphere. This successful dynamic model was used for quite some time to investigate phenomena such as the propagation of gravity waves and their energetic impact on the middle atmosphere [Jakobs, 1986; Jakobs and Hass, 1987; Jakobs et al., 1986], thermic tides [Berger, 1994], stratospheric warmings [Rose, 1983], quasi-biennial oscillations [Dameris and Ebel, 1990], impacts of the increasing CO₂ concentration on the thermic regime of the middle atmosphere [Berger and Dameris, 1993; Berger et al., 1994], and the ozone hole phenomenon [Dameris et al., 1991].

The mechanistic grid point model COMMA was a pure dynamical model calculating the global wind, temperature and pressure fields. In the early 1990s, this model was coupled with a chemical transport model (CTM) developed by Sonnemann and Kremp at the Institute of Atmospheric Physics in Kühlungsborn. The CTM consisted of chemical, radiation and transport codes used in the dynamical fields for the calculations of the chemical fields. By means of this model some special problems were investigated such as the distribution of NO, the calculation of the chemical heating rate, the plasma variation of the D- and E-layer, the mesospheric ozone distribution, and the comparison of calculated and measured mesospheric wind fields [Sonnemann et al. 1995, 1996, 1998a/b; Kremp et al. 1999]. The improvement of the dynamical model by a clever gravity wave parameterization resulted in the correct calculation of real temperatures and of the two distinctive level structures of the mesopause by Berger and von Zahn [1999]. The early versions of the COMMA model, now called COMMA-IAP, run on a workstation. The availability of a fast NEC parallel computer calls for a reconstruction of the entire computer program. U. Körner parallelized the computer program and made it faster by two orders of magnitude [Kömer, 2002]. Subsequently, it was possible to calculate long-term runs and to treat the mesospheric water vapor problem based on this model version [Körner and Sonnemann, 2001]. In 2002 the so-called total hydrogen mixing ratio anomaly (THYMRA) was detected using this model [Sonnemann and Körner, 2002]. THYMRA is a decrease of the total hydrogen mixing ratio with a minimum somewhat above the turbopause when taking into account the hydrogen escape flux. The calculated water vapor mixing ratios reflected the main patterns of the measured annual variation but resulted in values too low in the upper mesosphere and mesopause region. The explanation consisted in the use of a relatively diffusive transport scheme introduced by Smolarkiewicz [1983].

The COMMA-IAP represents a model calculating climatological means. It cannot consider the excitation of planetary waves and consequently it cannot model such events as sudden stratospheric warmings. In the meantime, a new real date dynamical model version has been developed by U. Berger using a so-called simplex or three-angle horizontal grid (reduced Gaussian grid). The model assimilates real-date ECMWF data (European Centre for Medium-Range Weather Forecasts) for horizontal wind components, pressure and temperature up to 35 km. It was called the Leibniz-Institute Middle Atmosphere (LIMA) model. The use of the new dynamical fields in the CTM permitted us to calculate real date fields of the chemical minor constituents and to compare them with real date measurements.

The main interest of the scientific community in modeling the dynamics and chemistry of the middle atmosphere is focused on the stratospheric ozone layer and related problems. There are several research groups working on this field in Germany (Hamburg, Berlin, Mainz, Karlsruhe and München). The mesosphere is often included as an upper model domain and the intricate mesopause region is excluded or it is simplified and neglects to treat variables such as the important molecular diffusion. There are many excellent scientific papers and books about the middle atmosphere, but only one reference is given here with 31 pages of references to publications mainly concerning middle atmospheric research [Brasseur et al., 1999].

Currently, there are different two-dimensional models including the mesospheric height range. Examples of these are from Brasseur et al. [1990], Yang et al. [1991], Jackman et al. [1991], Garcia et al. [1992], Ko et al. [1993] and Summers et al. [1997]. Two-dimensional models, however, if using the diurnal average of the dissociation rates, are not able to calculate the distribution of constituents with lifetimes comparable to one day. A main drawback results from the fact that tidal waves cannot be considered in two-dimensional models. As the results from these models show, the models are apparently very diffusive and do not display marked latitudinal variations below a global scale.

There were also some three-dimensional (3D) models developed comprising the domain of the mesosphere and lower thermosphere. The model of Arnold and Robinson [1998] has a height range extending from 10 to 140 km. Brasseur and de Baets [1986], and Richmond et al. [1992] used 3D-models. The TIME-GCM (Thermosphere-Ionosphere-Mesosphere-Exosphere-General Circulation Model) of Roble and Ridley [1994] and Liu and Roble [2002] comprises a height range from 30 to 800 km. It also considers plasma components and plasma transport. The drawback of such models comprising an extended height range consists in their relatively coarse height resolutions. Different versions based on the Rose model have been used [e.g. Brasseur et al., 2000; Marsh et al., 2001].

In Germany, the use of 3D-models differs as variants of the Hamburg climate model (ECHAM) ends at the stratopause. The Mainz version ECHAM4-MA has been extended up to 0.01 hP, corresponding to approximately 80 km. In addition, the COMMA model was distributed in Germany and currently some versions are used in Leipzig [Fröhlich et al., 2003] and Lindau.

Appendix B

Derivation of the Equation for Calculation of Eddy Diffusion

For diffusive equilibrium the flux induced by eddy diffusion for the number density of the air is

$$\Phi_k = -K \left(\frac{\partial n}{\partial z} + n \left(\frac{1}{H} + \frac{\partial \ln T}{\partial z} \right) \right) = 0. \quad (\text{B.1})$$

With a nonzero eddy diffusion coefficient, the underbraced term in B.1 has to be zero. This is an equivalent formulation to the use of log-pressure coordinates as used in COMMA-IAP.

$$p = p_0 e^{-z/H}, \quad H = \text{const}, z_0 = 0. \quad (\text{B.2})$$

With the ideal gas law, we get the height- and temperature-dependent number density of the air

$$p = nkT \Leftrightarrow n = \frac{p}{kT} = \frac{p_0 e^{-z/H}}{kT}. \quad (\text{B.3})$$

Differentiation of the number density yields

$$\frac{1}{n} \frac{\partial n}{\partial z} = - \left(\frac{1}{H} + \frac{1}{T} \frac{\partial T}{\partial z} \right) \Leftrightarrow \frac{\partial \ln n}{\partial z} = - \left(\frac{1}{H} + \frac{\partial \ln T}{\partial z} \right). \quad (\text{B.4})$$

Equation B.1 can be transformed into the change of the number density per unit time by the use of Fick's law.

$$\frac{\partial n}{\partial t} = - \frac{\partial}{\partial z} (\Phi_k) = \frac{\partial}{\partial z} \left(K \left(\frac{\partial n}{\partial z} + n \left(\frac{1}{H} + \frac{\partial \ln T}{\partial z} \right) \right) \right). \quad (\text{B.5})$$

The righthand sum of B.5 is equivalent to the zero value for the underbraced term in equation B.1. Taking into account a constant scale height and the ideal gas law meaning the same as the assumption of a zero flux for the number density of the air by eddy diffusion.

The equation for the calculation of the eddy diffusion of the i 'th constituent in terms of mixing ratio f_i can be derived.

$$n_i = n f_i \Rightarrow \frac{\partial n_i}{\partial z} = n \frac{\partial f_i}{\partial z} + f_i \frac{\partial n}{\partial z}, \quad (\text{B.6})$$

$$\Phi_{k,i} = -K \left(\frac{\partial n_i}{\partial z} + n_i \left(\frac{1}{H} + \frac{\partial \ln T}{\partial z} \right) \right), \quad (\text{B.7})$$

$$\frac{\partial n_i}{\partial z} = n \frac{\partial f_i}{\partial z} + f_i \frac{\partial n}{\partial z} = - \frac{\partial}{\partial z} (\Phi_{k,i}), \quad (\text{B.8})$$

$$n \frac{\partial f_i}{\partial z} + f_i \frac{\partial n}{\partial z} = \frac{\partial}{\partial z} \left(K \left(n \frac{\partial f_i}{\partial z} + f_i \frac{\partial n}{\partial z} + n f_i \left(\frac{1}{H} + \frac{\partial \ln T}{\partial z} \right) \right) \right), \quad (\text{B.9})$$

$$\begin{aligned} n \frac{\partial f_i}{\partial z} + f_i \frac{\partial n}{\partial z} &= \frac{\partial}{\partial z} \left(\underbrace{K n \frac{\partial f_i}{\partial z}}_A \right) + f_i \frac{\partial}{\partial z} \left(\underbrace{K \left(\frac{\partial n}{\partial z} + n \left(\frac{1}{H} + \frac{\partial \ln T}{\partial z} \right) \right)}_A \right) \\ &+ \frac{\partial f_i}{\partial z} \underbrace{K \left(\frac{\partial n}{\partial z} + n \left(\frac{1}{H} + \frac{\partial \ln T}{\partial z} \right) \right)}_{=0}. \end{aligned} \quad (\text{B.10})$$

The terms underbraced with A are equivalent to the diffusion of the air multiplied with the mixing ratio of the i'th constituent, and they equalize each other because the air is assumed to be in diffusive equilibrium. The third underbraced term is equal to zero according to B.1. The remaining terms are

$$n \frac{\partial f_i}{\partial z} = n \frac{\partial f_i}{\partial z} \frac{\partial K}{\partial z} + K \frac{\partial f_i}{\partial z} \frac{\partial n}{\partial z} + K n \frac{\partial^2 f_i}{\partial z^2}, \quad (\text{B.11})$$

$$\frac{\partial f_i}{\partial z} = K \frac{\partial^2 f_i}{\partial z^2} + \frac{\partial f_i}{\partial z} \left(\frac{\partial K}{\partial z} + K \frac{1}{n} \frac{\partial n}{\partial z} \right). \quad (\text{B.12})$$

With equation B.1, the resulting equation, which is used to calculate the effect of the eddy diffusion, is

$$\frac{\partial f_i}{\partial z} = K \frac{\partial^2 f_i}{\partial z^2} + \frac{\partial f_i}{\partial z} \left(\frac{\partial K}{\partial z} - K \left(\frac{1}{H} + \frac{\partial \ln T}{\partial z} \right) \right). \quad (\text{B.13})$$

Appendix C

Derivation of the Equation for Calculation of Molecular Diffusion

The derivative in z direction of the diffusion coefficient can be expressed in terms of z -derivative of the temperature to reduce the terms of the molecular diffusion.

$$\frac{\partial \hat{D}_i}{\partial z} = \beta_i \hat{D}_i \frac{\partial \ln T}{\partial z} \quad (\text{C.1})$$

The molecular diffusion will be transformed analogically to the derivation of the eddy diffusion.

$$\Phi_{D_i} = -D_i \left(\frac{\partial n_i}{\partial z} + n_i \left(\frac{1}{H} + \frac{\partial \ln T}{\partial z} \right) + n_i \left(\frac{1}{H} \left(\frac{m_i}{m} - 1 \right) + \alpha_i \frac{\partial \ln T}{\partial z} \right) \right) \quad (\text{C.2})$$

$$\Phi_{D_i} = \Phi_{D,i} + \Phi_{D,j} \quad (\text{C.3})$$

$$\Phi_{D,i} = -D_i \left(\frac{\partial n_i}{\partial z} + n_i \left(\frac{1}{H} + \frac{\partial \ln T}{\partial z} \right) \right) \quad (\text{C.4})$$

$$\Phi_{D,j} = -D_i n_i \left(\frac{1}{H} \left(\frac{m_i}{m} - 1 \right) + \alpha_i \frac{\partial \ln T}{\partial z} \right) \quad (\text{C.5})$$

The flux component $\Phi_{1,i}$ has the same mathematical structure as the flux resulting from the eddy diffusion.

$$\frac{\partial n_i}{\partial t} = -\frac{\partial}{\partial z} (\Phi_{D,i} + \Phi_{D,j}) \quad (\text{C.6})$$

$$\frac{\partial f_i}{\partial t} = D_i \frac{\partial^2 f_i}{\partial z^2} + \frac{\partial f_i}{\partial z} \left(\frac{\partial D_i}{\partial z} - D_i \left(\frac{1}{H} + \frac{\partial \ln T}{\partial z} \right) \right) - \frac{1}{n} \frac{\partial}{\partial z} (\Phi_{D,i}) \quad (\text{C.7})$$

Some precalculations are needed to get the z -derivative of the flux term

$$F_i(T) = \frac{1}{H} \left(\frac{m}{m_i} - 1 \right) + \alpha_i \frac{\partial \ln T}{\partial z}, \quad (\text{C.8})$$

$$\begin{aligned} -\frac{1}{n} \frac{\partial}{\partial z} (\Phi_{D,i}) &= \frac{1}{n} \frac{\partial}{\partial z} (D_i n_i F_i(T)) = \frac{1}{n} \frac{\partial}{\partial z} (D_i n f_i F_i(T)) \\ &= \frac{1}{n} \left(\frac{\partial f_i}{\partial z} D_i n F_i(T) + f_i \frac{\partial}{\partial z} (D_i n F_i(T)) \right) \\ &= \frac{\partial f_i}{\partial z} (D_i F_i(T)) + f_i \frac{1}{n} \frac{\partial}{\partial z} (D_i n F_i(T)) \\ &= \frac{\partial f_i}{\partial z} D_i \left(\frac{1}{H} \left(\frac{m_i}{m} - 1 \right) + \alpha_i \frac{\partial \ln T}{\partial z} \right) + f_i \frac{1}{n} \frac{\partial}{\partial z} (\hat{D}_i F_i(T)), \end{aligned} \quad (\text{C.9})$$

$$\begin{aligned} \frac{\partial}{\partial z} (\hat{D}_i F_i(T)) &= F_i(T) \frac{\partial \hat{D}_i}{\partial z} + \hat{D}_i \frac{\partial F_i(T)}{\partial z} \\ &= \beta_i \hat{D}_i F_i(T) \frac{\partial \ln T}{\partial z} + \hat{D}_i \alpha_i \frac{\partial}{\partial z} \left(\frac{\partial \ln T}{\partial z} \right), \end{aligned} \quad (\text{C.10})$$

$$\frac{\partial}{\partial z} \left(\frac{\partial \ln T}{\partial z} \right) = \frac{1}{T} \frac{\partial^2 T}{\partial z^2} - \left(\frac{1}{T} \frac{\partial T}{\partial z} \right)^2, \quad (\text{C.11})$$

$$-\frac{1}{n} \frac{\partial}{\partial z} (\Phi_{D,i}) = \frac{\partial f_i}{\partial z} D_i F_i(T) + f_i D_i \left(\beta_i \frac{\partial \ln T}{\partial z} F_i(T) + \alpha_i \frac{\partial}{\partial z} \left(\frac{\partial \ln T}{\partial z} \right) \right), \quad (\text{C.12})$$

$$\begin{aligned} \frac{\partial D_i}{\partial z} &= \frac{\partial}{\partial z} \left(\frac{\hat{D}_i}{n} \right) = \frac{1}{n} \frac{\partial \hat{D}_i}{\partial z} + \hat{D}_i \frac{\partial}{\partial z} \left(\frac{1}{n} \right) \\ &= \frac{1}{n} \beta_i \hat{D}_i \frac{\partial \ln T}{\partial z} + \hat{D}_i \frac{1}{n} \left(\frac{1}{H} + \frac{\partial \ln T}{\partial z} \right) \\ &= \beta_i D_i \frac{\partial \ln T}{\partial z} + D_i \left(\frac{1}{H} + \frac{\partial \ln T}{\partial z} \right), \end{aligned} \quad (\text{C.13})$$

$$\frac{\partial D_i}{\partial z} = D_i \left((1 + \beta_i) \frac{\partial \ln T}{\partial z} + \frac{1}{H} \right). \quad (\text{C.14})$$

The equation C.14 will be inserted into equation C.6. The terms are added to get a suitable structure.

$$\frac{\partial f_i}{\partial t} = \frac{\partial^2 f_i}{\partial z^2} D_i \quad (\text{C.15})$$

$$+ \frac{\partial f_i}{\partial z} \left(D_i \left((1 + \beta_i) \frac{\partial \ln T}{\partial z} + \frac{1}{H} \right) - D_i \left(\frac{1}{H} + \frac{\partial \ln T}{\partial z} \right) + D_i F_i(T) \right) \\ + f_i D_i \left(\beta_i \frac{\partial \ln T}{\partial z} F_i(T) + \alpha_i \frac{\partial}{\partial z} \left(\frac{\partial \ln T}{\partial z} \right) \right)$$

$$\frac{\partial f_i}{\partial t} = \frac{\partial^2 f_i}{\partial z^2} D_i + \frac{\partial f_i}{\partial z} D_i \left(\beta_i \frac{\partial \ln T}{\partial z} + F_i(T) \right) \\ + f_i D_i \left(\beta_i \frac{\partial \ln T}{\partial z} F_i(T) + \alpha_i \frac{\partial}{\partial z} \left(\frac{\partial \ln T}{\partial z} \right) \right) \quad (\text{C.16})$$

All terms of the equations B.13 and C.16 are added. They can be solved with the implicit Thomas algorithm as described in Morton and Mayers [1994]. The structure of equation C.17 allows very fast calculation of the diffusion terms and a maximum of precalculation for the terms of the innermost loop, and therefore a fast computer code with a high degree of vectorization.

$$\frac{\partial f_i}{\partial t} = \frac{\partial^2 f_i}{\partial z^2} (K + D_i) \quad (\text{C.17}) \\ + \frac{\partial f_i}{\partial z} \left(\frac{\partial K}{\partial z} - K \left(\frac{1}{H} + \frac{\partial \ln T}{\partial z} \right) + D_i \left(\beta_i \frac{\partial \ln T}{\partial z} + F_i(T) \right) \right) \\ + f_i D_i \left(\beta_i \frac{\partial \ln T}{\partial z} F_i(T) + \alpha_i \frac{\partial}{\partial z} \left(\frac{\partial \ln T}{\partial z} \right) \right)$$

Appendix D

Description of Walcek Scheme

The following derivation of the so-called Walcek scheme is based on works by Walcek and Aleksis [1998] and Walcek [2000]. Equation (2.13) can be expressed in terms of the tracer mixing ratio Q

$$\frac{\partial(\rho Q)}{\partial t} = - \frac{\partial(u\rho Q)}{\partial x}, \quad (\text{D.1})$$

where ρ is the fluid density. Equation (D.1) is numerically approximated by using a forward time difference and evaluating the space derivative at time t . The mixing ratios at time $t + \Delta t$ can be initially estimated using

$$Q_i^{\text{guess}} = \frac{\left[Q_i^t D_{d-1} - \frac{(\Delta t u \rho Q_f)_{i+1/2}}{\Delta x_i} + \frac{(\Delta t u \rho Q_f)_{i-1/2}}{\Delta x_i} \right]}{D_d} \quad (\text{D.2})$$

Here, Q_f is the average mixing ratio within the fluid flowing across each cell edge during time step Δt . D_{d-1} and D_d are either the dimensionally dependent fluid densities at the beginning and end of the time step, or the dimensional step in a multidimensional calculation performed one dimension at a time. The subscript $i+1/2$ refers to the "higher- i " face of each cell (the edge of cell i nearest to $i+1$ cell), and $i-1/2$ refers to the "lower- i " side of the cell. Two or three-dimensional advection calculations are performed by applying this one dimensional algorithm sequentially over each dimension. However, as described below, the fluid densities D_d must be sequentially changed for the second and third dimensions even in incompressible fluids, while the ρ terms used to calculate fluxes are held fixed at the initial fluid density for all dimensions.

Fluxes are evaluated using the 2nd-order accurate [van Leer, 1977] approach, which assumes a linear distribution of tracer within each grid cell, and the gradient within the cell equaling $\partial Q / \partial x = (Q_{i+1} - Q_{i-1}) / 2\Delta x_i$. The average mixing ratio Q_i in the fluid transported out of each cell during Δt , is

$$\left(Q_f\right)_{i+1/2} = Q_i + \frac{(Q_{i+1} - Q_i)(1-c)}{4} \alpha, \quad u_{i+1/2} \geq 0 \quad (\text{D.3})$$

$$\left(Q_f\right)_{i-1/2} = Q_i + \frac{(Q_{i-1} - Q_i)(1-c)}{4} \alpha, \quad u_{i-1/2} < 0 \quad (\text{D.4})$$

where c is the local "upwind" Courant-Friedrich-Lewy number [Courant et al., 1928] ($c = u_{i+1/2} \Delta t / \Delta x_i; u_{i+1/2} \geq 0$ and $c = |u_{i-1/2}| \Delta t / \Delta x_i; u_{i-1/2} < 0$). α is specified using equation (D.13). Dimensionally dependent densities (D_d in equation D.2) are specified as

$$\begin{aligned} D_0 &= \rho_i, \\ D_1 &= D_0 - \left[(\rho u)_{i+1/2} - (\rho u)_{i-1/2} \right] \Delta t / \Delta x_i, \\ D_2 &= D_1 - \left[(\rho v)_{i+1/2} - (\rho v)_{i-1/2} \right] \Delta t / \Delta y_j, \\ D_3 &= D_2 - \left[(\rho w)_{i+1/2} - (\rho w)_{i-1/2} \right] \Delta t / \Delta z_k, \end{aligned} \quad (\text{D.5})$$

where ρ_i is the initial fluid density, and $\rho_{i\pm 1/2}$ is the density of fluid advected across the specified cell interface. Cross-flowing densities $\rho_{i\pm 1/2}$ can be defined using an upstream approach or other approximations but must be identical to the densities used in defining the tracer fluxes in equation (D.2). ρ terms in (D.2) and (D.5) are the same for each dimension of a multidimensional calculation, while D_d terms change with each dimension. For three-dimensional cases, mixing ratios first update doing x direction advection using u velocities. These updated mixing ratios are then advected in the y direction using v velocities, followed by z dimension advection using w velocities. During x advection D_0 and D_1 are used in (D.2) for D_{d-1} and D_d . During y advection with velocities v , D_1 and D_2 are used, and during z , advection D_2 and D_3 are used in (D.2). Using this operator splitting approach for multidimensional advection, fluid density can artificially change when performing advection in one dimension, even in nondivergent flows, but any artificial density perturbations are intermediate and are naturally compensated during subsequent dimension calculations.

A monotonic advection algorithm will never generate mixing ratios higher than the highest mixing ratio initially present in the mixing ratio field, nor will a mixing ratio ever become lower than the lowest initial mixing ratio. Here, monotonic constraints are employed locally based on obvious physical limitations. If the Courant-Friedrich-Lewy number is $i < 1$ at time $t + \Delta t$, it is physically impossible for updated mixing ratios to be greater than the highest mixing ratio of the upwind cell or the initial mixing ratio of the cell. Likewise, updated mixing ratios cannot be lower than the lowest initial mixing ratio in the cell. Monotonicity is guaranteed through two steps. First, Q_f in (D.3) and (D.4) is constrained to fall in the range of the mixing ratios on either side of the interface where fluxes are evaluated:

$$\min(Q_i, Q_{i+1}) < \left(Q_f\right)_{i+1/2} < \max(Q_i, Q_{i+1}) \quad u_{i\pm 1/2} \geq 0, \quad (\text{D.6})$$

$$\min(Q_i, Q_{i-1}) < (Q_f)_{i-1/2} < \max(Q_i, Q_{i-1}) \quad u_{i-1/2} < 0. \quad (\text{D.7})$$

Second, outflowing fluxes are adjusted so that updated mixing ratios never exceed or fall below the physically constrained highest $Q_{\max}^{t+\Delta t}$ and lowest $Q_{\min}^{t+\Delta t}$ mixing ratios allowed. These upper and lower limits are given by

$$Q_{\min}^{t+\Delta t} = \min(Q_i, Q_{i-1}) \quad Q_{\max}^{t+\Delta t} = \max(Q_i, Q_{i-1}) \quad u_{i-1/2} \geq 0, \quad (\text{D.8})$$

$$Q_{\min}^{t+\Delta t} = \min(Q_i, Q_{i+1}) \quad Q_{\max}^{t+\Delta t} = \max(Q_i, Q_{i+1}) \quad u_{i+1/2} < 0. \quad (\text{D.9})$$

In inflow-only cells where $u_{i-1/2} \geq 0$ and $u_{i+1/2} < 0$, the mixing ratio limits are the maximum or minimum of the three cells Q_{i-1}, Q_i, Q_{i+1} contributing mass to the cell during Δt . If Q_i^{guess} calculated using (D.2) violates these monotonic constraints, the updated mixing ratio is set to the violated limit

$$Q_i^{t+\Delta t} = \max\left[\min(Q_{\max}^{t+\Delta t}, Q_i^{\text{guess}}), Q_{\min}^{t+\Delta t}\right], \quad (\text{D.10})$$

then the outflowing flux is adjusted so that the $Q_i^{t+\Delta t}$ equals the violated limit:

$$(\Delta t u \rho Q_f)_{i+1/2} = [Q_i^t D_{d-1} - Q_i^{t+\Delta t} D_d] \Delta x_i + (\Delta t u \rho Q_f)_{i-1/2} \quad u_{i+1/2} \geq 0, \quad (\text{D.11})$$

$$(\Delta t u \rho Q_f)_{i-1/2} = [Q_i^{t+\Delta t} D_d - Q_i^t D_{d-1}] \Delta x_i + (\Delta t u \rho Q_f)_{i+1/2} \quad u_{i-1/2} < 0. \quad (\text{D.12})$$

Overall numerical diffusion is significantly removed by a minor adjustment of the factor α in (D.3) and (D.4) near local extremes. If there is a local extreme at the cell immediately downwind of the edge where fluxes are calculated. There used two adjustments together

$$\alpha_d = 1.75 - 0.45c \quad (\text{D.13})$$

$$\alpha_u = \max(1.5, 1.2 + 0.6c)$$

if the cell two cells upwind of the face where fluxes are being calculated is a local extreme. In (D.13), c is the upwind Courant number. These two adjustments together "sandwich" each local extreme and, therefore, effectively aggregate all tracer around local maximums in a manner that counters the numerical diffusion that diffuses mass away from extremes.

Appendix F

The Chemical Reactions

N	Reaction	Rate	Reference
1	$O+O+M \rightarrow O_2+M$	$3.7 \cdot 10^{-33}(300/T)^{2.0}$	Brasseur and Solomon [1986]
2	$O+O_2+M \rightarrow O_3+M$	$6.0 \cdot 10^{-34}(300/T)^{2.3}$	Brasseur and Solomon [1986]
3	$O+O_3 \rightarrow 2O_2$	$8.0 \cdot 10^{-12}\exp(-2060/T)$	Sander et al.[2003]
4	$O(^1D)+N_2 \rightarrow O(^3P)+N_2$	$1.8 \cdot 10^{-11}\exp(-110/T)$	DeMore et al.[1994]
5	$O(^1D)+O_2 \rightarrow O(^3P)+O_2$	$3.2 \cdot 10^{-11}\exp(-70/T)$	DeMore et al.[1994]
6	$O(^1D)+O_3 \rightarrow 2O_2$	$1.2 \cdot 10^{-10}$	Brasseur and Solomon [1986]
7	$O(^1D)+O_3 \rightarrow O_2+2O$	$1.2 \cdot 10^{-10}$	Brasseur and Solomon [1986]
8	$H_2O+O(^1D) \rightarrow 2OH$	$2.2 \cdot 10^{-10}$	Brasseur and Solomon [1986]
9	$H_2+O(^1D) \rightarrow H+OH$	$1.0 \cdot 10^{-10}$	Brasseur and Solomon [1986]
10	$H+O_2+M \rightarrow HO_2+M$	$5.7 \cdot 10^{-32}(300/T)^{1.6}$	DeMore et al.[1994]
11	$H+O_3 \rightarrow OH+O_2$	$1.4 \cdot 10^{-10}\exp(-470/T)$	Brasseur and Solomon [1986]
12	$OH+O \rightarrow H+O_2$	$2.2 \cdot 10^{-11}\exp(-120/T)$	DeMore et al.[1994]
13	$OH+O_3 \rightarrow HO_2+O_2$	$1.6 \cdot 10^{-12}\exp(-940/T)$	Brasseur and Solomon [1986]
14	$HO_2+O_3 \rightarrow OH+2O_2$	$1.1 \cdot 10^{-14}\exp(-500/T)$	DeMore et al.[1994]
15	$HO_2+O \rightarrow OH+O_2$	$3.0 \cdot 10^{-11}\exp(-200/T)$	Brasseur and Solomon [1986]
16	$2OH \rightarrow H_2O+O$	$4.2 \cdot 10^{-12}\exp(-240/T)$	DeMore et al.[1994]
17	$OH+HO_2 \rightarrow H_2O+O_2$	$4.8 \cdot 10^{-11}\exp(-250/T)$	DeMore et al.[1994]
18	$OH+H_2 \rightarrow H_2O+H$	$5.5 \cdot 10^{-12}\exp(-2000/T)$	DeMore et al.[1994]
19	$H+HO_2 \rightarrow 2OH$	$7.2 \cdot 10^{-11}$	Atkinson et al.[1992]
20	$H+HO_2 \rightarrow H_2+O_2$	$5.6 \cdot 10^{-12}$	Atkinson et al.[1992]
21	$H+HO_2 \rightarrow H_2O+O$	$2.4 \cdot 10^{-12}$	Atkinson et al.[1992]
22	$HO_2+NO \rightarrow OH+NO_2$	$3.7 \cdot 10^{-12}\exp(-240/T)$	Brasseur and Solomon [1986]
23	$2HO_2 \rightarrow H_2O_2+O_2$	$2.3 \cdot 10^{-13}\exp(-600/T)$	DeMore et al.[1994]
24	$H_2O_2+OH \rightarrow H_2O+HO_2$	$2.9 \cdot 10^{-12}\exp(-160/T)$	DeMore et al.[1994]
25	$H_2O_2+O \rightarrow OH+HO_2$	$1.4 \cdot 10^{-12}\exp(-2000/T)$	Brasseur and Solomon [1986]
26	$N+OH \rightarrow NO+H$	$3.8 \cdot 10^{-11}\exp(-85/T)$	Atkinson et al.[1992]

27	H+NO ₂ OH+NO	4.0 10 ⁻¹⁰ exp(340/T)	DeMore et al.[1992]
28	H+OH+N ₂ H ₂ O+N ₂	1.38 10 ⁻²⁴ (1/T) ^{2.6}	DeMore et al.[1990]
29	2OH+M H ₂ O ₂ +M	6.9 10 ⁻³¹ (300/T) ^{0.8}	DeMore et al.[1990]
30	2HO ₂ +M H ₂ O ₂ +O ₂ +M	1.7 10 ⁻³³ exp(1000/T)	DeMore et al.[1990]
31	NO ₂ +O NO+O ₂	6.5 10 ⁻¹² exp(120/T)	DeMore et al.[1994]
32	NO+O ₃ NO ₂ +O ₂	2.0 10 ⁻¹² exp(1400/T)	DeMore et al.[1994]
33	N+NO ₂ N ₂ O+O	3.0 10 ⁻¹²	Brasseur and Solomon [1986]
34	N+NO N ₂ +O	3.4 10 ⁻¹¹	Brasseur and Solomon [1986]
35	N+O ₂ NO+O	4.4 10 ⁻¹² exp(3320/T)	Brasseur and Solomon [1986]
36	NO ₂ +O ₃ NO ₃ +O ₂	1.2 10 ⁻¹³ exp(2450/T)	Brasseur and Solomon [1986]
37	NO ₃ +NO 2NO ₂	1.3 10 ⁻¹¹ exp(250/T)	Brasseur and Solomon [1986]
38	NO ₃ +O NO ₂ +O ₂	1.0 10 ⁻¹¹	Brasseur and Solomon [1986]
39	N ₂ O+O(¹ D) N ₂ +O ₂	4.9 10 ⁻¹¹	Brasseur and Solomon [1986]
40	N ₂ O+O(¹ D) 2NO	6.7 10 ⁻¹¹	Brasseur and Solomon [1986]
41	NO+O+M NO ₂ +M	9.0 10 ⁻³² (300/T) ^{1.5}	DeMore et al.[1994]
42	NO ₂ +O+M NO ₃ +M	9.0 10 ⁻³² (300/T) ^{2.0}	DeMore et al.[1994]
43	O ₃ +N NO+O ₂	1.0 10 ⁻¹⁶	DeMore et al.[1990]
44	CH ₄ +O(¹ D) CH ₃ +OH	1.4 10 ⁻¹⁰	Brasseur and Solomon [1986]
45	CH ₄ +O(¹ D) CH ₂ O+H ₂	1.4 10 ⁻¹¹	Brasseur and Solomon [1986]
46	CH ₄ +OH CH ₃ +H ₂ O	2.65 10 ⁻¹² exp(1800/T)	DeMore et al.[1994]
47	Cl+O ₃ ClO+O ₂	2.8 10 ⁻¹¹ exp(257/T)	Brasseur and Solomon [1986]
48	ClO+O Cl+O ₂	4.7 10 ⁻¹¹ exp(50/T)	Brasseur and Solomon [1986]
49	ClO+NO Cl+NO ₂	6.2 10 ⁻¹² exp(294/T)	Brasseur and Solomon [1986]
50	Br+O ₃ BrO+O ₂	1.4 10 ⁻¹¹ exp(755/T)	Brasseur and Solomon [1986]
51	BrO+O Br+O ₂	3.0 10 ⁻¹¹	Brasseur and Solomon [1986]
52	BrO+NO Br+NO ₂	8.7 10 ⁻¹² exp(265/T)	Brasseur and Solomon [1986]
53	BrO+OH Br+HO ₂	1.0 10 ⁻¹¹	Brasseur and Solomon [1986]
54	BrO+ClO Br+Cl+O ₂	3.0 10 ⁻¹¹	Brasseur and Solomon [1986]
55	BrO+BrO 2Br+O ₂	6.0 10 ⁻¹⁴ exp(150/T)	Brasseur and Solomon [1986]
56	CO+OH CO ₂ +H	1.5 10 ⁻¹³	Brasseur and Solomon [1986]

References

- Abarbanel, H. D. I.: Analysis of observed chaotic data, Springer-Verlag, *New York-Berlin-Heidelberg*, 1995.
- Adler-Golden, S., Kinetic parameters for OH nightglow modeling consist with recent laboratory measurements, *J. Geophys. Res.*, **102**, 19,969-19,976, 1997.
- Alpers, M., M. Gerding, J. Hoffner, and U. von Zahn, NLC particle properties from a five-color lidar observation at 54° N, *J. Geophys. Res.*, **105**, 12,235-12,240, 2000.
- Arnold, N. F., and T. R. Robinson, Solar cycle changes to planetary wave propagation and their influence on the middle atmosphere circulation, *Ann. Geophys.*, **16**, 69-76, 1998.
- Atkinson, R., D. L. Baulch, R. A. Cox, R. F. Hampson Jr., J.A. Kerr, and J. Troe, Evaluated Kinetic and Photochemical Data for Atmospheric Chemistry: Supplement IV, *Atmospheric Environment*, **26A**, 1187-1230, 1992.
- Azeem, S. M. I., Palo, S. E., Wu, D. L., and Friedevox, L.: Observations of the 2-day wave in UARS MLS temperature and ozone measurements, *Geophys. Res. Lett.*, **28**, 3147-3150, 2001
- Baker, D. J., and A. T. Stair Jr., Rocket measurements of the altitude distributions of the hydroxyl airglow, *Phys. Scri.*, **37**, 611-617, 1988.
- Banks, P.M. and G. Kockarts, *Aeronomy, Part A and B*, Academic Press, New York and London, 1973.
- Bauer, S. J., The constitution of the topside ionosphere, *Electron Density Profiles in Ionosphere and Exosphere*, ed. by J. Trihagen, North-Holland, Amsterdam, 1966.
- Berger, U., Numerische Simulation klimatologischer Prozesse und thermischer Gezeiten in der mittleren Atmosphäre, *Dissertation*, Universität Köln, 1994.
- Berger, U., and Dameris, Cooling of the upper atmosphere due to CO₂ increase: A model study, *An. Geophys.*, **11**, 809-819, 1993.
- Berger, U., and U. von Zahn, The two-level structure of the mesopause: A model study, *J. Geophys. Res.*, **104**, 22,083-22,093, 1999
- Berger, U. and von Zahn, U.: Icy particles in the summer mesopause region: Three-dimensional modeling of their environment and two-dimensional modeling of their transport, *J. Geophys. Res.*, **107**, 1366, doi:10.1029/2001JA000316, 2002.
- Berger, U., and F.-J. Lübken, Weather in mesospheric ice layers, *Geophys. Res. Lett.*, **33**, doi:10.1029/2005GL024841, 2006.
- Bevilacqua, R. M., W. J. Wilson, W. B. Rickelts, R. Schwartz, and R. J. Howard, Possible

- seasonal variability of mesospheric water vapour, *Geophys. Res. Lett.*, **12**, 397-400, 1985.
- Bott, A., A Positive Definite Advection Scheme Obtained by Nonlinear Renormalization of the Advective Fluxes, *Mon. Wea. Rev.*, **117**, 1006-1015, 1989.
- Bott, A., Monotone Flux Limitation in the Area Preserving Flux-from Advection Algorithm, *Mon. Wea. Rev.*, **120**, 2592-2602, 1992.
- Brasseur, G., and P. de Baets, Ions in the mesosphere and lower thermosphere: A two-dimensional model, *J. Geophys. Res.*, **91**, 4025-4046, 1986.
- Brasseur, G., and D. Offermann, Recombination of Atomic Oxygen Near the Mesopause: Interpretation of Rocket Data, *J. Geophys. Res.*, **91**, 10,818-10,824, 1986.
- Brasseur, G., and S. Solomon, *Aeronomy of the Middle Atmosphere: Chemistry and Physics of the Stratosphere and Mesosphere*, D. Reidel Publishing Company, Dordrecht, Holland, Second revised edition, 1986.
- Brasseur, G., M. H. Hitchman, S. Walters, M. Dymek, E. Falise, and M. Pirre, An interactive chemical and dynamical radiative two-dimensional model of the middle atmosphere, *J. Geophys. Res.*, **95**, 5639-5655, 1990.
- Brasseur, G., J. J. Orlando, and G. S. Tyndall, *Atmospheric Chemistry and Global Change*, Oxford University Press, Oxford New York, 1999.
- Brasseur, G., et al., Natural and human-induced perturbations in the middle atmosphere: a short tutorial, Atmospheric Science across the Stratopause, *Geophysical Monograph*, **123**, 7-20, AGU, 2000.
- Chamberlain, J. W., and D. M. Hunten, *Theory of Planetary Atmospheres, An Introduction to Their Physics and Chemistry*, Academic Press, Inc., San Diego, USA, Second edition, 1987.
- Chapman, S., A theory of upper-atmospheric ozone, *Mem. Roy. Meteorol. Soc.*, **3**, 103-125, 1930.
- Charney, J. G., P. G. Drazin, Propagation of planetary scale waves from the lower atmosphere to the upper atmosphere, *J. Geophys. Res.*, **66**, 83-109, 1961.
- Charters, P. E., R. G. McDonald, and J. C. Polanyi, Formation of vibrationally excited OH by the reaction H+O₃, *Appl. Opt.*, **10**, 1747-1756, 1971.
- CIRA 1986: *COSPAR International Reference Atmosphere*, Eds. D. Rees, J. J. Barnett, and K. Labitzke, Pergamon Press, 1990.
- Clancy, R. T., D. W. Rusch, R. J. Thomas, M. Allen, R. S. Eckman, Model ozone photochemistry on the basis of solar mesospheric explorer mesospheric observations, *J. Geophys. Res.*, **92**, 3067-3080, 1987.

Clancy, R. T., B. J. Sandor, and D. W. Rusch, Microwave observations and modeling of HO₂, H₂O and O₃ in the mesosphere, *J. Geophys. Res.*, **99**, 5465-5473, 1994.

Conway, R. R., M. Summers, M. Stevens, J. G. Cardon, P. Preusse and D. Offermann, Satellite observations of upper stratospheric and mesospheric OH: The HO_x dilemma, *Geophys. Res. Lett.*, **27**, 2613-2616, 2000.

Courant, R., K. O. Friedrichs, and H. Lewy, über die partiellen Differenzgleichungen der mathematischen Physik, *Math. Ann.*, **100**, 32, 1928.

Craig, R. L., Vincent, R. A., Fraser, G. J., and Smith, J. M.: The quasi 2-day wave near 90 km altitude at Adelaide (35. S), *Nature*, **287**, 319-302, 1980.

Cravens, T. E., J.-C. Gerard, M. LeCompte, A. I. Stewart, and D. W. Rusch, The global distribution of nitric oxide in the thermosphere as determined by the Atmosphere Explorer D Satellite, *J. Geophys. Res.*, **90**, 9862, 1985.

Crutzen, P. J., Energy conversions and mean vertical motions in the high latitude summer mesosphere and lower termsosphere, in *Mesospheric Models and Related Experiments*, edited by G. Fiocco, D. Reidel, pp. 78-88, Norwell, Mass., 1971.

DeMore, W. B., S. P. Sander, D. M. Golden, M. J. Molina, R. F. Hampson, M. J. Kurylo, C. J. Howard, and A. R. Ravishankara, *Chemical Kinetics and Photochemical Data for Use in Stratospheric Modelling*, Jet Propulsion Laboratory, California Institute of Technology, Evaluation No. 9, JPL Publication 90-1, 1990.

DeMore, W. B., S. P. Sander, D. M. Golden, R. F. Hampson, M. F. Kurylo, C. J. Howard, and A. R. Ravishankara, C. E. Kolb, M. J. Molina, Chemical kinetics and photochemical data for use in stratospheric modeling, *JPL Publ. 90-4*, 1997.

Dlugokencky, E. J., S. Houweling, L. Bruhwiler, K. A. Masarie, P. M. Lang, J. B. Miller, and P. P. Tans, Atmospheric methane levels off: Temporary pause or anew steady-state?, *Geophys. Res. Lett.*, **30**, 1992, doi:10.1029/2003GL018126, 2003.

Dowdy, A., R. A. Vincent, K. Igarashi, Y. Murayama, and J. Murphy, A comparison of mean winds and gravity wave activity in the northern and southern polar MLT, *Geophys. Res. Lett.*, **28**, 1475-1478, 2001.

Doyle, E. M.: Wind measurements in the upper atmosphere, *Ph.D. thesis*, University of Adelaide, Australia, 1968.

Duffing, G.: *Erzwungene Schwingungen bei ver nderlicher Eigenfrequenz*, Vieweg, Braunschweig, 1918.

Ebel, A., U. Berger, and B. C. Kr ger, Numerical simulations with COMMA, a global model of the middle atmosphere, *Simpo Newsl.*, **4**, No. 12, 22-32, Step Simul. Promotion Off., Japan, February, 1995.

Eluszkiewicz, J., M. Allen, A global analysis of the ozone deficit in the upper stratosphere and lower mesosphere, *J. Geophys. Res.*, **98**, 1069-1082 (1993).

Evans, S. J., R. Toumi, J. E. Harries, M. P. Chipperfield, and J. M. Russel, Trends in stratospheric humidity and the sensitivity of ozone to these trends, *J. Geophys. Res.*, **103**, 8715-8725, 1998.

Feigin, A. M.: Nonlinear dynamic models of atmospheric photochemical systems: Methods for construction and analysis (Review). *Izvestiya RAS: Atmos. Ocean. Phys.*, **38**, 513-554, 2002.

Feigin, A. M., Konovalov, and Ya., I. B., Mol'kov, I.: Toward an understanding of the nonlinear nature of atmospheric photochemistry: essential dynamic model of the mesospheric photochemical system, *J. Geophys. Res.*, **103**, 25 447-25 460, 1998.

Feigin, A. M., Mol'kov, Ya. I., Mukhin, D. N., and Loskutov, E. M.: Prognosis of qualitative behavior of a dynamic system by the observed chaotic time series, *Radiophys. Quant. Elec.*, **44**, 348-367, 2001.

Fichtelmann, B. and Sonnemann, G.: The strange attractor in the photochemistry of ozone in the mesopause region, *Acta. Geod. Geophys. Mont. Hung.*, **22** (1-2), 313-319, 1987.

Fichtelmann, B., and G. Sonnemann, On the Variation of Ozone in the Upper Mesosphere and Lower Thermosphere: A Comparison between Theory and Observation, *Z. Meteorol.*, **39**, 6, 297-308, 1989.

Fichtelmann, B. and Sonnemann, G.: Non-linear behaviour of the photochemistry of minor constituents in the mesosphere, *Ann. Geophys.*, **10**, 719-728, 1992.

Fomichev, V. I., J.-P. Blanchet, and D. S. Turner, Matrix parametrization of the 15 μm CO₂ band cooling in the middle and upper atmosphere for variable CO₂ concentrations, *J. Geophys. Res.*, **103**, 11,505-11,528, 1998.

Forbes, J. M.: Atmospheric tides 1. model description and results for solar diurnal component, *J. Geophys. Res.*, **87**, 5222-5240, 1982.

Foster, P. M. de F. and K. P. Shine, Stratospheric water vapour changes as a possible contributor to observed stratospheric cooling, *Geophys. Res. Lett.*, **26**, 3309-3312, 1999.

Fröhlich, K., A. I. Pogoreltsev, Ch. Jacobi, The 48 layer version COMMA-LIM model: Model description, new aspects and climatology, *Wiss. Mitt. d. Instituts f. Meteorologie Leipzig*, **30**, 157-185, 2003.

Garcia, R. R., and S. Solomon, A numerical model of the zonally averaged dynamical and chemical structure of the middle atmosphere, *J. Geophys. Res.*, **88**, 1379-1400, 1983.

Garcia, R. R., and S. Solomon, The effect of breaking gravity waves on the dynamics and chemical composition of the mesosphere and lower thermosphere, *J. Geophys. Res.*, **90**, 3850-

3868, 1985.

Garcia, R. R., F. Stordal, S. Solomon, and J. F. Kiehl, A numerical model of the middle atmosphere 1. Dynamics and transport of tropospheric source gases, *J. Geophys. Res.*, **97**, 12,967-12,991, 1992.

Gibbins, C. J., P. R. Schwartz, D. L. Thaker, and R. M. Bevilacqua, The variability of mesospheric water vapor, *Geophys. Res. Lett.*, **9**, 131-134, 1982.

Grygalashvily, M. and G. R. Sonnemann, Trends of mesospheric water vapor due to the increase of methane - a model study, accepted in *Adv. Space Res.*, 2005.

HALOE: Halogen Occultation Experiment on board of the Upper Atmosphere Research Satellite, data available on-line: <http://haloedata.larc.nasa.gov/home.html>

Haltiner, G., and R. Williams, Numerical Prediction and Dynamic Meteorology, 2nd Edition, John Wiley & Sons, 1980.

Hampson, R. F., Chemical kinetic and chemical data sheets for atmospheric reactions, Rep. *FAA-EE-80-17*, U.S. Dep. of Transp., Washington, D.C., 1987.

Harries, J. E., J. M. Russell III, A. F. Tuck, L. L. Gordley, P. Purcell, K. Stone, R. M. Bevilacqua, M. Gunson, G. Nedoluha, and W. A. Traub, Validation of measurements of water vapour from the Halogen Occultation Experiment, HALOE, *J. Geophys. Res.*, **101**, 10,205-10,216, 1996a.

Harries, J. E., S. Ruth, and J. M. Russell III, On the distribution of mesospheric molecular hydrogen inferred from HALOE measurements of H₂O and CH₄, *Geophys. Res. Lett.*, **23**, 297-300, 1996b.

Harris, T. J.: A long-term study of the quasi-two-day wave in the middle atmosphere, *J. Atmos. Terr. Phys.*, **36**, 569-579, 1994.

Hartogh, P., and Jarchow, Ground-based detection of middle atmospheric water vapour, Global Process Monitoring and Remote Sensing of the Ocean and Sea Ice, ed. by D. W. Deering and P. Gudmandsen, *Vol. 2586 of Proc. SPIE*, pp 188-195, 1995.

Hartogh, P., G. K. Hartmann, and P. Zimmermann, Simultaneous water vapor and ozone measurements with millimeter-waves in the stratosphere and mesosphere, *IEEE Catalog Number 91CH2971-0*, **1**, 227-230, 1991.

Hartogh, P., C. Jarchow, G. R. Sonnemann and M. Grygalashvily, On the spatiotemporal behavior of ozone within the upper mesosphere/mesopause region under nearly polar night conditions, *J. Geophys. Res.*, **109**, D18303, doi:10.1029/2004JD004576, 2004.

Holton, J. R., A semi-spectral numerical model for wave-mean flow interactions in the stratosphere: Application to sudden stratospheric warmings, *J. Atmos. Sci.*, **33**, 1639-1649, 1976.

Holton, J. R., An Introduction to Dynamik Meteorology, Third Edition, Academic Press, San Diego, 1992.

Hunten, D. M., The Escape of Light Gases from Planetary Atmospheres, *J. Atmos. Sci.*, **30**, 1481-1494, 1973.

Hunten, D. M., and M. B. McElroy, Metastable $O_2(^1\Delta)$ as a major source of ions in the D region, *J. Geophys. Res.*, **72**, 2421, 1968.

Hunten, D. M., and D. F. Strobel, Production and Escape of Terrestrial Hydrogen, *J. Atmos. Sci.*, **31**, 305-317, 1974.

Jackman, C. H., A. R. Douglass, S. Chandra, R. S. Stolarski, J. E. Rosenfield, J. A. Kaye, and E. R. Nash, Impact of inter annual variability (1979-1986) of transport and temperature on ozone as computed using a two-dimensional photochemical model, *J. Geophys. Res.*, **96**, 5073-5079, 1991.

Jarchow, C, L. Song and P. Hartogh, Comparison of mesospheric ozone measurements from 50 and 70 degree northern latitude, AGU Fall Meeting 2000.

Johnson, B. R., Scott, S. K., and Tinsley, M. R.: A reduced model for complex oscillatory responses in the mesosphere, *J. Chem. Soc. Faraday Trans.*, **94**, 2707-2715, 1998.

Kaye, J. A., On the possible role of the reaction $O + HO_2 \rightarrow OH + O_2$ in OH airglow, *J. Geophys. Res.*, **93**, 285-288, 1988.

Khalil, M. A. K., R. A. Rasmussen, and F. Moraes, Atmospheric methane at Cap Meares: Analysis of a high-resolution data base and its environmental implications, *J. Geophys. Res.*, **98**, 14,753-14,770, 1993.

Klinker, E., Die numerische Simulation der nahezu zweijährigen Schwingung des mittleren zonalwindes in der äquatorialen Stratosphäre, Dissertation, Freie Universität Berlin, Berlin, 1981.

Ko, M. K. W., H. R. Schneider, R.-L. Shia, D. K. Weisenstein, and N.-D. Sze, A two-dimensional model with coupled dynamics, radiation, and photochemistry. 1. Simulation of middle atmosphere, *J. Geophys. Res.*, **98**, 20, 429-20,440, 1993.

Konovalov, I. B. and Feigin, A. M.: Towards an understanding of the nonlinear nature of atmospheric chemistry: origin of the complicated dynamic behavior of the mesospheric photochemical system, *Ann. Geophys.*, **7**, 87-104, 2000.

Konovalov, I. B., Feigin, A. M., and Mukhina, A. Y.: Toward an understanding of the nonlinear nature of atmospheric photochemistry: Multiple equilibrium states in the high-latitude lower stratospheric photochemical system, *J. Geophys. Res.*, **104**, 8669-8689, 1997.

Körner U., and G. R. Sonnemann, Global three-dimensional modelling of the water vapour concentration of the mesosphere-mesopause region and implications with respect to the noctilucent cloud region, *J. Geophys. Res.*, **106**, 9639-9651, 2001.

Körner, U., Global three-dimensional modelling of minor constituents in the middle atmosphere including the hydrogen escape flux, Thesis, Univ. Rostock, 2002.

Kouker, W., G. Brasseur, Transport of atmospheric tracers by planetary waves during a winter stratospheric warming event: a three-dimensional model simulation, *J. Geophys. Res.*, **91**, 13,167-13,185, 1986.

Kremp, Ch., U. Berger, P. Hoffmann, D. Keuer, and G. R. Sonnemann, Seasonal variation of middle latitude wind fields of the mesopause region - a comparison between observation and model calculation, *Geophys. Res. Lett.*, **26**, 1279-1282, 1999.

Krol, M. C. and Poppe, D.: Nonlinear dynamics in the atmospheric chemistry rate equations, *J. Atmos. Chem.*, **29**, 1-16, 1998.

Kulikov, M. Yu. and Feigin, A. M.: Reaction-diffusion waves in the mesospheric photochemical system, *J. Adv. Space Res.*, accepted, 2005.

Kutepov, A. A., and V. I. Fomichev, Application of the second order escape probability approximation to the solution of the NLTE vibrational-rotational band radiative transfer problem, *J. Atmos. Terr. Phys.*, **55**, 1-6, 1993.

Labitzke, K., 1981. Stratospheric-mesospheric midwinter disturbances: A summary of characteristics, *J. Geophys. Res.*, **86**, 9665-9678.

Lacis, A. A., and J. E. Hansen, A parametrization for the absorption of solar radiation in the earth's atmosphere, *J. Atmos. Sci.*, **31**, 118-132, 1974.

Lean, J. L., Estimating the solar variability of solar flux between 200 and 300 nm, *J. Geophys. Res.*, **89**, 1-9, 1984.

Lehmann, R., An algorithm for the determination of all significant pathways in chemical reaction systems, *J. Atmos. Chem.*, **47**, 45-78, 2004.

Liou, K.-N., An Introduction to Atmospheric Radiation, Academic, San Diego, Calif., 1980.

Liu, H. L. and R. G. Roble, 2002. A study of a self-generated stratospheric sudden warming and its mesospheric-lower thermospheric impacts using the coupled TIME-GCM/CCM3, *J. Geophys. Res.*, **107** (D23), 4695, doi: 10.1029/2001JD001533.

London, J., G. G. Bjarnason, and G. R. Rottman, 18 month of UV irradiance observations from the Solar Mesosphere Explorer, *Geophys. Res. Lett.*, **11**, 54-56, 1984.

Lübken, F.-J., Seasonal variation of turbulent energy dissipation rates at high latitudes as

determined by in situ measurements of neutral density fluctuations, *J. Geophys. Res.*, **102**, 13,441-13,456, 1997.

Lübken, F.-J., Nearly zero temperature trend in the polar summer mesosphere, *Geophys. Res. Lett.*, **27**, 3603-3606, 2000.

Lübken, F.-J., and J. Höffner, Experimental evidence for ice particle interaction with metal atoms at the high latitude summer mesopause region, *Geophys. Res. Lett.*, **31 (8)**, L08103, doi:10.1029/2004GL019586, 2004.

Lübken, F.-J., K. H. Fricke, and M. Langer, Noctilucent clouds and the thermal structure near the arctic mesopause in summer, *J. Geophys. Res.*, **101**, 9489-9508, 1996.

Lübken, F.-J., M. Rapp, T. Blix, and E. Thrane, Microphysical and turbulent measurements of the Schmidt number in the vicinity of polar mesosphere summer echoes, *Geophys. Res. Lett.*, **25**, 893-896, 1998.

Lübken, F.-J., M. Rapp, and P. Hoffmann, Neutral air turbulence and temperatures in the vicinity of polar mesopause summer echoes, *J. Geophys. Res.*, (submitted), 2001.

Lübken, F.-J., A. Müllemann, and M. J. Jarvis, Temperatures and horizontal winds in the Antarctic summer mesosphere, *J. Geophys. Res.*, **109**, D24112, doi:10.1029/2004JD005133, 2004a.

Lübken, F.-J., M. Zecha, J. Höffner, and J. Röttger, Temperatures, polar mesosphere summer echoes, and noctilucent clouds over Spitsbergen (78° N), *J. Geophys. Res.*, **109**, D11203, doi:10.1029/2003JD004247, 2004b.

Lübken, F.-J., U. Berger, M. Rapp, G. Baumgarten, and A. Schöch, On the physics of small scale structures in the upper atmosphere (OPOSSUM), in *Results of the German Atmospheric Research Programme - AFO 2000*, pp. 130-131, Federal Ministry of Education and Research, 2005.

Lübken, F.-J., M. Rapp, and I. Strelnikova, The sensitivity of mesospheric ice layers to atmospheric background temperatures and water vapor, *Adv. Space Res.*, submitted, 2006a.

Lübken, F.-J., W. Singer, and I. Strelnikova, Radar measurements of turbulence and absolute reflectivities during polar mesosphere winter echoes (PMWE), *Adv. Space Res.*, submitted, 2006b.

Lübken, F.-J., B. Strelnikov, M. Rapp, W. Singer, R. Latteck, A. Brattli, U.-P. Hoppe, and M. Friedrich, The thermal and dynamical state of the atmosphere during polar mesosphere winter echoes, *Atmos. Chem. Phys.*, **6**, 13-24, 2006c.

Makhlouf, U. B., R. H. Picard, and J. R. Winick, Photochemical-dynamical modeling of the measured response of airglow to gravity waves, *J. Geophys. Res.*, **100**, 11,289-11,311, 1995.

- Marsh, D., A. Smith, G. Brasseur, M. Kaufmann, and K. Grossmann, The existence of a tertiary ozone maximum in the high-latitude middle mesosphere, *Geophys. Res. Lett.*, **28**, 4531-4534, 2001.
- McCormac, B. M. (Editor), Atmospheres of Earth and the Planets, D. Reidel Publishing Company, Dordrecht, Holland, 1975.
- McDade I. C., and E. J. Llewellyn, Kinetic parameters related to sources and sinks of vibrationally excited OH in the nightglow, *J. Geophys. Res.*, **92**, 7643-7650, 1987.
- McIntyre, M.E., How well do we understand the dynamics of stratospheric warmings?, *J. Meteor. Soc. Japan*, **60**, 37-65, 1982.
- Meriwether, J. W., and M. G. Mlynczak, Is chemical heating a major cause of the mesosphere inversion layer?, *J. Geophys. Res.*, **100**, 1379-1387, 1995.
- Mlynczak, M. G., and S. Solomon, Middle atmosphere heating by exothermic chemical reactions involving odd-hydrogen species, *Geophys. Res. Lett.*, **18**, 37-40, 1991a.
- Mlynczak, M. G., and S. Solomon, On the efficiency of solar heating in the middle atmosphere, *Geophys. Res. Lett.*, **18**, 1201-1204, 1991b.
- Mlynczak, M. G., and S. Solomon, A detailed evaluation of the heating efficiency in the middle Atmosphere, *J. Geophys. Res.*, **98**, 10,517-10,541, 1993.
- Montecinos, S. E.: Reaktionskinetische-photochemische Modellierung der Ozonkonzentration der Mesosphäre, *Ph.D. thesis*, Tech. Univ. Clausthal, Germany, 1996.
- Montecinos, S. and Felmer, P.: Multiplicity and stability of solutions for a simple Chapman and more complex mesospheric photochemical model, *J. Geophys. Res.*, **104**, 11 799-11 803, 1999.
- Morton, K. W., and D. F. Mayers, Numerical Solution of Partial Differential Equations, Cambridge University Press, 1994.
- Müller, H. G.: Long-period meteor wind oscillations, *Phil. Trans. R. Soc.*, **A271**, 585-598, 1972.
- Nedoluha, G. E., R. M. Bevilacqua, R. M. Gomez, W. B. Waltman, B. C. Hicks, D. L. Thacker, and W. A. Matthews, Measurements of water vapour in the middle atmosphere and implications for mesospheric transport, *J. Geophys. Res.*, **101**, 21,183-21,193, 1996.
- Nedoluha, G. E. and P. Hartogh; Upper stratosphere comparison (WVMS and WASPAM). In: Stratospheric processes and their role in Climate (A project of the WMO/ICSU/IOC World Climate Research Program) SPARC Assessment of Upper Tropospheric and Stratospheric Water Vapor, Eds. D. Kley, J. M. Russell III, and Phillips, WCRP-113, WMO/TD No. 1043, Sparc Report No. 2, pp 139-141, December 2000.
- Nelson Jr., D. D., Schiffman, D. J. Nesbit, J. J. Orlando, and J. B. Burkholder, H+O₃ Fourier-

transform infrared emission and laser absorption studies of OH($X^2\Pi$) radical: An experimental dipole moment function and state-to-state Einstein A coefficients, *J. Chem. Phys.*, **93**, 7003-7009, 1990,

Nicolet, M., Ozone and hydrogen reactions, *Ann. Geophys.*, **26**, 531, 1970.

Offermann, D. and R. Gerndt, Upper mesospheric temperature from OH* emissions, in CIRA 1986, Part II, eds. D. Rees, J.J. Barnett, and K. Labitzke, *Adv. Space Res.*, **10**, No.12, 217-221, 1990.

Offermann, D., Satellite observations of upper stratospheric and mesospheric OH: the HOx dilemma, *Geophys. Res. Lett.*, **27**, 2613-2616, 2000.

Oldmans, S. J. and D. J. Hofmann, Increase in lower stratospheric water vapour and a midlatitude northern hemisphere site from 1981-1994, *Nature*, **374**, 146-149, 1995.

Palo, S. E. and Avery, S. K.: Observation of the quasi-two-day wave in the middle and lower atmosphere over Christmas Island, *J. Geophys. Res.*, **101**, 12 833-12 846, 1996.

Pawson, S., U. Langematz, G. Radek, U. Schlese, and S. Strauch, The Berlin Troposphere-Stratosphere-Mesosphere GCM: Sensitivity to physical parametrizations, *Q. J. R. Meteorol. Soc.*, **124**, 1343-1371, 1998.

Peter, R., K. K. nzi, and G. K. Hartmann, Latitudinal survey of water vapour in the middle atmosphere using an airborne millimeter wave sensor, *Geophys. Res. Lett.*, **15**, 1173-1176, 1988.

Poole, L. M.: The characteristics of mesospheric two-day wave as observed at Grahamstown (33.3. S, 26.5. N), *J. Atmos. Terr. Phys.*, **32**, 259-268, 1990.

Poppe, D.: Time constant analysis of tropospheric gas-phase chemistry, *Phys. Chem. Chem. Phys.*, **1**, 5417-5422, 1999.

Prather, M. J., Numerical advection by conservation of second order moments, *J. Geophys. Res.*, **91**, 6671-6681, 1986.

Radford, H. E., M. M. Litvak, C. A. Gottlieb, E. W. Gottlieb, S. K. Rosenthal, and A. Lilley, Mesospheric water vapour measured from ground-based microwave observations, *J. Geophys. Res.*, **82**, 472-478, 1977.

Rapp, M.: On the physics of polar mesospheric summer echoes, University lecturing qualification, ISSN 1615-8083, Univ. Rostock, Germany, 2004.

Rapp, M., and F.-J. Lübken, Electron temperature control of PMSE, *Geophys. Res. Lett.*, **27**, 3285-3288, 2000.

Rapp, M., and F.-J. Lübken, Polar mesosphere summer echoes (PMSE): Review of observations and current understanding, *Atmos. Chem. Phys.*, **4**, 2601–2633, 2004.

Rapp, M., B. Strelnikov, A. Müllemann, F.-J. Lübken, and D. C. Fritts (2004), Turbulence measurements and implications for gravity wave dissipation during the MacWave/MIDAS rocket program, *Geophys. Res. Lett.*, **31**, L24S07, doi:10.1029/2003GL019325, 2004.

Richmond, A. D., E. C. Ridley, and R. G. Roble, A thermospheric/ionospheric general circulation model with coupled electrodynamics, *Geophys. Res. Lett.*, **19**, 601–604, 1992.

Riese, M., D. Offermann, and G. Brasseur, Energy released by recombination of atomic oxygen and related species at mesopause heights, *J. Geophys. Res.*, **99**, 14585, 1994.

Roble, R. G., and E. C. Ridley, A thermosphere - ionosphere - mesosphere - electrodynamic general circulation model (TIME - GCM): Equinox solar minimum simulation, 30–500 km, *Geophys. Res. Lett.*, **21**, 417–420, 1994.

Rose, K., On the influence of nonlinear wave-wave interaction in a 3-d primitive equation model for sudden stratospheric warmings, *Beitr. Phys. Atmosph.*, **56**, 14–41, 1983.

Sandor, B. J. and R. T. Clancy, Mesospheric HO_x chemistry from diurnal microwave observations of HO₂, O₃, and H₂O, *J. Geophys. Res.*, **103**, 13,337–13,352, 1998.

Sander, S. P. et al., Chemical kinetics and photochemical data for use in atmospheric studies, Evaluation Number 14, *JPL Publ. 02-25*, 2003.

Scherhag, R., Die explosionsartige Stratosphärenenerwärmung des Spätwinters 1951/52, *Ber. Deut. Wetterdienstes*, **6**, 51–63, 1952.

Schoeberl, M.R., Stratospheric warmings: observations and theory, *Rev. Geophys. Space Phys.*, **16**, 521–538, 1978.

Scott, S. K., Johnson, B. R., Taylor, A. F., and Tinsley, M. R.: Complex chemical reactions - A review, *Chem. Engineer. Sci.*, **55**, 209–215, 2000.

Seele, C., and P. Hartogh, Water vapour of the polar middle atmosphere: Annual variation and summer mesosphere conditions as observed by ground-based microwave spectroscopy, *Geophys. Res. Lett.*, **26**, 1517–1520, 1999.

She, C.-Y., and R.P. Lowe, Seasonal temperature variations in the mesopause region at mid-latitude: Comparison of lidar and hydroxyl rotational temperatures using WINDII/UARS height profiles, *J. Atmos. Sol. Terr. Phys.*, **60**, 1573–1583, 1998.

Shimazaki, T., Minor constituents in the middle atmosphere, D. Reidel Publishing Company, Dordrecht, Holland, 1985.

Simon, P. C., Solar irradiance between 120 and 400 nm and its variation, *Solar Physics*, **74**, 273–291, 1981.

Siskind, D. E., B. J. Connor, R. S. Eckman, E. E. Remsberg, J. J. Tsou, and A. Parrish, An

- intercomparison of model ozone deficits in the upper stratosphere and mesosphere from two data sets, *J. Geophys. Res.*, **100**, 11,191-11,201, 1995.
- Siskind, D. E., and M. E. Summers, Implications of enhanced mesospheric water vapor observed by HALOE, *Geophys. Res. Lett.*, **25**, 2133-2136, 1998.
- Siskind, D. E., L. Coy, and P. Espy, Observations of stratospheric warmings and mesospheric cooling by the TIMED SABER instrument, *Geophys. Res. Lett.*, **32**, L09804, doi:10.1029/2005GL022399, 2005.
- Smolarkiewicz P. K., A simple positive definite advection scheme with small implicit diffusion, *Mon. Wea. Rev.*, **111**, 479-486, 1983.
- Sonnemann, G. R., The photochemical effects of dynamically induced variations in solar insolation, *J. Atmos. Sol. Terr. Phys.*, **63**, 781-797, 2001.
- Sonnemann, G. and Fichtelmann, B.: Enforced oscillations and resonances due to internal non-linear processes of photochemical system in the atmosphere, *Acta. Geod. Geophys. Mont. Hung.*, **22 (1-2)**, 301-311, 1987.
- Sonnemann, G. and Fichtelmann, B.: Subharmonics, cascades of period doublings, and chaotic behavior of photochemistry of the mesopause region, *J. Geophys. Res.*, **102**, 1193-1203, 1997.
- Sonnemann, G. R. and Feigin, A. M., Nonlinear behavior of a reaction-diffusion system of the photochemistry within the mesopause region, *Phys. Rev. E*, **59**, 1719-1726, 1999a.
- Sonnemann, G. R. and Feigin, A. M., Nonlinear response of the upper mesospheric photochemical system under action of diffusion, *Adv. Space Res.*, **24**, No. 5, 557-560, 1999b.
- Sonnemann, G. R. and U. Körner, The total hydrogen mixing ratio anomaly (THYMRA) around the mesopause region, *J. Geophys. Res.*, **108**, 4692, doi:10.1029/2002JD003015, 2003.
- Sonnemann, G. R. and Grygalashvily, M., The zonal wind effect on the photochemistry within the mesosphere/mesopause region, *Adv. Space Res.*, **32**, No. 5, 719-724, 2003.
- Sonnemann, G. R. and Grygalashvily, M.: Solar influence on mesospheric water vapor with impact on NLCs, *J. Atmos. Sol. Terr. Phys.*, **67**, 177-190, 2005.
- Sonnemann G., B. Fichtelmann, and K.-K. Ohle, An empirical ozone model of the mesosphere, *MAP Newsletter*, **3**, 5, 1984.
- Sonnemann G., A. Ebel, C. Kremp, B. Fichtelmann, and U. Berger, The global NO distribution computed on the basis of a dynamic 3d-model and implications on the winter anomaly of the D-layer, *Adv. Space Res.*, **16(1)**, 133-136, 1995.
- Sonnemann, G., Ch. Kremp, A. Ebel, and U. Berger, Calculation of the global chemical heating rates by means of a 3d-model of dynamics and chemistry, *Adv. Space Res.*, **20(6)**, 1153-1156, 1997.
- Sonnemann, G., Ch. Kremp, A. Ebel, and U. Berger, A three-dimensional dynamic model of minor constituents of the mesosphere, *Atmos. Environ.*, **32**, 3157-3172, 1998.
- Sonnemann, G., Ch. Kremp, A. Ebel, and U. Berger, The global 3D-calculation of the distribution of the plasma components within the 80 to 130 km height range, *Adv. Space Res.*, **21(6)**, 887-890, 1998.

Sonnemann, G. R., Feigin, A. M., and Mol'kov, Ya. I., On the influence of diffusion upon the nonlinear of the photochemistry of the mesopause region, *J. Geophys. Res.*, **104**, 30 591–30 603, 1999.

Sonnemann, G. R., Grygalashvyly, M., and Berger, U, Autocatalytic water vapor production as a source of large mixing ratios within the middle to upper mesosphere, *J. Geophys. Res.*, **110**, D15303, doi:10.1029/2004JD005593, 2005.

Sonnemann, G. R., Grygalashvyly, M., and Berger, Impact of a stratospheric warming event in January 2001 on the minor constituents in the MLT region calculated on the basis of a new 3D-model LIMA of the dynamics and chemistry of the middle atmosphere, *J. Atmos. Sol. Terr. Phys.*, **68**, 2012-2025, 2006.

Steinfeld, J. I., S. M. Adler-Golden, and J. W. Gallagher, Critical survey of data on the spectroscopy and kinetics of ozone in the mesosphere and thermosphere, *J. Phys. Chem. Ref. Data*, **16**, 911-918, 1987.

Strobel, D. F., Parametrization of the atmospheric heating rate from 15-120 km due to O_2 and O_3 absorption of solar radiation, *J. Geophys. Res.*, **83**, 6225-6230, 1978.

Summers, M. E., D. E. Siskind, Recombination of O and H_2 on meteoric dust as a source of mesospheric water vapor, *Geophys. Res. Lett.*, **26**, 1837-1840, 1999.

Summers, M.E., R.R. Conway, D.E. Siskind, R. Bevilacqua, D.F. Strobel, and S. Zasadil, Mesospheric HO_x photochemistry: Constraints from recent satellite measurements of OH and H_2O , *Geophys. Res. Lett.*, **23**, 2097-2100, 1996.

Summers, M.E., R.R. Conway, D.E. Siskind, M.H. Stevens, D. Offermann, M. Riese, P. Preusse, D.F. Strobel, and J.M. Russel III, Implications of satellite OH observations for middle atmospheric H_2O and ozone, *Science*, **277**, 1967-1970, 1997a.

Summers, M. E., D. E. Siskind, J. T. Bacmeister, R. R. Conway, S. E. Zasadil, and D. F. Strobel, Seasonal variation of middle atmospheric CH_4 and H_2O with a new chemical-dynamical model, *J. Geophys. Res.*, **102**, 3503-3526, 1997b.

Summers, M. E., et al., Discovery of a water vapor layer in the Arctic summer mesosphere: implications for polar mesospheric clouds, *Geophys. Res. Lett.*, **28**, 3601-3604, 2001.

Takahashi, H., and P. P. Batista, Simultaneous measurements of OH(9,4), (8,3), (7,2), (6,2) and (5,1) bands in the airglow, *J. Geophys. Res.*, **86**, 5632-5642, 1981.

Takahashi, H., M. L. Stella, B. R. Clemesha, and D. M. Simonich, Atomic hydrogen and ozone concentration derived from simultaneous lidar and rocket airglow measurements in the equatorial region, *J. Geophys. Res.*, **101**, 4033, 1996.

Tao, X., Wave-mean flow interaction and stratospheric warming in an isentropic model, *J. Atmos. Sci.*, **51**, 134-153, 1994.

Tarasick, D. W., and G. G. Shepherd, Effects of gravity waves on complex airglow chemistries. 2. OH emission, *J. Geophys. Res.*, **97**, 3195-3208, 1992.

Thayaparan, T., Hocking, W. K., MacDougall, J., Manson, A. H., and Meek, C. E.: Simultaneous observations of the 2-day wave at London (43. N, 81. W) and Saskatoon (52. N, 107. W) near 91 km altitude during the two years of 1993 and 1994, *Ann. Geophys.*, **15**, 1324–1339, 1997, SRef-ID: 1432-0576/ag/1997-15-1324.

- Thomas, G. E. and J. Olivero, Noctilucent clouds as possible indicators of global change in the mesosphere, *Adv. Space Res.*, **28(7)**, 937-946, 2001.
- Thomas, R. J., Atomic hydrogen and atomic oxygen density in the mesopause region: Global and seasonal variations deduced from Solar Mesosphere Explorer near-infrared emissions, *J. Geophys. Res.*, **95**, 16,457-16,476, 1990.
- Thomas, R. J., C. A. Barth and S. Solomon, Seasonal variation of ozone in the upper mesosphere and gravity waves, *Geophys. Res. Lett.*, **11**, 673-676, 1984.
- Thompson, J. M. T. and Stewart, H. B.: Nonlinear dynamics and chaos, John Wiley, New York, 1991.
- Turnbull, D. N. and R. P. Lowe, New hydroxyl transition probabilities and their importance in airglow studies, *Planet. Sci.*, **37**, 723-738, 1989.
- U. S. Standard Atmosphere 1976*, U. S. Government Printing Office, Washington, D. C. 20402, Stock No. 003-017-00323-0
- van Leer, B., Toward the ultimate conservative difference scheme, IV: A new approach to numerical convection, *J. Comp. Phys.*, **23**, 276-299, 1977.
- Vidal-Madjar, A., Evolution of the solar Lyman-alpha flux during four consecutive years, *Solar Physics*, **40**, 69-86, 1975.
- Vidal-Madjar, A., The solar spectrum at Lyman-alpha 1216 Å, in: *The Solar Output and its Variation*, edited by O. R. White, *Colo. Assoc. Univ. Press*, Boulder, 213-236, 1977.
- Vidal-Madjar, A. and Phissamay, The solar L flux near solar minimum, *Solar Physics*, **66**, 227-271, 1980.
- von Zahn, U., and J. Bremer, Simultaneous and common-volume observations of noctilucent clouds and polar mesosphere summer echoes, *Geophys. Res. Lett.*, **26**, 1521-1524, 1999.
- von Zahn, U., Fricke, K. H., Gerndt, R., and Blix, T., Mesospheric temperatures and the OH layer height as derived from ground-based lidar and OH* spectrometry, *J. Atmos. Sol. Terr. Phys.*, **49**, 863-869, 1987.
- Walcek, C. J., Minor flux adjustment near mixing ratio extremes for simplified yet highly accurate monotonic calculation of tracer advection, *J. Geophys. Res.*, **105**, 9335-9348, 2000.
- Walcek, C. J. and N. M. Aleksic, A simple but accurate mass conservative, peak preserving, mixing ratio bounded advection algorithm with Fortran code, *Atmos. Environm.*, **32**, 3863-3880, 1998.
- Ward, W. E., Wang, D. Y., Solheim, B. H., and Shepherd, G. G.: Observations of the two-day wave in WINDII data during January, 1993, *Geophys. Res. Lett.*, **23**, 2923-2926, 1996.
- Ward, W. E., Solheim, B. H., and Shepherd, G. G.: Two day wave induced variation in the oxygen green line volume emission rate: WINDII observations, *Geophys. Res. Lett.*, **24**, 1127-1130, 1997.
- Ward, W. E., Oberheide, J., Riese, M., Preusse, P., and Ofermann, D.: Planetary Wave Two Signature in CRISTA 2 Ozone and Temperature Data, in: *Atmospheric Science Across the Stratopause*, *Geophysical Monograph*, **123**, 319-325, 2000.

Woods, T. N., W. K. Tobiska, G. J. Rottman, and J. R. Worden, Improved solar Lyman irradiance modeling from 1947 through 1999 based on UARS observations, *J. Geophys. Res.*, **105**, 27,195-27,215, 2000.

World Meteorological Organization (WMO), *Scientific Assessment of Ozone Depletion: 1998*, Geneva, 1999.

Wu, D. L., Hays, P. B., Skinner, W. R., Marshal, A. R., Burrage, M. D., Liebermann, R. S., and Ortland, D. A.: Observations of the quasi 2-day wave from the high resolution Doppler imager on UARS, *Geophys. Res. Lett.*, **20**, 2853–2856, 1993.

Wu, D. L., Fishbein, E. F., Read, W. G., and Waters, J. W.: Excitation and evolution of the quasi -2-day wave observed in UARS/MLS temperature measurements, *J. Atmos. Sci.*, **53**, 728– 738, 1996.

Yang, H., E. Olaguer, and K. K. Tung, Simulation of the present day atmospheric ozone, odd nitrogen, chlorine and other species using a coupled 2-d model in isentropic coordinates, *J. Atmos. Sci.*, **98**, 442-447, 1991.

Yang, P. and G. Brasseur, Dynamics of the oxygen-hydrogen system in the mesosphere, 1. Photochemical equilibria and catastrophe, *J. Geophys. Res.*, **99**, 20.955-20.965, 1994.